Modeling and Control of Transport Processes during Melt Crystal Growth

A DISSERTATION
SUBMITTED TO THE FACULTY OF THE GRADUATE SCHOOL
OF THE UNIVERSITY OF MINNESOTA
BY

Nan Zhang

IN PARTIAL FULFILLMENT OF THE REQUIREMENTS
FOR THE DEGREE OF
DOCTOR OF PHILOSOPHY

Jeffrey J. Derby, Adviser

September 2012

Acknowledgments

To all the people that I have met or have met me in person, on phone, by email, and via unrecognized but existed connections, many thanks. Without you, I wouldn't be me today.

to my Mom *Baoxia Xing*

Abstract

In this thesis, detailed, realistic, multi-scale numerical models are developed and employed to study various systems applied for the growth of crystals from melt, including the melt growth of single-crystal *Cadmium Zinc Telluride(CZT)* and *Sapphire*.

The melt growth of single-crystal Cadmium Zinc Telluride(CZT), a very promising high-value crystal widely used in radiation detectors and other applications, has been challenging to the crystal growers in terms of yield and quality. In order to address such challenges, a transient, coupled model has been developed to analyze the segregation of zinc in CZT grown in an electrodynamic gradient freeze (EDG) furnace used at Pacific Northwest National Laboratories and Washington State University. The coupled model consists of a local model that solves for time-dependent melt flow, heat transfer, melt-crystal interface position, and zinc distribution in both melt and solid phases and a quasi-steady-state global model that features realistic furnace heat transfer. Surprisingly, anomalous zinc segregation is predicted, featuring a non-monotonic axial concentration profile and several local minima and maxima across the boule. A mechanistic explanation is put forth based on the cumulative effect of changes in multi-cellular melt flow structures, a particularly susceptible occurrence for CZT systems.

Furthermore, optimized EDG furnace profiles are developed that promote the growth of CZT crystals with a uniformly convex interface shape. Such interface shapes are expected to improve the single-crystalline yield of this material. These computations clearly show how interface shape modification can be put directly into practice simply by changing thermal set points in existing EDG growth systems. In addition, the quenching process for CZT crystals has also been investigated by global model.

Finally, a similar model has also been applied to investigate the single-crystal growth of sapphire, a very important substrate material for the fabrication of gallium-nitride light-

emitting-diodes (LEDs), by Heat Exchanger Method (HEM). Both quasi-steady-state and transient analysis have been performed to investigate the effects of furnace geometry and processing parameters on the temperature distribution, convection, and melt-crystal interface shape. Results have provided key insight into the further optimized design of HEM furnace.

Contents

List of Tables

List of Figures

Chapter 1

Introduction

1.1 Introduction

Crystals are the central components of the modern technological and pharmaceutical products, such as the CPU chips, silicon wafers, solar cells and so on. However, the physics of many crystal growth processes still remain elusive. This lack of understanding is mostly due to the enormous nonlinear complexity of crystal growth processes, which often require the control of multiple parameters that interact through nonlinear relationships [1], as shown in Figure 1.1. The historical approach to optimizing crystal growth processes has often required systematic trial-and-error experiments, based on certain simple theory and many direct observations and, more importantly, experience. To fully understand the interrelation of essential growth parameters would require thousands of growth runs, and hence crystal growth in many cases has remained an art.

However, the successful development and application of numerical models to study crystal growth processes have shed new light on the field, enabling crystal growth less of an art and more of a science. Detailed simulations guided by experimentally derived properties are now capable of providing researchers with a qualitative, even quantitative, understanding of the role that essential parameters play on crystal growth. Furthermore, advancements in computing power and algorithms have allowed us to replace systematic trial and error studies of crystal growth processes with much quicker and frugal experimental studies. But as models become more and more realistic to account for the further details in growth, the physical complexity of crystal growth translates to increased computational complexity.

The physical and chemical processes that determine crystal growth occur over disparate

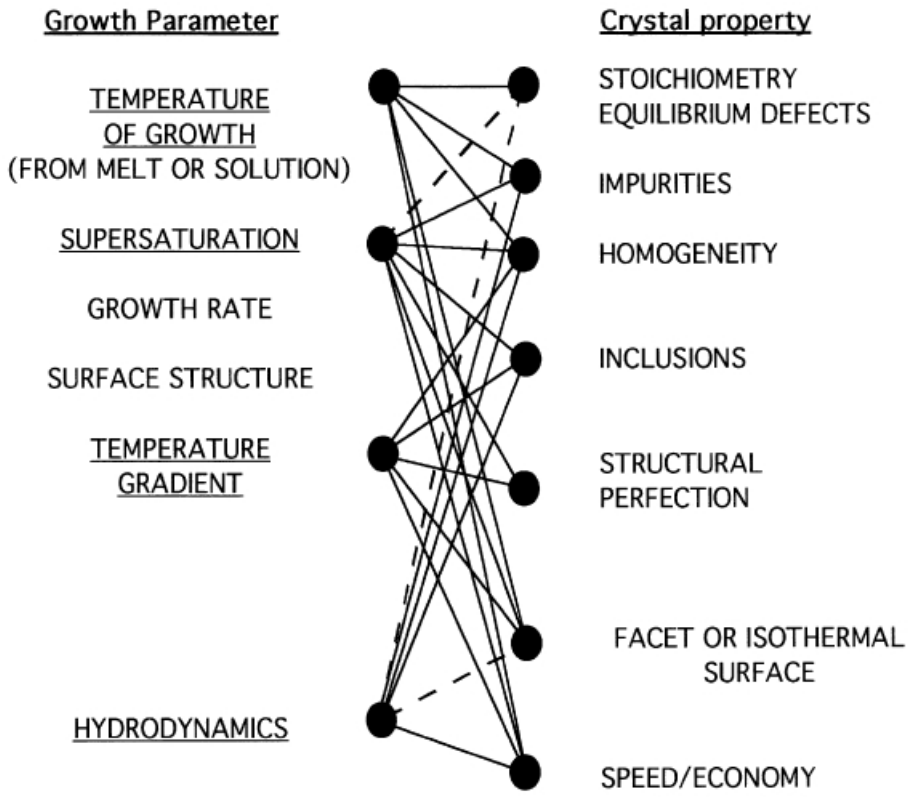

Figure 1.1: Impact of the four major growth parameters on the properties of crystal and on the economy of crystal fabrication, from [1]

length scales, ranging from the size of atoms and molecules incorporating at the growth interface to the size of the vessels and furnaces applied for growth. The encompassing accounting of these disparate length scales in a single computational model remains challenging. However, many crystal defects on the nano-to-micro end of this length scale have been correlated to continuum transport properties on the meso-to-macro end, allowing much to be learned about crystal growth processes through continuum transport models. Models coupling solutal convection and species transport have led to breakthroughs in the growth of crystals for non-linear optical materials [8, 9, 10, 11]. In recent years, detailed models have been developed that couple the continuum transport of momentum, species and energy, and account for the shape of the growth interface [12, 13, 14, 15, 16, 17]. Attention to model detail along with faithful model validation procedures have made crystal growth modeling an essential part of crystal growth research.

In this thesis, computational models that contribute to our understandings of transport processes within several different growth systems have been presented. We investigate and analyze transport phenomena in melt crystal growth processes. The models developed and employed here rigorously account for realistic details, allowing us to apply physically accurate boundary conditions. Both advanced finite element and finite volume methods have been applied to solve the continuum transport equations.

1.2 Melt crystal growth methods

The majority of semiconductor single crystals are grown by directional solidification from the melt phase by many melt crystal growth methods. The premise of such methods is that the material is solidified from its liquid phase, where the solid phase consists, preferably, of a single crystal. These methods are broadly classified as meniscus-defined techniques and confined growth techniques [18, 19, 20]. The classification of the method is based on what determines the shape of the growing crystal. In meniscus-defined techniques, the meniscus between the melt and a gaseous environment shapes the crystal near the solidification interface. In confined growth techniques, the crystal takes the shape of the surrounding container known as an ampoule or crucible.

The most widely used meniscus-defined growth technique is the Czochralski method (CZ) shown in Figure 1.2. A seed crystal is dipped into a pool of the molten material, and the crystal grows as the seed is slowly pulled out of the pool. Cylindrical boules of single crystalline semiconductors such as silicon, germanium, gallium arsenide, and indium

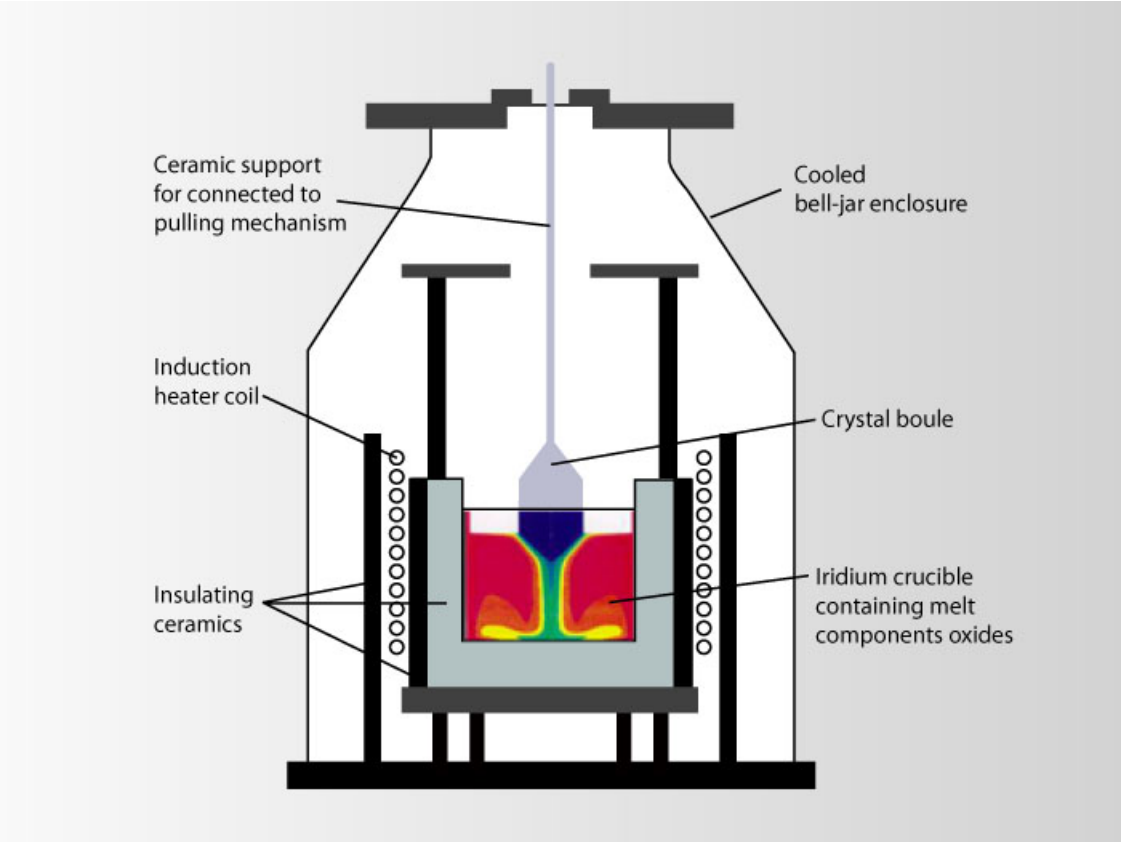

Figure 1.2: Schematic diagram of a Czochralski melt growth furnace. (Adapted from Scientific Material Corp.)

phosphide are grown via variations of the CZ method [20, 21, 22] .

While large radius crystals can be grown using the CZ method, this method is unsuitable for the growth of certain materials. Some materials have high vapor pressures where stoichiometry control in the melt is difficult in a CZ system. With confinement, the melt can be subjected to a high over-pressure to prevent out gassing. Confined growth is also used for materials where low axial temperature gradients are required to produce low dislocation densities in the crystal [19]. The thermal environment that the growing crystal is subjected to, both melt and solid phases, can be carefully controlled in a confined system.

The Bridgman-Stockbarger method is the most commonly used confined growth technique where growth occurs in a container known as an ampoule or crucible. Bridgman furnaces are either aligned with gravity, vertical Bridgman (VB) systems, or perpendicular

to gravity, horizontal Bridgman (HB) systems. Figure 1.3 shows a schematic of a vertical Bridgman furnace where growth occurs upwards from the bottom, or vertical direction. The use of the end product influences the choice between VB and HB growth methods. VB furnaces are cylindrical making it more practical to produce circular wafers for most semiconductor uses. HB furnaces are more likely to be used when wafers of material are needed. Single crystalline gallium arsenide, indium phosphide, and cadmium zinc telluride are grown via variants of the Bridgman-Stockbarger system [23, 20, 24, 25].

A VB system is made up of a cylindrical furnace that surrounds a cylindrical ampoule. Raw materials are loaded into the ampoule, completely melted and homogenized through convective mixing. The ampoule is often sealed at the top with a gaseous overhead on top of the melt. The furnace temperatures are then adjusted to vary along the furnace length with temperatures hotter at the top and cooler at the bottom, temperatures relative to the crystal's melting point. Traditionally, solidification was induced by translating the ampoule through furnace from the hot end toward the cool end. A variation on the Bridgman-Stockbarger method is the gradient freeze method where heater powers of multi-zone heaters are varied with respect to time while the ampoule is held stationary. The crystal is removed from the ampoule after solidification. Crystallization is initialized by either placing a seed crystal at the cool end of melt or by heterogeneous nucleation by undercooling a portion of the melt. In general, HB furnaces work by the same theory as VB furnaces, but in the horizontal direction. This thesis focuses on crystal growth performed using the VB method and its gradient freeze analog as it is the method used to grow the types of CZT crystals we are interested in.

Another commonly used confined growth method is the Heat-Exchanger Method (HEM), which is very promising and competing method for the growth of sapphire (a widely applied substrate material for the fabrication of GaN-based LEDs). In the HEM furnace as shown in Figure 1.4, the charge within the crucible is melted by the heating element, and then the heat is extracted from the base of the crucible by the heat exchanger (also called "cold finger") to initiate the solidification process. Therefore, the thermal field within the crucible including both the melt and crystal phase is highly dependent on and sensitive to the conditions of heating elements around the crucible and cooling system below the base of crucible, which affect the thermal gradient in the melt and crystal respectively. However, the prediction, or even understanding of the thermal field and melt convection in such system is extremely hard to obtain just by experiments, especially when it comes to the growth of high-melting-point, semitransparent crystals such as sapphire where the radiative heat transfer is largely

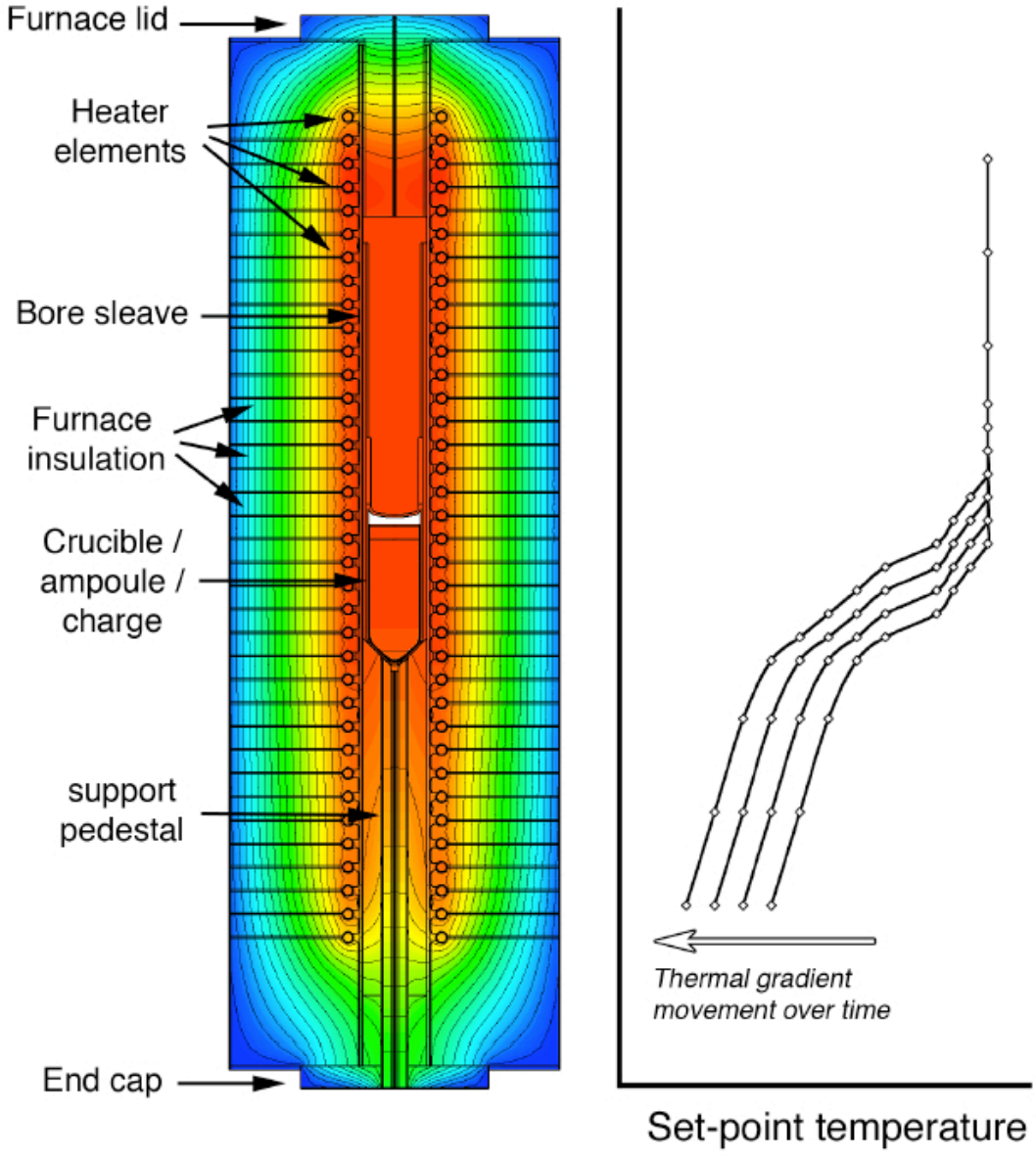

Figure 1.3: Schematic diagram of a vertical Bridgman melt growth furnace. Furnace imposed temperature profile is shown. The melting point temperature of the crystal lies between the temperature T_{hot} and T_{cold}. Solidification occurs from the bottom to the top of the ampoule. The axis of the VB system is aligned with the gravity vector.

involved [26, 27, 28, 29].

1.3 Physics of vertical Bridgman growth

All melt crystal growth systems are subject to the same physical governing forces, but we will analyze them in the context of a VB system. A VB furnace is a multi-domain system in which a wide range of physical phenomena occur over a large extent of length and time scales (atoms to cubic centimeters) [3]. These physical phenomena include coupled bulk transport of heat, mass, and momentum transfer along with thermodynamic phenomena such as phase change and equilibrium partitioning of solutes along the solidification front [30].

Heat transport plays an especially important role in that melt crystal growth furnaces are essentially heat transfer unit operations where a high temperature melt is solidified into a crystal at a lower temperature. Heat conduction, heat convection, and radiation all play a role in VB systems. In the furnace domain heat transfer is governed by heat conduction and radiation. Both heat conduction and convection are important in the melt phase. In addition, momentum convection in the melt is driven by temperature gradients, buoyancy driven flow, which in turn affects the solute concentration in both the melt and solid phases. The solid phase is governed by heat conduction. Depending on the material, radiation effects may be present in the growing crystal. The macroscopic shape between the melt and crystal is influenced by the interaction of the material with the thermal environment. A thorough understanding of heat transfer and its interactions with mass transport, momentum transport, and phase change is needed for effective design of VB systems for the material of interest.

1.3.1 Heat transfer effects

Melt temperatures should be high enough to maintain the material in a molten state, but lower than temperatures where the melt either decomposes or vaporizes. Also, the axial temperature gradient that drives solidification should be large enough to prevent the occurrence of constitutional supercooling where the equilibrium melting temperature changes with variations in concentration at the melt-crystal interface. A wavy interface can develop that can become successively more unstable as the underlying driving forces increase. Cells, and even dendrites, can form [31]. The phenomenon is common in melt growth of multiple component materials [32]. On the other hand, large axial temperature

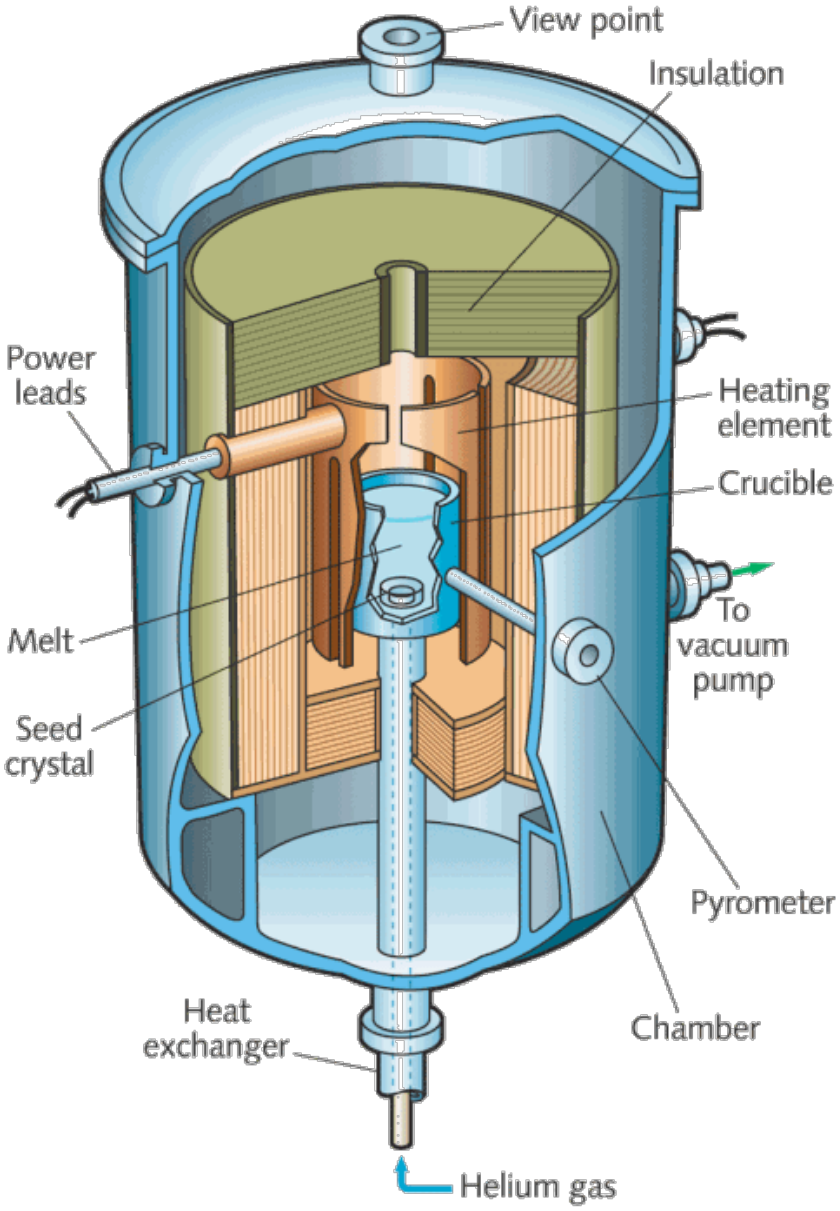

Figure 1.4: Schematic diagram of a Heat-Exchanger melt growth furnace. Solidification occurs from the bottom to the top of the ampoule. The axis of the HEM system is aligned with the gravity vector.(Adapted from LaserFocusWorld.)

gradients can result in undesirably high thermal stresses in the crystal which can cause in high dislocation density in the crystal [33]. Intense time-dependent buoyant flows driven by high thermal gradients can cause fluctuations in the temperature and dopant concentration which in turn can cause the melt-crystal interface to melt and resolidify. This leads to striations, or local compositional non-uniformities, in the crystal [34, 35].

The interplay between the heat transfer environment and physical properties affects the shape of the melt-crystal interface known as the *interface effect* [36]. The physical properties include heat conductivities of the melt, solid, and ampoule and the rate latent heat is released at the interface during solidification.

Three general macroscopic interface shapes can occur: flat, concave, and convex. Crystals grown with no radial temperature gradient and constant axial temperature gradient have flat interfaces, and no thermal stresses are produced [37]. Curved interfaces are more likely to have adverse interactions at the melt-crystal-ampoule tri-point that can result in twinning and higher dislocation density [33]. With an interface that is concave with respect to the melt, these interactions tend to propagate toward the bulk crystal [18, 37]. Conversely, an interface that is convex with respect to the melt favors grain selection [38] and minimizes the potential for defects by propagating spurious crystal nucleated at the tri-junction toward the ampoule wall. Thus these new grains grow away from the bulk crystal, and self eliminate themselves against the ampoule wall. Much work has been conducted to understand what causes interface shape and how to achieve a desired shape by changing ampoule material, ampoule translation rate, furnace gradient, or adding a submerged heater [39, 40, 38, 41, 42, 43, 44, 36, 15, 45, 46, 47, 48, 49].

Under typical growth conditions in a VB system, CZT has a concave interface shape due to the smaller heat conductivity in the solid than the melt, and the relatively large amount of latent heat generated at the interface. The typical method of minimizing a concave curvature is to increase the applied temperature gradient. However, CZT is also brittle and prone to cracking caused by thermal stresses which puts an upper limit on the furnace temperature gradient.

1.3.2 Momentum transfer effects

Fluid flow in a melt growth system is mainly driven by buoyancy effects caused by temperature variations in the bulk of the melt. If the melt has a free-boundary with a gaseous phase, the surface tension gradient caused by temperature variations along this boundary

can cause Marangoni flow in the melt [50]. The melt can exhibit a wide range of flow behavior from time-independent laminar flow to intense turbulent flow depending on the driving force, system geometry, and boundary conditions [51, 52, 53]. In general the flow is two-dimensional due to the inherent axisymmetry of the VB system. Three-dimensional flows are encountered in these systems due to symmetry breaking flow instabilities [54] or system imperfections such as tilting or asymmetric heating [55, 56, 57, 58].

As previously mentioned, the interaction between fluid flow and species transport plays an important role in setting the composition profile of the crystal. A magnetic field can be imposed to damp intense time-dependent flow if the melt is a conducting material [59, 60]. With a large enough magnetic field, the flows may be suppressed to the point where diffusion-limited growth is reached. Growing crystals in a microgravity environment can also promote diffusion-limited growth since buoyant flows are suppressed considerably [61]. Accelerated crucible rotation is used to promote mixing in the melt and thereby reduce the possibility of constitutional supercooling [62, 63, 64]. Steady crucible rotation can be used to suppress flow in the melt to reduce axial segregation [55, 56, 65].

1.3.3 Mass transfer effects and segregation

The spatial distribution of composition is important to crystal quality especially in multi-component semiconductor alloys such gallium-doped germanium and cadmium zinc telluride. In the case of CZT, zinc can be considered a dopant that is present in high concentrations. Mass transfer is driven by both mass convection and diffusion in the melt phase and diffusion in the solid crystal phase. During growth, equilibrium partitioning along the melt-crystal interface results in a depletion or accumulation in the melt of the dopant species depending on which phase the dopant is preferentially incorporated [32]. This partitioning effect coupled with diffusion and convection in the melt results in compositional non-uniformities, also known as segregation.

However, to achieve a homogeneous dopant distribution is extremely difficult in practice which requires both growth rate and convection to be constant during growth. Because minor fluctuations of growth rate, due to local temperature fluctuations from turbulent buoyancy driven flows when near the melt/solid interface for example, could create the undesired solute banding. Furthermore, the thermodynamics of phase changes and mass transfer could also hinder homogeneity [32]. For a nearly pure material (dopant added to a pure material) the phase behavior can be described by a phase diagram of melting

temperature as a function of concentration. Fig. 1.5(a) describes a simplified phase diagram of a dilute binary alloy. The equilibrium segregation coefficient is defined as the ratio of the solid concentration to the liquid concentration at equilibrium. At a given melt temperature, the solid and liquid concentration have different values. This is known as segregation. In this simplified case, where the solidus and liquidus curves are straight lines intersecting at the pure solve composition, k is constant.

The case of diffusion limited growth in one dimension, as shown in Fig. 1.5(b), has been investigated by Tiller et al. [66]. No convection exists within the melt and the segregation coefficient, k, is assumed to be less than one. Both the solid and liquid phase have the same composition, c_o at the initial stage. Solute rejected into the liquid (since $k < 1$) at the interface is taken away only by diffusion which create a solute boundary layer. The liquid concentration at the interface increases with time until it is exactly c_o/k. The solid concentration is constant at c_o for the entire length of the crystal except for initial and final transient stages [32].

The other extreme case that could exist is perfect mixing resulting from the convection within the melt. Here one can assume that the crystal growth rate is slow enough for convection mixing to eliminate all concentration gradients in the melt, while is still quick enough to neglect the solid diffusion [67]. If so, the solid concentration is not constant any more, but a function of the solid fraction. Hence the axial segregation appears. This relationship is described by the Scheil equation [32].

Great majority of practical melt crystal growth cases lie between the diffusion limited and the perfectly mixed extremes. The flow going through transitions will have a considerable effect on the concentration profile within the melt as the intense of convection increases,. The BPS model proposed by Burton, Prim, and Schlicter [68] firstly decoupled the effects of diffusion and convection. In a stagnant film of thickness δ in front of the interface within the melt phase, diffusion could be assumed to be the only transport means. whereas convection is the only transport mechanism occurring beyond the film. For convenience, an effective segregation coefficient is defined as the ratio of the equilibrium solid concentration versus the bulk concentration of the melt, $k_{eff} = c_s/c_o$. As described in Fig. 1.5(c), the effective segregation coefficient approaches unity and diffusion limited growth is obtained as $\delta \to \infty$. While as $\delta \to 0$ and $k_{eff} \to k$, occurring is the perfect mixing of the melt which is described by the Scheil equation. Although the BPS model is plausible since its conceptual simplicity and satisfactory represent of experimental segregation data , it can not be employed to predict the segregation [2]. Segregation across the interface, which

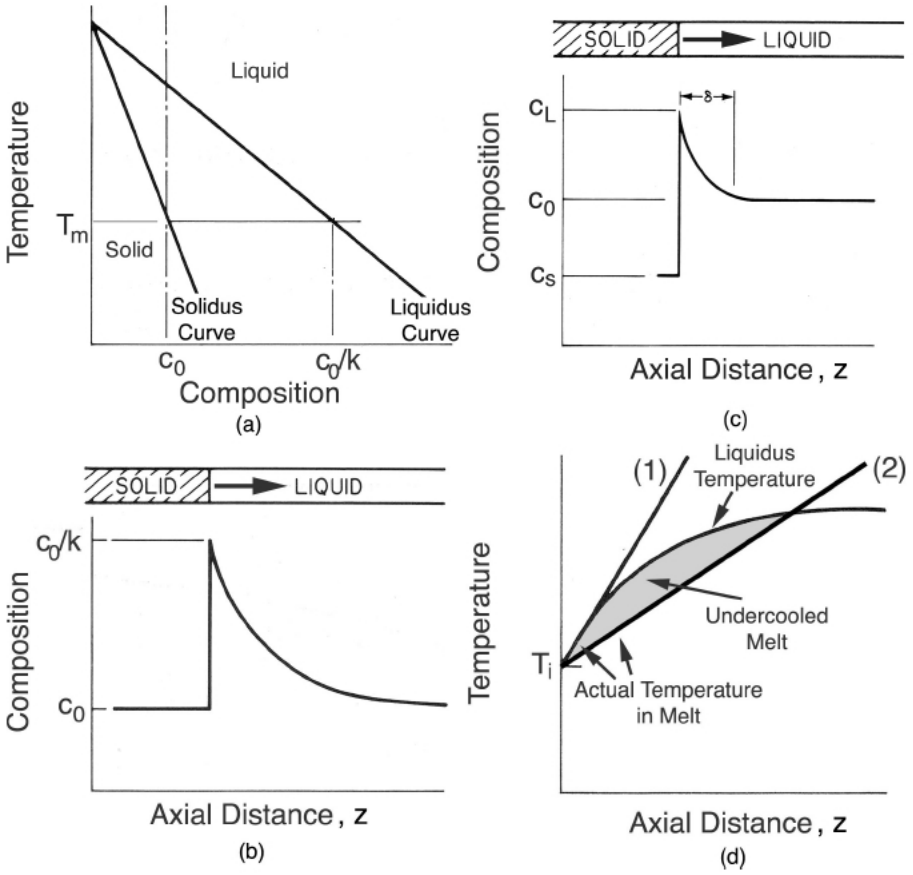

Figure 1.5: Solidification of a dilute binary alloy: (a) simplified phase diagram, (b) diffusion-limited axial segregation, (c) BPS model of axial segregation, and (c) constitutional cooling conditions. Reproduced from [2]

can be extremely significant for the solute distribution, is ignored in this one-dimensional model. Even for moderate convection there can be up to 60% segregation as shown by Chang and Brown [69]. Such gross simplification could be avoided by applying numerical methods.

Another difficulty that hinders the single crystal growth is the constitutional supercooling [70, 67], a phenomenon that could occur in compound melt growth. The term constitutional indicates that supercooling is resulting from the local changes of composition not temperature. As shown in Fig. 1.5(c), the composition in the melt is a function of position when both diffusion and convection exist within the melt. As shown in Fig. 1.5(a), the equilibrium melting temperature is a function of composition. Temperature profile (1) shows a stable crystallization front where every point in front of the interface is above the liquidus temperature. If a protuberance occurs at the interface, it will sense itself in a superheated environment and will melt back again [32]. In contrast, thermal profile (2) describes a case where the thermal gradient is too small and much of the melt front is below the equilibrium melt temperature. A protuberance at the interface will sense itself in a supercooled environment and will rapidly grow. Therefore, thermal profile (1) is considered to be morphologically stable while thermal profile (2) is unstable [71]. A wavy interface, cells and even dendrites could occur. This interface is referred to as the Mullins-Sekerka instability [72]. In order to eliminate supercooling in the melt, the latent heat released during solidification at the melt/crystal interface must be removed by conduction through the solid instead of into the liquid [73]. A balance must be kept between minimizing the effects of constitutional supercooling and thermal stress when growing materials that are sensitive to thermal stress.

The shape of melt/crystal interface is another significant factor affecting the product quality. It is determined by the melt temperature isotherm in the growing crystal. And the melt temperature isotherm is determined by the internal heat flux. There are a variety of factors affecting the thermal environment such as the furnace temperature profile, the thermal conductivities of the melt, crystal, and surroundings, the latent heat generated by solidification and the radiation heat transfer in the system. A concave interface typically has undesired interface/ampoule interactions causing twinning and higher dislocation density [67]. A convex interface toward the melt will benefit grain selection [74] and minimize the potential for defects or spurious crystals nucleated at the ampoule wall to propagate toward the bulk crystal [67, 75]. Crystal growth with no radial temperature gradient and having a constant axial temperature gradient will result in a flat interface, and hence no thermal

stresses exist [76].

Striations is another phenomena in melt growth, arising from time-dependent convective melt flow. Fluctuations in temperature and concentration can cause the melt/crystal interface to melt and re-solidify which leads to the striations [77, 78]. The striations, considered as local axial solute segregation, cause the inconsistent crystal composition contributing to variable material and electrical properties which is detrimental to product quality. Kim, Witt, and Gatos studied the effects of flow intensity on flow stability and solute segregation in tellerium-doped indium antimonide and gallium-doped germanium [79, 80].

Many challenges associated with growing high quality, single crystal products such as segregation, sensitivity to thermal stress, striations, and surface instability need to be fully understood and precisely controlled, which is the essential basis for the designed furnace for crystal growth including the furnace temperature profile required to be fully controlled and monitored to minimize not only thermal stress but constitutional supercooling. And the overhead pressure or a gaseous are often needed when a volatile component is present. Ampoule pull rate and the material of the ampoule could also influence the quality of crystals. Due to the difficulties such as the expensive cost and long growing time associated with crystal growth, numerical simulations have become an indispensable tool in the respect of guiding and optimizing crystal growth processes. Furthermore, system behaviors that can not be monitored in real-time is attainable by employing numerical simulations which, in turn, could help promote the final product quality.

1.4 Modeling vertical Bridgman systems

The goal of crystal growth processes is to produce large, defect-free, compositionally uniform, single crystals. CZT crystals with all of these characteristics are never grown, and yields of useable material are very low. The crystals are often contaminated with crystallographic defects such as grain boundaries, twins, inclusions, precipitates, and micro-cracks [81]. Compositional in-homogeneities from axial and radial segregation also reduce crystal quality [82]. A considerable amount of research has been done to develop crystal growth processes to reduce crystallographic defects and improve composition uniformity [19]. Mathematical modeling in conjunction with empirical knowledge gained from experiments has been successfully used to enhance our understanding of the connection between processing conditions during crystal growth and crystal quality [83]

A wide range of physical phenomena occur during crystal growth, and over a vast extent

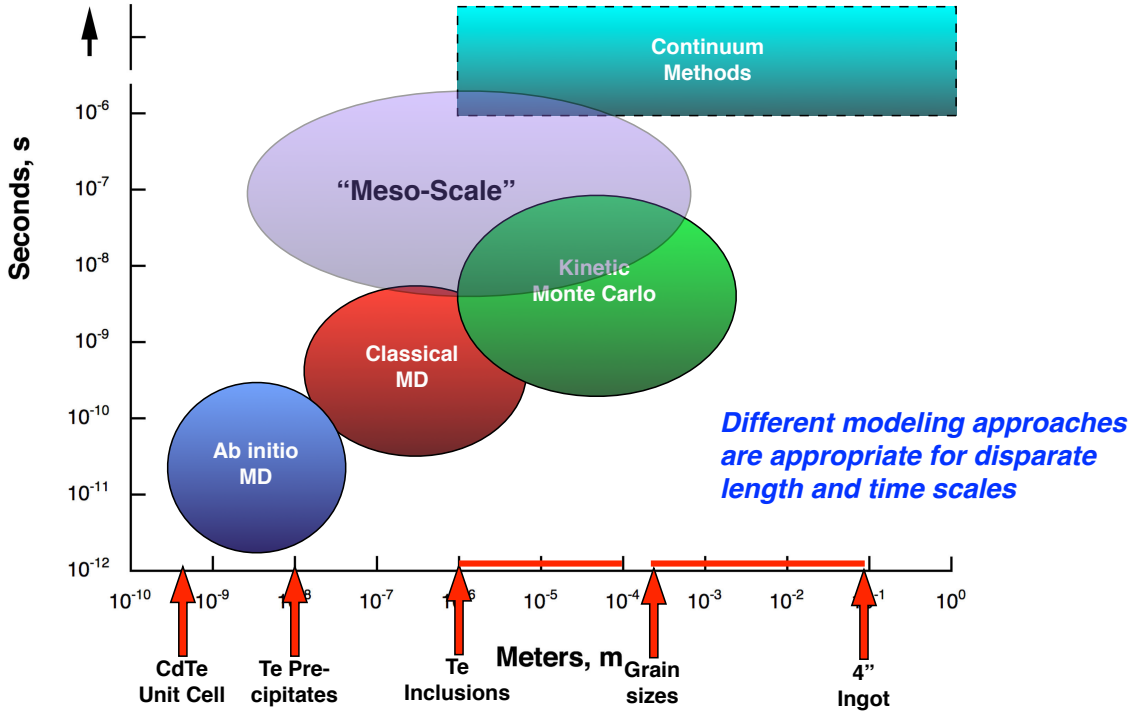

Figure 1.6: Modeling approaches for various length and time scales, reproduced from Derby [3].

of length and times scales [3]. It is not possible to simulate all of the physics within one model, so compromises must be made. Figure 1.6 illustrates different modeling approaches used for various length and time scales. Atomic behavior on the tens of nanometers scale is studied using *ab initio* molecular dynamics methods. Simulations at this scale are limited to systems of a few hundred atoms on time scales of tens of picoseconds. Larger ensembles and longer time scales are studied by employing molecular dynamics models based on classical potentials. The kinetic Monte Carlo method is utilized on systems of even larger length scales and longer time scales. At the bulk crystal growth level, continuous governing equations best describe the process where processing conditions can be connected to the final crystal structure. Work has also been done to link the kinetic growth on the crystal surface to bulk transport at this meso-scale length [84, 30, 85, 86]. Phase field methods have been used to model meso-scale phenomena such as dendritic growth [87]. The work presented in this thesis is based on continuum level physics.

Modeling of crystal growth processes began with simple one-dimensional models that had analytical or semi-analytical solutions [32]. Tiller et al. [88, 89] studied equilibrium partitioning in an unidirectional solidification model assuming diffusion in both the melt and crystal, but ignoring convection in the melt which predicted an almost uniformly doped crystal. However, axial segregation is known to occur in the presence of melt convection. In the limit of complete mixing of the melt, the axial composition profile of the solute is given by the Scheil equation [90]. In reality convection is not always intense enough to justify the assumption of complete mixing in the melt. Therefore, to describe axial segregation caused by the interaction of diffusion and intermediate levels of convection, Burton, Prim, and Schlicter [91] formulated a model that invoked the concept of a stagnant-film as first proposed by Nernst [92]. The BPS model, as it's popularly known, proposed the existence of a stagnant-film of thickness δ ahead of the solidification interface in the melt, or a diffusion layer. This model assumed diffusion only within the stagnant-film and complete mixing outside this layer.

Though the BPS model is successful in fitting experimental axial segregation data in most cases, it has several drawbacks. In a system there is never a demarcation between well-mixed and quiescent parts of the melt. Convection and diffusion are important through out the melt. Furthermore, use of a single physical parameter δ grossly over-simplifies the interactions between furnace design, heat transfer, buoyancy driven flow on solute partitioning in crystal growth systems. Coriell and Sekerka [93, 94] showed that considerable radial segregation occurred in unidirectional solidification of binary alloys due to a curved melt-crystal interface, but BPS, being a one-dimensional model, cannot predict radial segregation. Wilcox [95] and Rosenberger and Müller [96] discussed the drawbacks of the BPS model. Brown and Kim [97] also highlighted the limitations of the BPS model, and showed that results from detailed numerical simulations of a two-dimensional model of Bridgman growth better matched solute segregation data from growth experiments on a gallium-doped germanium system.

By the 1980's, computing power had risen to a level where such detailed numerical simulations of two-dimensional models were possible. By exploiting the cylindrical geometry of the VB system, an assumption of azimuthal symmetry (or axisymmetry) reduced three-dimensional systems to two dimensions. These early efforts typically did not include momentum transport but only heat conduction and included only the melt, crystal and ampoule [39, 38, 98, 41, 44, 36, 45]. However, thermodynamic phenomena such as phase change, release of latent of heat of fusion, and equilibrium partitioning of solutes were also included

as well as prediciting the macroscopic shape of the melt-crystal interface. As the field matured, more sophisticated models were developed that coupled bulk transport phenomena of heat, mass, and momentum transfer [97, 99, 100, 101, 102, 12, 13, 103, 104, 57, 65]. Much of this work is summarized in a still-relevant review article by Brown [19], and more recent reviews by Müller [105], Lan [106], and Yeckel and Derby [83].

Temperature fields predicted by the above two-dimensional models have also been used to solve for von Mises stresses in the crystal by assuming a continuum thermoelasticity model [107, 108, 100] for the crystal. Defects are known to be generated when the stresses in the system are greater than the critically resolved shear stress (CRSS) of the crystal [19]. Based on the thermoelastic stress analysis, qualitative predictions can be made on the density of defects in the crystal. Models capable of making quantitative predictions of defect density have also been developed [109].

Though the VB system has an azimuthal symmetry, three-dimensional effects are known to occur in these systems due to symmetry-breaking system imperfections caused by an ampoule tilt, ampoule misalignment with the furnace, and defective heating elements. Three-dimensional flows can also develop when the driving forces of buoyant convection pass some critical point [19]. Three-dimensional, quasi-steady-state, models [55, 56, 57, 58] have been used to predict three-dimensional flow patterns and solute segregation. Recent developments in parallel computing algorithms and hardware have helped in the implementation of these three-dimensional models.

These models, however, neglect modeling the furnace environment, and the effect of the surrounding furnace is included as an idealized heat transfer boundary condition along the ampoule walls. Other researchers, such as Müller and coworkers and Dupret et al. [110, 111], took a separate route and concentrated on developing highly detailed, two-dimensional models of the crystal growth furnaces that included radiative transport over complicated geometries. These efforts, however, have only limited capability of modeling the complex fluid dynamics that can occur in the melt phase. Instead, these models have been used to supply realistic heat transfer boundary conditions along the ampoule boundaries to models focusing on the coupled transport phenomena occurring in the growing crystal. This has allowed the analysis of the effect of the furnace domain on the crystal growth domain. Many of these approaches stopped short of seeking a self-consistent multi-scale solution [112, 113]. Recent efforts by Derby and coworkers have been made to rectify this situation by coupling pre-existing computer codes to exploit the expertise of the standalone models into one, self-consistent, multi-scale model [114, 115, 116].

Development of process control for the VB/VGF systems has been extremely slow because very few system variables can be measured in real time and *in-situ*. Chin and Carlson [41] and Seidensticker et al. [117] used open-loop simulations to investigate the effects of temperature boundary conditions on interface shape and their suitability to a control algorithm. Azuma et al. [118] developed an automatic feedback control system to keep the temperature at the interface of silicon germanium, which is dependent on composition, during growth to control bulk composition. The ampoule translation rate was updated based on the position of the interface, which was detected automatically by images captured by an *in-situ* monitoring system via a charge-coupled-device camera. Sonda et al. [119, 120] studied the feasibility of using feedback control to suppress oscillatory flows via crucible rotation with numerical modeling on indium antimonide. Batur and co-workers [121, 122, 123] fashioned a transparent, multi-zone furnace for the production of lead bromide. A video camera and real-time imaging software was able to observe the melt-crystal interface shape through the transparent furnace. The temperature profile was adjusted by comparing the observed interface shape to the desired shape. A good overview of recent work of active growth control is provided by Lan [106].

1.5 Thesis overview

The purpose of this thesis is to study novel VB-based Electrodynamic Gradient Freeze Furnace for the improvement on CZT growth.

Chapter 2 continues the introductory material by presenting a two-dimensional mathematical model of a VB crystal growth system for semiconductor alloys. This model consists of conservation equations for heat, momentum, and mass transport with an accurate representation of the phase change boundary. Details of the furnace are entered as heat transfer boundary conditions. These equations form a set of time-dependent partial differential equations. The Galerkin finite element method is used to discretize the equations in the spatial coordinates, and an implicit trapezoidal time marching scheme is used to solve the temporal dependency. Newton's method is used to solve the resulting set of nonlinear algebraic equations. The governing equations and their implementation are discussed in detail.

In Chapter 3, a transient, coupled model has been developed to analyze the segregation of zinc in Cadmium Zinc Telluride (CZT) grown in an electrodynamic gradient freeze (EDG) furnace. The coupled model consists of a local model that solves for time-dependent

melt flow, heat transfer, melt-crystal interface position, and zinc distribution in both melt and solid phases and a quasi-steady-state global model that features realistic furnace heat transfer. After verification and validation tests, the model is applied to predict composition patterns in a large-scale CZT EDG growth system previously analyzed by Gasperino et al. (JCG 311, 2327 2335, 2009). Surprisingly, anomalous zinc segregation is predicted, featuring a non-monotonic axial concentration profile and several local minima and maxima across the boule. A mechanistic explanation is put forth based on the cumulative effect of changes in multi-cellular melt flow structures, a particularly susceptible occurrence for CZT systems. Additional effects of furnace translation rate and solid state diffusion are probed.

Chapters 4 and 5 explore two novel processing methods for VB growth of CZT. In Chapter 4, a realistic furnace model has been developed and applied to assess cadmium zinc telluride (CZT) interface shape dependency on thermal environments in the electrodynamic gradient (EDG) furnaces. A novel furnace thermal profile has been inspired by the traveling heater method and applied to the Vertical Bridgman process by numerical simulations. Compared to the traditional furnace profile, namely cold bottom and hot top, the novel bell curve thermal profile could change the interface shape from concave to convex towards melt. Further comparison of the results including the convection-dominated thermal field, the flow pattern transition and the heat flux transition in the melt between traditional thermal profile and bell curve profile reveal the undercurrent mechanism of the interface transformation. Due to the bell-curve profile, the typical Bénard convection cells occur and dominate the heat transfer in the melt, which could be seen by the thermal field results, and dramatically change the heat flow pattern and intensity from basically downward axial flux to the coexistence of dominated radial heat flux and strong upward heat flux on the top of the melt phase. This newfound results uncover the further possibility of the interface shape control via subtle model-based design and dynamic control of the furnace thermal field. And a theoretical dynamic control strategy based on the bell-curve profile has been investigated and validated our novel design of furnace gradients.

In Chapter 5, a realistic Electrodynamic Gradient (EDG) Furnace model has been developed and employed to analyze the thermal field and interface evolution of quenching process of Cadmium Zinc Telluride (CZT). A variety of quenching cases have been investigated with respect to the time-dependent heating profile served as a pre-growth degree of design within the accessible operation space regarding CZT crystal growth in such an untraditional manner. For such a quick process, the growth kinetics may present itself depending on the relative time scales and competence with thermodynamic equilibrium

within a further detailed theoretical model. However, the work presented here will focus on the thermal analysis without considering the solute-related constitutional supercooling and segregation effects. After a series of case studies, it has been found that the growth behavior, such as interface evolution, in quenching process is highly history-dependent, i.e., highly depending on the history of furnace heating power profile. Besides, compared to the typical growth rate of 1mm/hr, the quenching growth rate could be 10-100 times larger and even reach to 110 mm/hr in the final growth. Further work regarding convection effects and solute distribution will provide more information when assessing the potential application of quenching process to CZT growth. Upon this point, the experiments will provide more direct evidence to further justify such a process.

Sapphire single crystals are an important substrate for the fabrication of gallium-nitride light-emitting-diodes (LEDs) that emit white light. Theses solid-state devices promise great energy savings over both incandescent and compact fluorescent lighting technologies, and their market is expanding at double-digit growth rates. Key to continuing cost reduction for such LED-based lighting is reducing the cost of sapphire without compromising quality. The heat exchanger method (HEM) represents a possible yield improvement over existing growth technologies (primarily Kyropoulos growth) and is the subject of the study presented in Chapter 6.

We have performed quasi-steady state analysis using the commercial code CrysMAS to investigate the effects of furnace geometry and processing parameters on the temperature distribution, convection field, and melt-crystal interface shape during the crystal growth of sapphire by heat exchanger method (HEM). The temperature profile in the system is calculated to have lower temperatures both at the base of crucible and at the center top of the melt; however, the presence of convection flow arising from Marangoni force and buoyancy can ameliorate the latter effect. The interface shape is also predicted to change from flat to convex as crystal growth proceeds. Changes in geometry of furnace, such as altering the width and shape of crucible support, are shown to affect the thermal field significantly. Based upon such results, optimization of furnace design will be presented.

Chapter 7 concludes the thesis by providing a summary followed by a brief overview of possible research directions for the future.

Chapter 2

Numerical Simulation of Continuum Transport

2.1 Chapter Summary

The model developed in this chapter focuses on continuum transport phenomena occurring in materials processing, especially the growth of crystal from the melt. While many physical phenomena occur over a large range of length and time scales, we focus on continuum level mechanics in our model. Coupled transport phenomena of momentum, energy, and mass transfer and their attendant boundary conditions are simulated by discretization using the finite element method on a structured, rectangular mesh. Newton's method is then used to solve the resulting set of nonlinear, algebraic equations. A second-order trapezoid scheme is used to time-integrate the problem. The models presented here are all solved using the software code Crystallization and Transport Simulator, or Cats2D [124] developed by Yeckel and Goodwin.

2.2 Model and Governing Equations

The models employed in this thesis are developed to represent vertical Bridgman systems, where bulk crystals are grown by directional solidification from a molten phase. The solidification process occurs in a cylindrical container called an ampoule or crucible. A schematic diagram representing a basic vertical Bridgman system is provided in Figure 2.1. Raw material is placed within the ampoule which is then placed within a cylindrical furnace. The

raw material is then melted by setting the furnace temperature greater than the melting point temperature. Next, an axial temperature gradient is applied in the furnace along the external ampoule wall, where temperatures (relative to the melting point) are hotter on the top and lower toward the bottom. Solidification occurs by either vertically translating the ampoule down through the furnace as in traditional vertical Bridgman growth, or by varying heater powers to, in effect, translate the temperature gradient up the furnace as in a gradient freeze system.

Simulating an entire crystal growth furnace is extremely challenging due to the disparate length scales involved, and the multi-physics nature of the problem. In this chapter, we discuss our model which focuses on continuum transport phenomena that occurs solely in the growing crystal and its containing ampoule. Furnace effects are applied as boundary conditions along the outer ampoule wall.

Additional assumptions are made of the system to further reduce the complexity of our model. The ampoule (and the furnace) is assumed to be axisymmetric, or uniform in the azimuthal direction, to reduce the model from three to two dimensions. This greatly reduces the computational effort needed to solve a crystal growth problem. Furthermore, the frame of reference is fixed with respect to the center of the bottom of the ampoule. Zinc is considered a dilute species within the CdTe, allowing the system to be modeled as a binary mixture with binary diffusion coefficients. Material properties are assumed to be constant with respect to zinc concentration, which allows the species concentration equation to be decoupled from the heat and momentum transfer equations. All material properties are assumed to be independent of temperature and pressure, except for fluid density.

Figure 2.2 shows a computational domain of a Vertical Bridgman system. The computational domain consists of three regions: the melt (Ω_m), the solid crystal (Ω_s), and the ampoule (Ω_a). In addition to the three regions, there are also four distinct boundaries in the system. These boundaries are between the ampoule and furnace ($\delta\Omega_{af}$); ampoule and melt ($\delta\Omega_{am}$); ampoule and crystal ($\delta\Omega_{as}$); and the melt and crystal ($\delta\Omega_{ms}$). The origin of the cylindrical coordinates is the intersection of the ampoule and the crystal along the centerline.

The governing transport equations are derived from first principles as discussed in detail in [125], and are non-dimensionalized. Spatial coordinates are scaled by the inner radius of the ampoule, $L_o = R_i$. Temperature is defined relative to the melting point temperature T_{mp}. Concentration is non-dimensionalized by the initial zinc concentration within the melt, $c_o = c_i$. Time is scaled by viscous dissipation of the melt, and velocity is scaled by buoyancy.

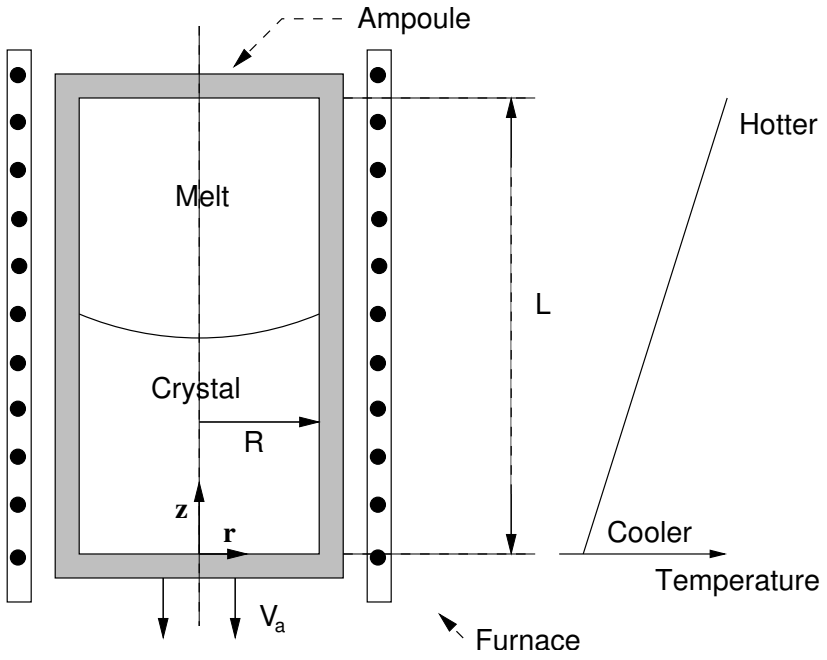

Figure 2.1: Schematic of the vertical Bridgman crystal growth system

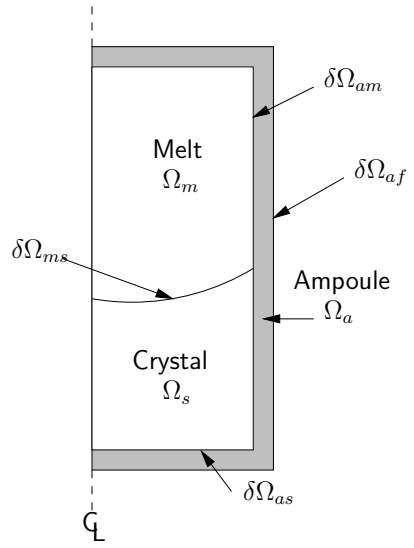

Figure 2.2: Schematic of the computational domain

Table 2.1: Characteristic values

Symbol	Description	Scale Factor	Comments
L_o	Length	R_i	Ampoule inner radius
T_o	Temperature	T_m	Melting point
V_o	Velocity	$\sqrt{\beta g L_o T_o}$	Based on vertical heated plate in an infinite bath
t_o	Time	$\frac{\rho L_o^2}{\mu}$	Viscous dissipation of melt
p_o	Pressure	$\frac{\mu V_o}{L_o}$	Based on melt dynamic viscosity
c_o	Concentration	c_i	Initial species concentration

Table 2.1 lists the characteristic values used to non-dimensionalize the field equations, where R_i is inner radius of ampoule, T_m is melting point, β is thermal expansivity of melt, g is gravitational constant,ρ is density of melt, μ is dynamic viscosity and c_i is initial species concentration.

2.2.1 Navier-Stokes Equations

Momentum conservation in the melt domain Ω_m is described by the Navier-Stokes (NS) equations for incompressible flow with the continuity constraint. The Boussinesq approximation is applied to encompass buoyancy effects. Using the characteristic quantities outlined in the previous section, the NS equations become:

$$\frac{\partial \mathbf{v}}{\partial t} + \sqrt{\mathrm{Gr}}\mathbf{v} \cdot \nabla \mathbf{v} = \nabla \cdot \mathsf{T} + \sqrt{\mathrm{Gr}}(1 - T)\mathbf{g}, \tag{2.1}$$

$$\nabla \cdot \mathbf{v} = 0 \tag{2.2}$$

where

$$\mathsf{T} \equiv -p\mathsf{I} + (\nabla \mathbf{v} + (\nabla \mathbf{v})^T) \tag{2.3}$$

T is the stress tensor, I is the identity tensor, p is the dynamic pressure, and $\mathbf{g}$ is a unit vector in the direction of gravity. The velocity vector contains the radial and axial velocities, $\mathbf{v} = (v_r, v_z)$. The Grashof number, $\mathrm{Gr} \equiv \rho^2 g L^3 T_o / \mu^2$, is the ratio of buoyancy force to viscous force acting on a fluid. In a Vertical Bridgman system momentum is convected by free convection driven by buoyancy effects.

In melt crystal growth systems, buoyant forces are extremely important in free convec-

tion due to density variation is the main driving force. With such nonisothermal systems, fluid density depends on temperature. To account for bouyant force, we insert an equation of state into the NS equations. Here we use the Boussinesq approximation equation of state which is a Taylor expantion of density with respect to density, $\rho(T)$ [125]. The approximation for $\rho(T)$ is substituted for the density term multiplying the gravity vector $\mathbf{g}$ only. Density can also change due to solute concentration differences. Since we assume it is a dilute solution, the buoyancy term depends solely on a constant multiple of the temperature gradient by β, the thermal expansivity of the melt.

To complete the NS equations, the appropriate boundary conditions must be applied. The no-slip boundary condition is applied along the ampoule/melt boundary ($\delta\Omega_{am}$) and the interface between melt and crystal ($\delta\Omega_{ms}$). :

$$\mathbf{v} = 0 \quad \text{on} \quad \delta\Omega_{am} \text{ and } \delta\Omega_{ms}. \tag{2.4}$$

Applying the no-slip boundary condition at the crystal/melt interface is a result of our assumption that the density of the melt and the crystal are not appreciably different. Under this assumption, the crystal melt freezes in place [83]. Symmetry conditions are applied along the system centerline, $r = 0$,

$$\mathbf{v} \cdot \mathbf{e}_r|_{r=0} = 0 \tag{2.5}$$

$$\left.\frac{\partial(\mathbf{v} \cdot \mathbf{e}_z)}{\partial r}\right|_{r=0} = 0 \tag{2.6}$$

where $\mathbf{e}_i$ is the unit vector in either the r- or z-direction.

In many systems, there is a gaseous overhead within the ampoule above the melt phase. A more specialized boundary condition is applied in such cases, which embodies the effects of surface tension at the interface. We use a simplified condition by assuming that the stress induced by the gas phase is negligible, such that the momentum balance in the gas phase is ignored. We further assume that gravity keeps the free boundary nearly flat, in which case the normal momentum balance is automatically satisfied, and only the tangential component must be accounted for. The force balance at the melt/gas interface becomes:

$$\mathbf{n} \cdot \mathsf{T}|_l = (\mathrm{Ma}\mathbf{t} \cdot \nabla T)\mathbf{t} \tag{2.7}$$

where Ma$\equiv \gamma_T T_o/\mu V_o$ is the Marangoni number, $\mathbf{t}$ is the unit tangent vector, μ is the

melt dynamic viscosity, and γ_T is the linear variation of surface tension with respect to temperature. This tangential stress caused by the surface tension gradient is known as the Marangoni effect [83].

2.2.2 Conservation of Energy

Energy transport occurs by conduction and convection within the melt, and conduction within the crystal and ampoule. The non-dimensional form of the energy conservation equation is

$$\mathrm{Pr}_m \frac{\partial T}{\partial t} + \mathrm{Pe}_{t,m} \mathbf{v} \cdot \nabla T = \nabla^2 T \tag{2.8}$$

in the melt, and

$$\mathrm{Pr}_i \frac{\partial T}{\partial t} = \nabla^2 T \tag{2.9}$$

in all other materials, where the index m indicates the melt phase, and i designates the solid crystal s or ampoule a. The energy conservation equation is scaled using an assumption of natural convection. The Prandtl number is defined as $\mathrm{Pr}_i \equiv \nu_m/\alpha_i$ where ν_m is the kinematic viscosity of the melt, and $\alpha_i \equiv k_i/\rho_i Cp_i$ is the thermal diffusivity of phase i, and used as a measure of the viscous diffusivity to the heat diffusivity. The thermal Peclet number, $\mathrm{Pe}_{m,i} \equiv V_o L_o/\alpha_i$, is a measure of the convective heat transport to the diffusive heat transport. The characteristic values of velocity, V_o, and length, L_o are defined in Table 2.1.

Latent heat of fusion is released at the melt-crystal interface, $\delta\Omega_{ms}$, upon crystallization as a function of the local interface velocity. Therefore, the Stefan or latent-heat boundary condition is applied:

$$\mathbf{n} \cdot (-\kappa \nabla T|_s + \nabla T|_m) = \Lambda \mathrm{Pr}_m \mathrm{Sf}_m \mathbf{n} \cdot \mathbf{V}_{ms} \quad \text{at} \quad \delta\Omega ms \tag{2.10}$$

where the variables and operators are in non-dimensional. $\kappa = \mathrm{k}_s/\mathrm{k}_m$ is the ratio of thermal conductivities, $\Lambda = \rho_s/\rho_m$ is the density ratio, and $\mathbf{V}_{ms} = \partial \mathbf{x}/\partial t$ is the velocity of the melt-crystal interface. As can be seen in Equation (2.10), $\partial \mathbf{x}/\partial t$ is non-dimensionalized by ν/L_o. The Stefan number, $\mathrm{Sf}_i \equiv H_f/C_{p,i}T_o$, is the ratio of latent heat to heat capacity, where H_f is the latent heat and $C_{p,i}$ is the heat capacity of phase i.

In addition to the Stefan condition, a melting-point isotherm condition is applied at the melt-crystal interface, which implicitly sets the shape of this boundary. The isotherm condition sets the location of the interface as that of the melting point temperature T_{mp}. Since the temperature is defined relative to T_{mp}, the boundary condition becomes

$$T = T_{mp} = 1 \quad \text{at} \quad \delta\Omega ms \tag{2.11}$$

Furnace contributions to heat transfer are included by a boundary condition along the external ampoule wall $\delta\Omega_{ag}$. In experimental vertical Bridgman growth, many different furnace temperature profiles are utilized in crystal growth. For illustrative purposes, we will employ a furnace temperature profile that is linear with axial position:

$$T_f = T_{mp} + \frac{T_H - T_L}{z_H - z_L}(z - z_{mp}) + V_a t \tag{2.12}$$

where T_f is the furnace temperature, z_H is the axial position of the top of the ampoule, z_L is the bottom of the ampoule, and T_H and T_L are the corresponding temperatures ($T_L < T_H$). A reference position, z_{mp}, is set as the axial location of the melting point temperature. The time dependent term simulates translation of the ampoule through the furnace, with V_a as the ampoule translation rate. Heat flux at the external ampoule wall includes a convective heat term and a radiative flux term:

$$\mathbf{n} \cdot \nabla T = h(T - T_f) + \mathrm{Rd}(T^4 - {T_f}^4) \quad \text{at} \quad \delta\Omega_{af} \tag{2.13}$$

where $\mathbf{n}$ is the unit normal vector, h is the dimensionless heat transfer coefficient (Biot number), Rd is the radiation number defined as $\mathrm{Rd} \equiv \epsilon_i \sigma L_o {T_o}^3 / k_i$ (ϵ_i is the emissivity and σ is the Stephan-Boltzmann constant, k_i is thermal conductivity), and $T_f(z,t)$ is the applied, dimensionless, furnace temperature defined above.

As with the momentum balance, a symmetry condition is applied at the system centerline:

$$\left.\frac{\partial T}{\partial r}\right|_{r=0} = 0 \tag{2.14}$$

Temperature is assumed to be continuous across all system boundaries.

2.2.3 Conservation of Mass

Similar to the energy transport equation, mass transport is described by a convection-diffusion equation. Zinc is assumed to be a dilute species in CdTe, and is subject to pseudo-binary conservation equations:

$$\mathrm{Sc}_m \frac{\partial c}{\partial t} + \mathrm{Pe}_{m,m}\mathbf{v} \cdot \nabla c = \nabla^2 c \tag{2.15}$$

in the melt, and

$$\mathrm{Sc}_s \frac{\partial c}{\partial t} = \nabla^2 c \tag{2.16}$$

in the CZT solid, where c is dimensionless concentration of zinc. The Schmidt number, $\mathrm{Sc}_i \equiv \nu/D_i$, is a measure of viscous to species diffusivity. The mass Peclet number, $\mathrm{Pe}_m, i \equiv V_o L_o/D$, measures the convective species transport of the diffusive species transport. ν is kinematic viscosity, D_i is diffusion coefficient. In both dimensionless quantities, i indicates phase.

Segregation boundary conditions that are analogous to the Stefan and the isotherm boundary condition are imposed as the melt-crystal interface:

$$\mathbf{n} \cdot (-\nabla c|_m + D\nabla c|_s) = \mathrm{Sc}_m(1-K)\mathbf{n} \cdot \mathbf{V}_{ms} \quad \text{at} \quad \delta\Omega_{ms} \tag{2.17}$$

$$c|_s = Kc|_m \quad \text{at} \quad \delta\Omega_{ms} \tag{2.18}$$

where $D = D_s/D_m$ and K is the equilibrium segregation coefficient and $\mathbf{V}_{ms} = \partial\mathbf{x}/\partial t$ is the velocity of the melt-crystal interface.

Again, a symmetry condition is applied at the system centerline

$$\left.\frac{\partial c}{\partial r}\right|_{r=0} = 0. \tag{2.19}$$

Furthermore, the melt-ampoule interface, crystal-ampoule interface, ampoule are assumed to be impermeable to solute transport:

$$\mathbf{n} \cdot \nabla c = 0 \quad \text{on} \quad \delta\Omega_{am} \text{ and } \delta\Omega_{as} \tag{2.20}$$

$$c = 0 \quad \text{in} \quad \Omega_a. \tag{2.21}$$

2.3 Numerical Implementation

The equations governing macroscopic transport in the vertical Bridgman growth system are a set of nonlinear, coupled, partial differential equations (PDE). Due to the complexity of the equations, it is not possible to solve them analytically, therefore they are solved numerically. The computational domain is spatially discretized, or partitioned, into small elements. The PDEs are spatially discretized based on the domain discretization. The Galerkin Finite Element Method (GFEM) is used to discretize the PDEs, and time is integrated using numerical techniques [126]. Discretization of the equations transforms the equations from PDEs to ordinary differential equations (ODEs). The goal of this thesis is not to be an account of the many intricacies of GFEM, but on how this method can be used to model a crystal growth system. For a more detailed exposition on how to apply GFEM to fluid dynamics problems, the reader is referred to [126, 127].

2.3.1 Discretization of Computational Domain

To solve PDEs using the finite element method, the computation domain is first discretized. Figure 2.3 shows how a one dimensional domain is discretized. The domain is divided into smaller subdomains called elements, while the endpoints of each element are defined by nodes. The collection of elements and nodes is called a "mesh". Discretizing a two dimensional computational domain is an extension of the one dimensional example. For quadrilateral elements, each element is defined by four corner nodes.

The computational domain of the vertical Bridgman growth system has an added complication of different materials making up the domain. Also, not all transport mechanisms apply throughout the domain. Therefore, the domain is divided into large subdomains representing different regions of the problem, i.e. the melt, crystal, and ampoule which are in turn divided by elements.

As the number of elements and also the order of basis functions are increased, the accuracy of the approximate solution increases. In the limit as the elements become infinitely small by further increasing the density of mesh, the "true" solution is achieved. The increase in accuracy comes at the extremely increased cost of computational resources and time. Therefore, a compromise must be made between accuracy and available resources.

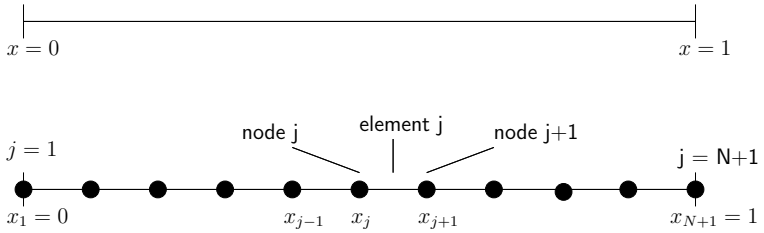

Figure 2.3: Example of a discretized domain in one dimension

2.3.2 Discretization of Unknowns

The unknowns (velocity, pressure, temperature, and concentration) are represented as a linear combination of finite element basis functions. These basis functions, ϕ^i and ψ^i, are contained within the Sobolev space $\mathcal{H}$ [126] defined as:

$$\mathcal{H} = \{w : \int_\Omega |\nabla w|^2 dx < \infty \text{ and } w = 0 \text{ for } w \in \Omega\} \tag{2.22}$$

where Ω is a domain, $\delta\Omega$ its boundary, and w a basis function. The basis functions used here are Lagrange polynomials

- Q_2 polynomials: biquadratic and continuous
- P_1 polynomials: linear and continuous
- P_{-1} polynomials: linear and discontinuous

which belong to the Sobolev space.

Furthermore, the basis function is non-zero only in the elements that share a given node, and zero over the rest of the domain making a set of nearly orthogonal functions. At the node itself ($node^i$), the basis function is unity and zero at all other nodes. The velocity field, $\mathbf{v}$, is then approximated as

$$\mathbf{v}(t, \mathbf{x}) \approx \hat{\mathbf{v}} = \sum_{j=1}^{N_v} \mathbf{v}^j(t)\phi_v^j(\mathbf{x}) \tag{2.23}$$

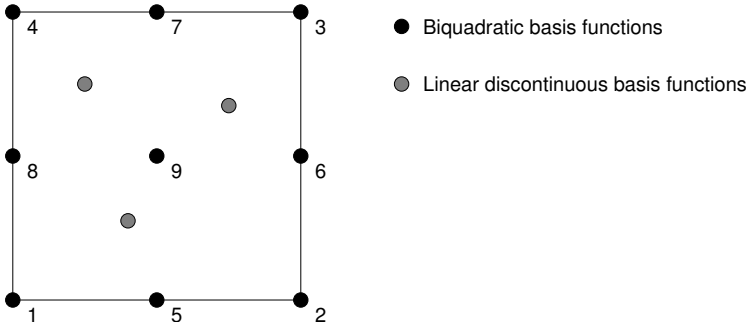

Figure 2.4: A sample element and its nodes. Dark nodes are associated with biquadratic basis functions, and light nodes are associated with linear discontinuous basis functions.

where $\mathbf{v}^j$ is the unknown velocity at the j^{th} node, N_v is number of nodes in the melt subdomain, and $\mathbf{x}$ is the position vector. The concentration is approximated as

$$c(t,\mathbf{x}) \approx \hat{c} = \sum_{j=1}^{N_c} c^j(t)\phi_c^j(\mathbf{x}) \tag{2.24}$$

where c^j is the concentration at the j^th node and N_c is the number of nodes in the melt and crystal subdomains. Similarly, the temperature is approximated as

$$T(t,\mathbf{x}) \approx \hat{T} = \sum_{j=1}^{N_T} T^j(t)\phi_T^j(\mathbf{x}) \tag{2.25}$$

were T^j is the temperature at the j^th node, and N_T is the number nodes over the entire domain. The basis functions used to represent velocity, concentration, and temperature are biquadratic. The domain is represented by nine nodes per element.

The pressure cannot be approximated in the same manner as the above field variables. Pressure does not appear in the continuity equation (Equation (2.2)), and only its gradient appears in the momentum equation (Equation (2.1)). Therefore, the pressure cannot be solved explicitly and creates an underlying constraint of the momentum equation. The constraint is overcome by "enriching" the velocity space by either adding extra velocity nodes or minimizing the number of pressure nodes. This technique is known as the "inf-sup" or "Babuska-Brezzi" condition. Elements that pass the stability test will converge "optimally" and without spurious pressure behavior. Those failing the test *may* not converge [127]. With quadrilateral elements, a good choice is to apply linear discontinuous basis

Table 2.2: Types of basis functions

Unknown	Symbol	Basis Function	Type
$\mathbf{v}$	velocity	ϕ_v	continuous, biquadratic
p	pressure	ψ_p	discontinuous, linear
T	temperature	ϕ_T	continuous, biquadratic
c	concentration	ϕ_c	continuous, biquadratic
ξ	nodal position	$\phi^k(\xi,\eta)$	continuous, bilinear
η	nodal position	$\phi^k(\xi,\eta)$	continuous, bilinear

functions, ψ^i, and three degrees of freedom per elements, which are associated with the value of the pressure and pressure gradient at the element center,

$$p(t,\mathbf{x}) \approx \hat{p} = \sum_{j=1}^{N_p} p^j(t)\psi_p^j(\mathbf{x}). \tag{2.26}$$

Figure 2.4 shows a schematic of a sample element and its associated nodes.

The spatial and temporal dependencies of the unknowns are divided between the basis functions and their coefficients. For example, temperature is discretized as in Equation (2.25). The temperature's spatial dependency is captured by the basis functions $phi_T^j(x)$, and its temporal dependency by the coefficients $T^j(t)$. Therefore, the spatial and time derivatives of the temperature are approximated as:

$$\frac{\partial T}{\partial x}(t,\mathbf{x}) \approx \sum_{j=1}^{N_T} T^j \frac{d\phi_T^j}{d\mathbf{x}} \tag{2.27}$$

$$\frac{\partial T}{\partial t}(t,\mathbf{x}) \approx \sum_{j=1}^{N_T} \frac{dT^j}{dt}\phi_T^j \tag{2.28}$$

The discretized unknowns and their derivatives are substituted into the governing equations resulting in a set of discretized PDEs. Table 2.2 summarizes the types of basis functions used in this model.

2.3.3 Weighted Residual Equations

Finite element methods comprise a subset of the method of weighted residuals [128], the goal of which is to obtain an approximate solution by minimizing the error between the exact

solution and the numerical approximation. To accomplish this, the equation in residual form (all of the terms are moved to the same side) is made orthogonal to a set of weighting functions that are mutually orthogonal. If the residual is orthogonal to a complete set of weight functions, then the residual itself is equal to zero and the solution to the equations is found [126]. The weighted residual, $\mathcal{R}$ has the form

$$\mathcal{R} = \int w f(x) dx = 0 \qquad \forall\ w \tag{2.29}$$

where w is the weight function, and $f(x)$ is the residual.

It is not always feasible to use a complete set of mutually orthogonal weighting functions, so a nearly complete, finite set $\mathcal{W}$ is used instead. The basis functions used to discretize the unknowns is a set of nearly orthogonal basis functions. GFEM uses these basis functions as weighting functions [126]: $w = \phi^i$ or ψ^i.

The transport equations are put into residual form, multiplied by the weight functions, and integrated over the computational domain. The weighted residuals of the governing equations are:

$$\underline{\mathcal{R}}^k_{\mathbf{v}} = \int_V \phi^k_v (\frac{\partial \hat{\mathbf{v}}}{\partial t} + \sqrt{\mathrm{Gr}}\mathbf{v} \cdot \nabla \hat{\mathbf{v}} - \nabla \cdot \hat{\mathsf{T}} - \sqrt{\mathrm{Gr}}(1 - \hat{T})\mathbf{g}) dV = 0 \quad \text{(momentum)} \tag{2.30}$$

where $\hat{\mathsf{T}} = -\hat{p}\mathsf{I} + (\nabla \hat{\mathbf{v}} + (\nabla \hat{\mathbf{v}})^T)$

$$\mathcal{R}^k_p = \int_V \psi^k_p (\nabla \cdot \mathbf{v}) dV = 0 \quad \text{(continuity)} \tag{2.31}$$

$$\mathcal{R}^k_T = \int_V \phi^k_T (\mathrm{Pr}_i \frac{\partial \hat{T}}{\partial t} + \mathrm{Pe}_{t,i} \hat{\mathbf{v}} \cdot \nabla \hat{T} - \nabla^2 \hat{T}) dV = 0 \quad \text{(energy)} \tag{2.32}$$

$$\mathcal{R}^k_c = \int_V \phi^k_c (\mathrm{Sc}_i \frac{\partial \hat{c}}{\partial t} + \mathrm{Pe}_{m,i} \hat{\mathbf{v}} \cdot \nabla \hat{c} - \nabla^2 \hat{c}) dV = 0 \quad \text{(species)}. \tag{2.33}$$

where V indicates volume integrals in real space. Note that the weighting functions in the continuity equation are the pressure basis functions. The pressure acts as a Lagrange multiplier for the incompressibility constraint by "adjusting itself" instantaneously in time and everywhere in space [127].

The next step in the GFEM is to recast the above equations into the weak form, also known as the variational form. Converting the equations to the weak form reduces the order of the derivatives which increases the accuracy of the equation. The equations are put into

the weak form using the identity chain rule:

$$\nabla \cdot \phi_T^k \nabla \hat{T} = \nabla \phi_T^k \cdot \nabla \hat{T} + \phi_T^k \nabla^2 \hat{T}, \tag{2.34}$$

and the divergence theorem of Green, Gauss, and Ostrogradskii (GGO):

$$\int_V \nabla \cdot \phi_T^k \nabla \hat{T} dV = \int_A \phi_T^k \mathbf{n} \cdot \hat{T} dA. \tag{2.35}$$

where A indicates an area integral. The volume integral over $\phi \nabla^2 \hat{T}$ becomes:

$$\int_V \phi_T^k \nabla^2 \hat{T} dV = -\int_V \nabla \phi_T^k \cdot \nabla \hat{T} dV + \int_A \phi_T^k \mathbf{n} \cdot \nabla \hat{T} dA. \tag{2.36}$$

This procedure is analogous to integration by parts in one dimension. The governing equations in weak form are:

$$\underline{\mathcal{R}}_{\mathbf{v}}^k = \int_V \phi_v^k (\frac{\partial \hat{\mathbf{v}}}{\partial t} + \sqrt{\mathrm{Gr}} \mathbf{v} \cdot \nabla \hat{\mathbf{v}} - \sqrt{\mathrm{Gr}}(1 - \hat{T})\mathbf{g}) dV + \int_V \nabla \phi_v^k \cdot \hat{\mathsf{T}} dV - \int_A \phi_v^k (\mathbf{n} \cdot \hat{\mathsf{T}}) dA = 0 \qquad \text{(momentum)} \tag{2.37}$$

$$\mathcal{R}_p^k = \int_V \psi_p^k (\nabla \cdot \mathbf{v}) dV = 0 \qquad \text{(continuity)} \tag{2.38}$$

$$\mathcal{R}_T^k = \int_V \phi_T^k (\mathrm{Pr}_i \frac{\partial \hat{T}}{\partial t} + \mathrm{Pe}_{t,i} \hat{\mathbf{v}} \cdot \nabla \hat{T}) dV + \int_V \nabla \phi_T^k \cdot \nabla \hat{T} dV - \int_A \phi_T^k (\mathbf{n} \cdot \nabla \hat{T}) dA = 0 \qquad \text{(energy)} \tag{2.39}$$

$$\mathcal{R}_c^k = \int_V \phi_c^k (\mathrm{Sc}_i \frac{\partial \hat{c}}{\partial t} + \mathrm{Pe}_{m,i} \hat{\mathbf{v}} \cdot \nabla \hat{c}) dV + \int_V \nabla \phi_c^k \cdot \nabla \hat{c} dV - \int_A \phi_c^k (\mathbf{n} \cdot \nabla \hat{c}) dA = 0 \qquad \text{(species).} \tag{2.40}$$

Equations (2.37)-(2.40) make up the set of differential algebraic equations used in GFEM to solve the problem. Note that the residual equation for momentum is a vector, $\underline{\mathcal{R}}_{\mathbf{v}}$ with a component for each velocity direction.

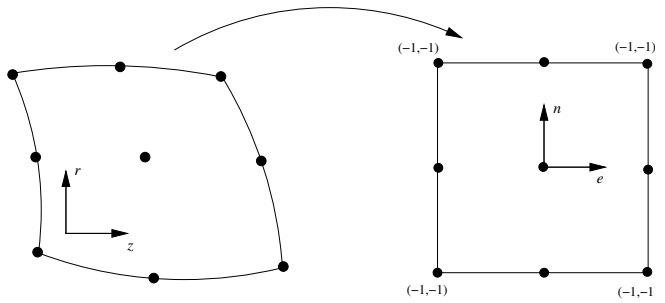

Figure 2.5: Parametric mapping to a unit square parent element

The types of boundary conditions are natural (flux), essential (Dirichlet). Flux boundary conditions are used in the surface integrals of the weak form. Essential boundary conditions replace the entire residual equation. For example, applying the flux boundary condition Equation (2.20) of impermeable solute transport to the surface integral Equation (2.40)

$$\int_A \phi^k(\mathbf{n}\cdot\nabla\hat{c})dA = 0 \quad \text{on} \quad \delta\Omega_{am}, \delta\Omega_{as}. \tag{2.41}$$

The isotherm boundary condition is an example of an essential boundary condition:

$$\mathcal{R}_T^k = \int_A \phi^k(\hat{T} - T_{mp})dA = 0. \tag{2.42}$$

The integrals of the weak form are evaluated numerically using Gaussian quadrature. Also the isoparametric mapping is used to "map" the arbitrary, computational elements in r, z to a square parent element in ξ, η coordinates, as in Figure 2.5. This mapping is given by:

$$(z, r) = \sum_{k=1}^{N_{el}} (z^k, r^k)\phi^k(\xi, \eta) \tag{2.43}$$

where $\phi^k(\xi, \eta)$ are basis function as described in [126], r^k, z^k are the nodal coordinates in the computational domain, and N_{el} is the number of nodes per element.

Isoparametric mapping also allows us to transform volume and area integrals from real space to parent element space using:

$$\int_V (\ldots)dV = \int_{-1}^{1} (\ldots)rJd\xi d\eta; \quad J = \frac{\partial x}{\partial \xi}\frac{\partial y}{\partial \eta} - \frac{\partial x}{\partial \eta}\frac{\partial y}{\partial \xi}, \tag{2.44}$$

where $r = 1$ for planar coordinates and $r =$ radius for cylindrical coordinates. The transformation Jacobian, J is computed using Equation (2.43), and the integrals are evaluated using 3×3 Gaussian quadrature [129].

Area integrals on boundaries of constant η are transformed using:

$$\int_A (\ldots) dA = \pm \int_{-1}^{1} (\ldots) r S_\xi d\xi; \quad S_\xi = \sqrt{\left(\frac{\partial x}{\partial \xi}\right)^2 + \left(\frac{\partial y}{\partial \xi}\right)^2} \tag{2.45}$$

The leading sign is positive for $\eta = -1$, and negative for $\eta = 1$. Area integrals on boundaries of constant ξ are transformed using:

$$\int_A (\ldots) dA = \pm \int_{-1}^{1} (\ldots) r S_\eta d\eta; \quad S_\eta = \sqrt{\left(\frac{\partial x}{\partial \eta}\right)^2 + \left(\frac{\partial y}{\partial \eta}\right)^2} \tag{2.46}$$

where the leading sign is positive for $\xi = 1$ and negative for $\xi = -1$. The signs are determined by the convention that line integrals proceed counter-clockwise over the domain. S_ξ and S_η are computed using Equation (2.43), and the area integrals are evaluated using 3 point Gaussian quadrature. By implementing isoparametric mapping, the residual integrals are computed easily and efficiently using generic code structure.

2.3.4 Deforming Boundary

Difficulty arises in accurately defining the melt-crystal interface. The interface shape is not known *a priori* and may change as the crystal grows [83]. In this work, a deforming mesh is used in order to compensate for the moving boundary. The initial mesh is generated by an algebraic method that uses quadrilateral elements. The mesh deforms according to the strategy known as elliptic mesh generation proposed by Winslow [130], and applied as by Christodoulou and Scriven [131] with boundary conditions developed by de Santos [132]. Elliptic mesh generation parameterizes the node locations using a pair of elliptic partial differential equations. For two dimensions,

$$\nabla \cdot D_\xi \nabla \xi = 0 \tag{2.47}$$

$$\nabla \cdot D_\eta \nabla \eta = 0 \tag{2.48}$$

where D_ξ and D_η are node diffusivities that control the refinement of the mesh. For a non-uniform mesh, the diffusivities are not constant. The diffusivities can be calculated

from an initial mesh that is generated algebraically:

$$D_\xi = \frac{\partial S}{\partial \xi} = \sqrt{\left(\frac{\partial r}{\partial \xi}\right)^2 + \left(\frac{\partial z}{\partial \xi}\right)^2}, \quad D_\eta = \frac{\partial S}{\partial \eta} = \sqrt{\left(\frac{\partial r}{\partial \eta}\right)^2 + \left(\frac{\partial z}{\partial \eta}\right)^2} \tag{2.49}$$

In this manner, the relative distribution of elements sizes is preserved while the domain deforms.

The residual elliptic mesh equations, Equations (2.47) and (2.48), are also put into weighted residual form. The basis functions used in isoparametric mapping are used as the weight functions:

$$\int_V \phi^k \nabla \cdot (D_\xi \nabla \xi) dV = 0 \tag{2.50}$$

$$\int_V \phi^k \nabla \cdot (D_\eta \nabla \eta) dV = 0 \tag{2.51}$$

The residual equations are written such that the computational coordinates (ξ,η) are dependent on the physical coordinates (z,r). In practice, it is necessary to perform a coordinate transformation so that (ξ, η) are the independent variables.

The time derivatives also need to be rewritten to accommodate the moving mesh. In the continuous governing equations, the time derivatives are taken with respect to the computational domain reference frame or Eulerian frame. On the other hand, the time derivatives of the basis function coefficients in the discretized equations are taken with respect to the parent element frame which moves at the velocity of the nodes. The time derivatives in the discretized frame are converted from the Eulerian frame to the parent element frame:

$$\frac{\partial \hat{\mathbf{v}}}{\partial t} = \dot{\mathbf{v}} - \dot{\mathbf{x}} \cdot \nabla \hat{\mathbf{v}}, \tag{2.52}$$

$$\frac{\partial \hat{T}}{\partial t} = \dot{T} - \dot{\mathbf{x}} \cdot \nabla \hat{T}, \tag{2.53}$$

$$\frac{\partial \hat{c}}{\partial t} = \dot{c} - \dot{\mathbf{x}} \cdot \nabla \hat{c}, \tag{2.54}$$

where the overdot indicates time derivatives with respect to the parent element frame which is analogous to the material derivative in Reynolds transport theorem. Figure 2.6 shows an example of a mesh with a deformed boundary at the melt-crystal interface.

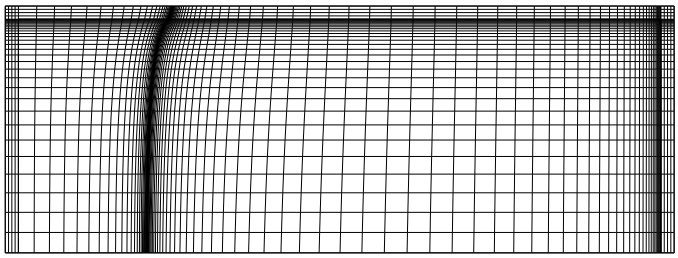

Figure 2.6: Sample mesh with deformed boundary at melt-crystal interface.

2.3.5 Quasi-steady state solution

The unknowns (velocity, pressure, temperature, and concentration) have both spatial and temporal dependencies. By approximating the unknowns as a linear combination of spatially dependent basis functions and temporally dependent coefficients, the dependencies are decoupled. However, the spatial and temporal dependencies in the discretized governing equations need to be separated. Then, instead of solving an initial value/boundary value problem (IBVP), the equations are of the initial value problem (IVP) form:

$$\mathbf{M}\frac{d\mathbf{q}}{dt} = \mathbf{F}(\mathbf{q}) \tag{2.55}$$

where $\mathbf{q}$ is the vector of unknowns

$$\mathbf{q}^j = \begin{bmatrix} v_r^j \\ v_z^j \\ p^j \\ T^j \\ c^j \\ \xi^j \\ \eta^j \end{bmatrix} \tag{2.56}$$

for $j = 1...N$ where N equals the total number of nodes. In the crystal solid and ampoule domains, $v_r^j = v_z^j = p^j = 0$. $\mathbf{M}$ is known as the mass matrix and $\mathbf{F}$ is a nonlinear vector function of the terms that do not have time derivatives of the unknowns in $\mathbf{q}$.

At steady state, the residual equation corresponding to Equation (2.55) is

$$\mathbf{R}_{ss} = \mathbf{F}(\mathbf{x}_{ss}) \tag{2.57}$$

where $\mathbf{R}$ is the vector of residual equations. These nonlinear residuals are linearized about a specific vector $\mathbf{q}_n^{(k)}$:

$$\mathbf{J}(\mathbf{q}_n^{(k)})\delta^{(k+1)} = -\mathbf{R}(\mathbf{q}_n^{(k)}) \tag{2.58}$$

where n denotes the time step value, and k denotes the iteration count at time step n. The Jacobian matrix, $\mathbf{J}(\mathbf{q}_n^{(k)})$, is defined as:

$$J_{ij} = \frac{\partial R_i}{\partial q_j} \tag{2.59}$$

where the subscripts i and j denote row and column indices, respectively; R_i is the i^{th} component of vector $\mathbf{R}$; and q_j is the j^{th} component of vector $\mathbf{q}$. The solution update vector, $\delta^{(k+1)}$, is defined by

$$\mathbf{q}^{(k+1)} = \mathbf{q}^{(k)} + \delta^{(k+1)} \tag{2.60}$$

The converged solution of the previous time step is used as the initial guess for each iteration. The iterations continue until the L_2 norm of the residual vector and the solution update vector are both less than specified error tolerances:

$$\|\mathbf{R}(\mathbf{q}_n^{(k+1)})\|_2 = \sqrt{\sum_{i=1}^{N} |\mathbf{R}_i(\mathbf{q}_n^{(k+1)})|^2} < \epsilon_1, \tag{2.61}$$

$$\|\delta^{(k+1)}\|_2 = \sqrt{\sum_{i=1}^{N} |\delta_i^{(k+1)}|^2} < \epsilon_2 \tag{2.62}$$

The linearized matrix problem in Equation (2.58) is put into LU-decomposition form using a direct solver method called the frontal solver developed by Hood [133]. The Jacobian matrix $\mathbf{J}$ is sparse due to the fact that the basis functions are nearly orthogonal. The product of the basis functions and their derivatives are non-zero only when multiplying basis functions corresponding to adjacent nodes. Gauss elimination can be performed as soon as all of the rows and columns involving the current element are constructed. In this manner, Gauss elimination is confined to the submatrix of rows and columns corresponding to nodes not yet eliminated but interact with the node being assembled. These nodes, called active variables, form a front that moves along the region hence the name frontal method.

2.3.6 Time Integration

With the equations rewritten as an IVP (Equation (2.55)), time is integrated using a numerical scheme. Integration, though, is difficult because the mass matrix, $\mathbf{M}$ is singular due to the lack of time derivatives for the pressure and the nodal positions. Additional difficulty arises from the nonlinearity of the equations. Therefore, an implicit time integration method is used. The method used here is the implicit trapezoid rule (TR) with a fixed timestep which is second-order accurate. This technique, adapted from Gresho [134], is unconditionally stable with respect to time step. Since TR depends on the derivative of the previous time step, the first time integration step of Equation (2.55) is done with Implicit Euler (IE):

$$\mathbf{M}(\mathbf{q}_1)\left[\frac{1}{\Delta t}(\mathbf{q}_1 - \mathbf{q}_0)\right] - \mathbf{F}(\mathbf{q}_1) = 0 \tag{2.63}$$

where the subscripts refer to time steps. The initial condition, $\mathbf{q}_0$, is obtained from a quasi-steady state solution of the governing equations $\mathbf{F}(\mathbf{q}_0) = 0$. In the subsequent steps, TR is used:

$$\mathbf{M}(\mathbf{q}_n)\left[\frac{2}{\Delta t}(\mathbf{q}_n - \mathbf{q}_{n-1}) - \left(\frac{d\mathbf{q}}{dt}\right)_{n-1}\right] - \mathbf{F}(\mathbf{q}_n) = 0 \tag{2.64}$$

For $n = 2$, the derivative $(d\mathbf{q}/dt)_{n-1}$ is calculated using IE:

$$\left(\frac{d\mathbf{q}}{dt}\right)_1 = \frac{1}{\Delta t}(\mathbf{q}_1 - \mathbf{q}_0) \tag{2.65}$$

while for $n > 2$ the derivative $(d\mathbf{q}/dt)_{n-1}$ is based on TR:

$$\left(\frac{d\mathbf{q}}{dt}\right)_{n-1} = \frac{2}{\Delta t}(\mathbf{q}_{n-1} - \mathbf{q}_{n-2}) + \left(\frac{d\mathbf{q}}{dt}\right)_{n-2} \tag{2.66}$$

The solution vector, $\mathbf{q}_n$, in Equations (2.63) and (2.64) is solved by using modified Newton-Raphson method. The governing equations, after discretization by the method of lines, are rearranged into residual form. As with the weighted residuals, we want to have an expression of the error, or residual, and minimize this error. Equations (2.63) and (2.64) are already written in residual form.

Modified Newton-Raphson method uses a single LU-decomposition for several iterations and for several time steps. A new LU-decomposition is done when the ratio of the L_2 norms of consecutive residual vectors is less than a tunable parameter (≤ 1). Typically iterations continue until the L_2 norm of both the residual and solution update vectors are less than

10^{-4} times the L_2 norm of the solution vector.

2.4 Numerical Codes

The numerical model presented in this chapter was generated using the Crystallization and Transport Simulator (Cats2D) code, developed by Andrew Yeckel and Ralph Goodwin [124].

In order to develop the complex, realistic furnace model, the crystal growth simulation software CrysMAS, developed by the Crystal Growth Laboratory of the Fraunhofer Institute of Integrated Systems and Device Technology (IISB) in Erlangen, Germany [135, 136, 137], was employed, which is capable of predicting high temperature heat transfer within complex crystal growth furnace by solving the energy conservation equations based on an unstructured triangular grid of finite volume method . Furthermore, the radiation heat transfer calculations are coupled and implemented by employing view factors and an enclosure method. Besides, CrysMAS can also perform the heat transfer, melt flow and phase change simulations within the crucible by applying the structured grid method. The interface between melt and crystal is tracked to coincide with the melting-point isotherm and also sets the vertices on the appropriate boundary between the structured and unstructured mesh. The inverse calculations are employed where the furnace set point temperatures are specified and the heater powers are solved as unknowns when performing a quasi-steady state calculation, which will server as the initial condition to the following transient simulation of rapid solidification process of CZT crystal growth. A quasi-Newton iterative method is employed in CrysMAS to arrive at a converged solution.

Physically, the model developed here is based on Mellen electrodynamic gradient freeze (EDG) furnaces with 18 controlled heating zones (12 one-element zones and six four-element zones). A schematic diagram of the computational domain for the model, showing the location of thermocouple set points and a representation of the finite volume mesh, is presented in Figure 2.8. Due to this elegant design of the heating system, it is feasible to design the thermal environment by setting the heating zone temperature or the power profile of heating elements in order to control the growth rate and interface shape between the melt and crystal. And with the help of the inverse calculations of CrysMAS, we could implement and testify a series of new designs not by experiments but by numerical simulations which is faster, less expensive and more accurate to establish the relationship between interface shape and thermal environment along the ampoule. Besides, the pyrolytic boron nitride (PBN) crucible is used in the furnace, which is highly anisotropic with respect to thermal

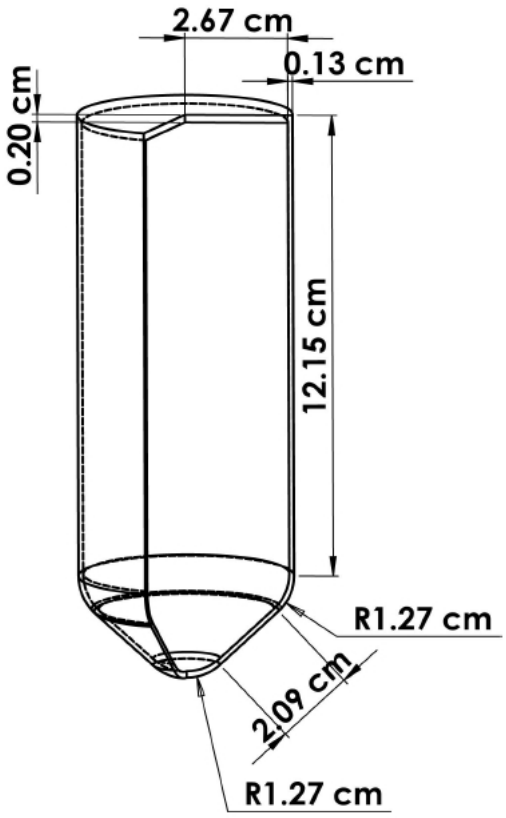

Figure 2.7: Schematic of PBN crucible employed in the model.

conductivity, namely, the conductivity parallel to the wall, the (a)-direction, is more than 25 times greater than the conductivity normal to the wall, the (c)-direction (Figure 2.7). Due to the axial symmetry of the experimental furnace, a simplified two-dimensional model representation is applied, with the vertical system axis assumed to be aligned with gravity. Void space between the melt and crucible lid is modeled as cadmium vapor with constant physical properties. Convection of the cadmium vapor is not accounted for in this model. Physical properties for materials used in the furnace are assumed to be constant with temperature [138].

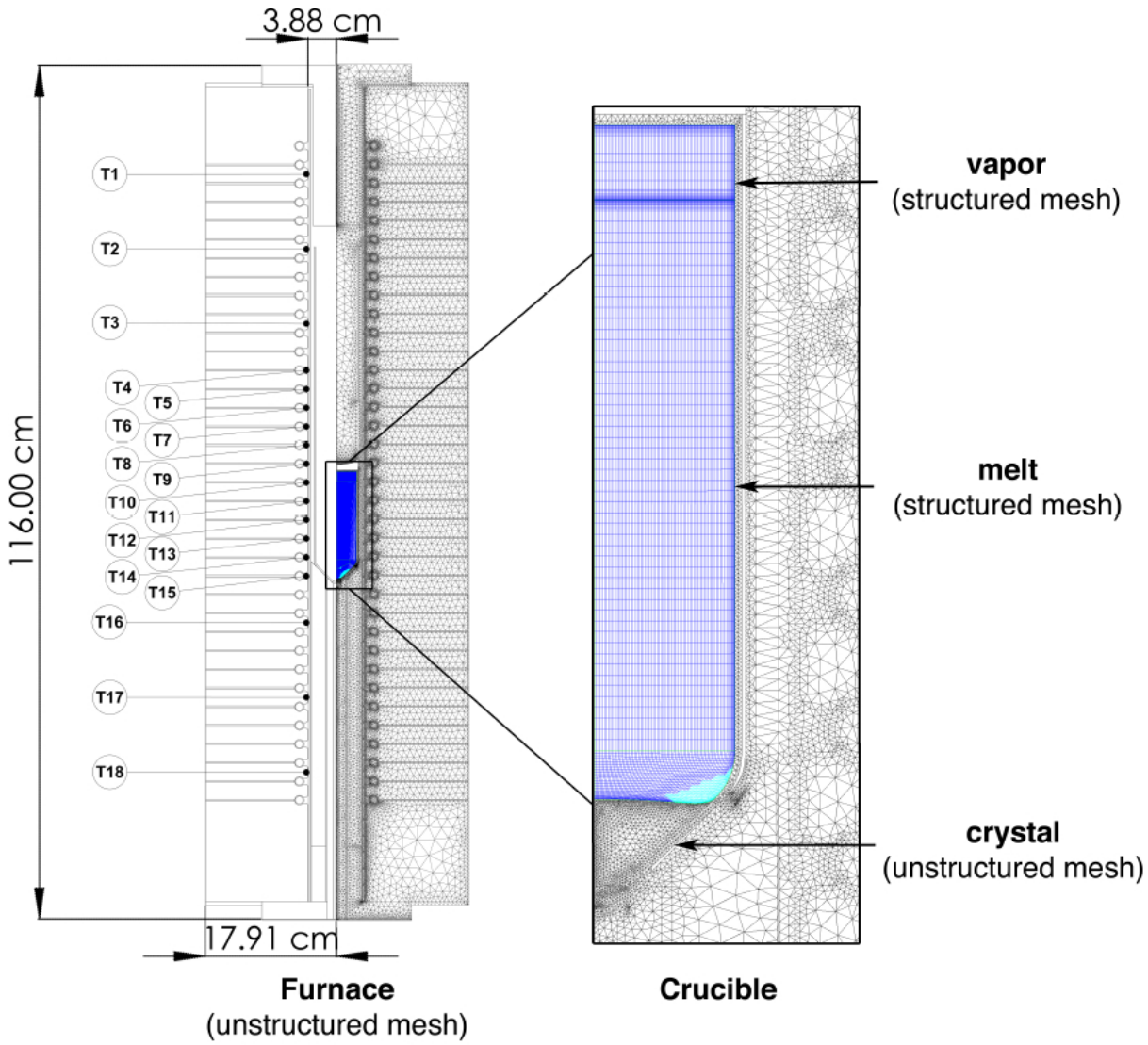

Figure 2.8: A schematic of the two-dimensional VB furnace model, showing the meshed domain employed for simulations on the right of the furnace's axis of symmetry, and the location of temperature set points for heater control on the left.

Chapter 3

Anomalous Segregation of Cadmium Zinc Telluride during Electrodynamic Gradient freeze Growth

3.1 Chapter Summary

A transient, coupled model has been developed to analyze the segregation of zinc in Cadmium Zinc Telluride (CZT) grown in an electrodynamic gradient freeze (EDG) furnace. The coupled model consists of a local model that solves for time-dependent melt flow, heat transfer, melt-crystal interface position, and zinc distribution in both melt and solid phases and a quasi-steady-state global model that features realistic furnace heat transfer. After verification and validation tests, the model is applied to predict composition patterns in a large-scale CZT EDG growth system previously analyzed by Gasperino et al. (JCG 311, 2327–2335, 2009). Surprisingly, anomalous zinc segregation is predicted, featuring a non-monotonic axial concentration profile and several local minima and maxima across the boule. A mechanistic explanation is put forth based on the cumulative effect of changes in multi-cellular melt flow structures, a particularly susceptible occurrence for CZT systems. Additional effects of furnace translation rate and solid state diffusion are probed.

3.2 Introduction

Cadmium Zinc Telluride ($Cd_{1-x}Zn_xTe$ or CZT), alloyed at x=0.10 zinc, has become a significant material for use in radiation detectors [139, 140, 141, 142, 143]. CZT-based devices promise portable, high-resolution gamma radiation detection while operating at room temperature, with superior properties than those of competing technologies. Such detectors could be applied in many fields, such as space research, medical imaging and other industrial applications. However, the most critical application of CZT detectors is to help combat illicit trade of nuclear materials and radioactive sources.

Thus far, however, it has been extremely difficult to produce large-area, single-crystal CZT with low compositional variation and homogeneous electrical properties. In the reviews by Rudolph [144, 145] and Triboulet [146, 147], many challenges to the successful growth of CdTe and CZT have been addressed, such as crystallinity, cracking, dislocations, second-phase particles, and compositional homogeneity. Here, we concentrate on the issue of zinc uniformity during the growth of CZT from the melt. Even though zinc is a substitutional dopant for cadmium, its much lower mass makes it preferentially incorporate into the growing crystal, with a distribution coefficient of approximately $k = 1.35$, thus leading to segregation during growth and non-uniform composition. Zinc uniformity is important for detector-grade material, since it strongly affects electrical resistivity [148].

In general, much is understood about the segregation of a dilute species during melt growth. The two extremes of behavior are represented by classical scenarios of complete mixing in the melt, leading to the Scheil equation [149], and of no mixing at all, the so-called diffusion-limited case analyzed by Smith, Tiller, and Rutter [150]. Both behaviors exhibit monotonic axial concentration distributions that either steadily increase or decrease in the direction of growth, according, respectively, to cases where the distribution coefficient of the segregated species is greater than or less than unity. A more complete picture of segregation emerged, with the appreciation of the effects of interface shape and incomplete mixing on radial segregation, from the careful application of numerical models for convection and solidification; see, e.g., the overviews [77, 151, 152].

Surprisingly, zinc segregation has been a relatively neglected topic in prior theoretical analyses of the growth of CZT, likely because of the significantly greater challenge of performing such analyses compared to more simple studies of heat transfer and solidification. For example, Sen *et al.* [153], Pfeiffer *et al.* [154], and Parfeniuk *et al.* [155], constructed early models for CZT growth but did not consider melt convection, a phenomenon that is

necessary for understanding heat transfer in the melt for these compounds and for solute segregation. Later, more realistic two-dimensional models have been employed to better understand the characteristics of both vertical [156, 157, 158, 159] and horizontal [160, 161, 162] Bridgman techniques for CZT crystal growth. Of these studies, Kuppurao *et al.* [158] analyzed segregation during the vertical Bridgman growth CZT for infrared detectors and found axial zinc profiles similar to those predicted by the Scheil equation; however, they also speculated that previously reported anomalous segregation was possibly caused by solid-state diffusion of zinc from newly grown regions to the initial solid formed during nucleation. Kuppurao *et al.* [159] followed with an analysis of segregation and interface stability during "growth and pause" processing strategies used for CZT growth. In addition, Edwards *et al.* [160] studied Zn segregation during horizontal Bridgman growth of CZT, noting that the extreme interface deflections in these systems actually made composition more uniform in the upper shelf of the grown material. In a later study, Xiao *et al.* [163] considered how ampoule tilt may effect the segregation of zinc in CZT via a three-dimensional, quasi-steady-state analysis. Yeckel and Derby [164, 165] studied the influences of transient flows driven by the accelerated crucible rotation technique (ACRT) on segregation during CZT melt growth in both large- and small-scale vertical Bridgman furnaces. Lun *et al.* [166] found that lateral segregation of zinc could possibly be reduced by ampoule tilting.

Most recently, Gasperino *et al.* [138, 167] applied the CrysMAS code [135, 136] to reveal conditions occurring in electrodynamic gradient freeze (EDG) furnaces during the growth of cadmium zinc telluride crystals. Their analyses focussed on heat transfer, interface shape, and melt convection and considered how crucible design changes might affect growth outcomes. Notably, segregation calculations proved too costly and were not attempted. However, these prior studies are the motivation for the analysis presented here, where we analyze segregation behavior in the same EDG growth system.

Specifically, we describe here how a coupled, multi-scale model has been developed to analyze the zinc segregation during the crystal growth CZT in the system described in [167], an electrodynamic gradient freeze (EDG) furnace with a pyrolytic boron nitride (PBN) crucible employed by co-author Lynn at Washington State University (WSU). This coupled model is numerically verified by comparison with the prior calculations of Gasperino *et al.* [167], and the physical faithfulness of the overall segregation model is validated by comparing with a small-scale, CZT growth experiment.

The model is then applied to study segregation in the large-scale CZT growth system previously analyzed by Gasperino *et al.* [167]. We find surprising results: anomalous, non-

monotonic zinc profiles are predicted for this system, in contrast to classical segregation theory. These profiles are explained via detailed mechanistic interactions among interface shape evolution, melt flow structure changes, and zinc segregation at the interface. Parametric sensitivity analyses are employed to further probe these phenomena.

3.3 Model development

Our prior studies of the EDG growth of CZT [167] employed CrysMAS [135, 136], a model that was able to compute quasi-steady-state (QSS) thermal fields through the entire system (furnace and charge), including flow structure in the melt phase, at reasonable computational costs. However, the QSS approach is not valid for computing segregation in this system, since a steady state is not approached with respect to mass transfer, due to the very slow growth rates in this system. A common justification for QSS segregation analysis is that the diffusion layer through the melt in front of the solidification interface be far smaller than the height of the melt in the ampoule, expressed mathematically as $\mathcal{D}_\ell/V \ll L$, where V is the growth rate, $\mathcal{D}_\ell$ is the diffusion coefficient of the solute in the liquid phase, and L is ampoule length. Using characteristic values of $V \approx 1$ mm/h and $\mathcal{D}_\ell \approx 10^{-4}$ cm^2/s, we find $\mathcal{D}_\ell/V \approx 3.6$ cm, which is comparable to the melt height of 7–15 cm. Thus, a segregation analysis of this system must be transient. Performing a fully time-dependent analysis of the growth process proved to be too computationally expensive using CrysMAS. Thus, we undertook the formulation of the transient coupled model described here.

In the coupled model, we desire to employ our highly developed and computationally efficient finite element code Cats2D [168] to analyze transient segregation in this system, but we also desire to faithfully represent the thermal environment during growth in the WSU EDG furnace. For this task, we employ a one-way coupling between CrysMAS and Cats2D, similar in spirit to the approaches we have employed previously in the QSS calculations of Pandy *et al.* [169] and Lun *et al.* [170].

The general approach is to use CrysMAS to compute heat transfer through the entire system, then apply appropriate temperatures from the CrysMAS results as boundary conditions to Cats2D, as depicted schematically in Figure 3.1. The additional challenge here is to apply these conditions in a rational manner to represent transient growth conditions, as will be outlined below. We note that this one-way coupling approach is still approximate, since it oversimplifies the heat load of the ampoule on the furnace. We have developed a rigorous method for model coupling (see Yeckel, Lun, and Derby [5, 171]), but this ap-

proach is currently limited to steady-state computations thus was not employed for the results presented in this paper.

The global model employs CrysMAS, developed by Müller *et al.* [135, 136] at the Crystal Growth Laboratory of the Fraunhofer Institute IISB, which is capable of modeling crystal growth in high-temperature furnaces with complex geometry in which radiant heat transfer is predominant. CrysMAS employs the finite volume method on unstructured and structured grids with a quasi-Newton iterative solution method.

The local model is solved using Cats2D [168], a finite-element model that computes heat transfer, both conduction and convection, melt flow, solidification position, and solute distribution. Elliptic mesh generation is applied to discretize the domain, with a mixed basis of biquadratic elements with a linear pressure basis. The shape and location of the solid-liquid interface along a prescribed set of element edges is tracked by the deforming mesh method. An implicit trapezoid rule is employed with Newton's method to integrate the transient equations in time.

Here, a common boundary, the outer boundary of the ampoule, is chosen for the global and local model, as depicted in Figure 3.1. Our approach is to perform a QSS computation using CrysMAS for heat transfer throughout the system (including heat transfer, solidification, and melt convection within the crucible), followed by a save of the outer ampoule surface temperatures to a file. This approach is repeated for multiple different configurations corresponding to equally spaced times during the growth process.

To carry out the transient computation in Cats2D, a time-dependent function, $\mathcal{T}_{\mathcal{F}}(z,t)$, is constructed by linearly interpolating between the saved CrysMAS temperature profiles from different growth stages. This function conveys the thermal environment of the furnace during the growth run to Cats2D via a heat flux condition applied along the outer ampoule as,

$$k_i \mathbf{n} \cdot \nabla T = h_c(T(z,t) - \mathcal{T}_{\mathcal{F}}(z,t)), \tag{3.1}$$

where $\mathbf{n}$ denotes a unit vector in a direction normal to the outer ampoule surface, T denotes the temperature of the ampoule, z denotes the spatial position along the outer ampoule wall, t denotes time, and h_c is a coupling constant (effectively a heat transfer coefficient), which is chosen to be large enough so that the difference between the ampoule outer wall and the CrysMAS temperature is very small.

The segregation analysis is then performed via computations of the local model, which comprises the ampoule and its contents of crystal and melt. We consider two-dimensional,

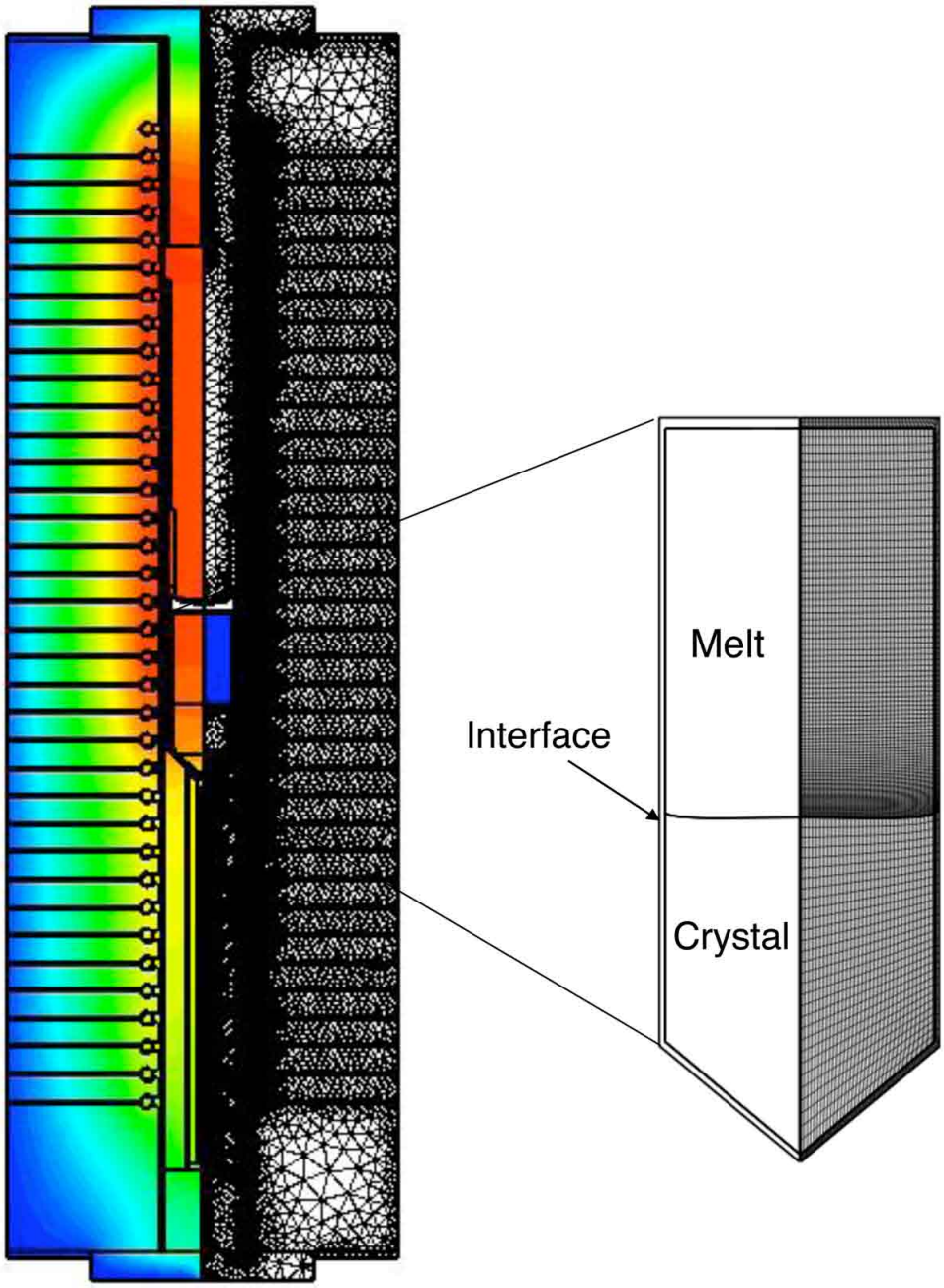

Figure 3.1: Schematic representation of the computational domains and the meshes for the furnace heat transfer (global, CrysMAS) and crystal growth (local, Cats2D) model.

Table 3.1: Physical properties for the furnace simulations of CZT growth

Property [Unit]	Description	Value	Ref.
Thermal conductivity $[W/cm \cdot K]$	CdZnTe crystal	1×10^{-2}	[172]
	CdZnTe melt	2×10^{-2}	[172]
	Cd vapor	8.2×10^{-5}	[173]
	PBN crucible(a)	0.63	[174]
	PBN crucible(c)	0.025	[174]
	Ampoule	0.014	[175]
	SiC support rod	0.62	[175]
	Ampoule support	0.65	[175]
	Furnace liner	6×10^{-2}	[175]
	Mellen insulation	7.7×10^{-3}	[175]
	Stainless steel	0.15	[175]
	Top furnace cap	1.4×10^{-2}	[176]
	Bottom furnace cap	1.8×10^{-3}	[177]
Density $[g/cm^3]$	CdZnTe crystal	5.65	[175]
	CdZnTe melt	5.65	[175]
	Cd vapor	1.97×10^{-3}	[173]
	PBN crucible	2.21	[174]
	Ampoule	2.2	[175]
	SiC support rod	3.1	[175]
	Ampoule support	1.6	[175]
	Furnace liner	3.8	[175]
	Mellen insulation	0.224	[175]
	Stainless steel	8.0	[175]
	Top furnace cap	2.56	[176]
	Bottom furnace cap	0.32	[177]

time-dependent phenomena which arise during growth using equations of continuum transport of heat, mass, and momentum, coupled with physically appropriate boundary and initial conditions. To compute segregation, we assume that zinc acts as a dilute dopant with a constant segregation coefficient of $k = 1.35$ and that stoichiometry is always maintained between the II and VI species. We note that neither solutal effects on melt density nor the effects of non-dilute, multicomponent diffusion are considered. While such effects can be modeled, we have no information about their importance for CZT growth. Please refer to Chapter 2 for a more complete model description and a list of physical properties employed are described in Table 6.1 and Table 3.2.

Table 3.2: Physical properties for the furnace simulations of CZT growth

Property [Unit]	Description	Value	Ref.
Emissivity	CdZnTe crystal	0.7	[175]
	CdZnTe melt	0.7	[175]
	Cd vapor	transparent	
	PBN crucible	0.5	[174]
	Ampoule	0.9	[175]
	SiC support rod	0.9	[175]
	Ampoule support	0.3	[175]
	Furnace liner	0.3	[175]
	Mellen insulation	0.3	[175]
	Stainless steel	0.3	[175]
	Top furnace cap	0.3	[176]
	Bottom furnace cap	0.3	[177]
Heat Capacity$[J/g \cdot K]$	CdZnTe crystal	159.5×10^{-3}	[153]
	CdZnTe melt	187.0×10^{-3}	[153]
	PBN crucible	1192.4×10^{-3}	[178]
Heat of Fusion $[J/g]$	CdZnTe	209	[179]
Melting Temperature $[K]$	CdZnTe	1365	[179]
Thermal Expansivity $[1/K]$	CdZnTe melt	5×10^{-4}	[172]
Kinematic Viscosity $[cm^2/s]$	CdZnTe melt	8.0×10^{-3}	[172]
Diffusion coefficient $[cm^2/s]$	Zn in CdTe melt	1.0×10^{-4}	[180]
	Zn in CdTe solid	5.0×10^{-7}	[181]
Equilibrium segregation coefficient	Zn in CdTe	1.35	[182]

3.4 Model verification and validation

In this section, we present evidence for verification of the coupled model and validation of the overall approach to model segregation. The system is modeled after the PBN ampoule configuration in the EDG furnace identical to the PBN case analyzed in [167]. In these and all subsequent calculations, physical properties for materials used in the model are assumed to be constant with temperature. Parameters that change between computed cases will be explicitly identified in the ensuing discussion.

3.4.1 Verification of coupled model

A series of meshes were constructed and employed to assess the numerical convergence and solution accuracy of both CrysMAS and Cats2D models. The unstructured meshes used in the global model were refined and tested to ensure adequate view factor quality. The structured meshes used within the crucible in the local model were refined and tested until the flow structure and intensity and solute distribution behavior could be assumed to be independent of the mesh.

To verify the effectiveness of the one-way coupling approach, we performed a transient simulation and then compared various measures of the predicted Cats2D solutions at selected times to the corresponding QSS solutions of CrysMAS. Figure 3.2 shows a comparison of the flow and thermal fields predicted at the same point in time by both models. While the results are not perfectly identical, both models exhibit the same convection pattern of three flow cells (streaming clockwise in the middle and counter-clockwise at the top and bottom) and very similar thermal fields. As a qualitative comparison, the Cats2D transient simulation results reproduced all of the flow structures that the QSS computations of CrysMAS predicted for various stages of growth in this system. These multi-cellular flows were discussed at length in [138, 167].

Perhaps the most important aspect of comparison between the two models in Figure 3.2 is the shape and position of the melt-solid interface, since our goal is to compute transient segregation at this interface. Figure 3.3 plots the dimensionless deflection of this interface for both models at numerous times during growth (as represented by dimensionless axial distance along the ampoule axis). Both models agree well with respect to the magnitude and sign (convex versus concave) of the interface deflection, lending confidence that the coupled model is very well representing this system.

3.4.2 Validation with experimental results

The results of the prior section show that the thermal and flow fields and the solidification interface are in good agreement between both model predictions. Hence, we argue that the models are verified, namely that the mathematics and numerical methods are correct. Here we desire to validate the segregation model by comparison with experimental results.

Since segregation results are not available for the system considered by Gasperino *et al.* [167], we consider recent growth runs in the same furnace but employing a smaller ampoule (45 mm inner diameter by 70 mm length). A crystal growth run was carried out by co-author

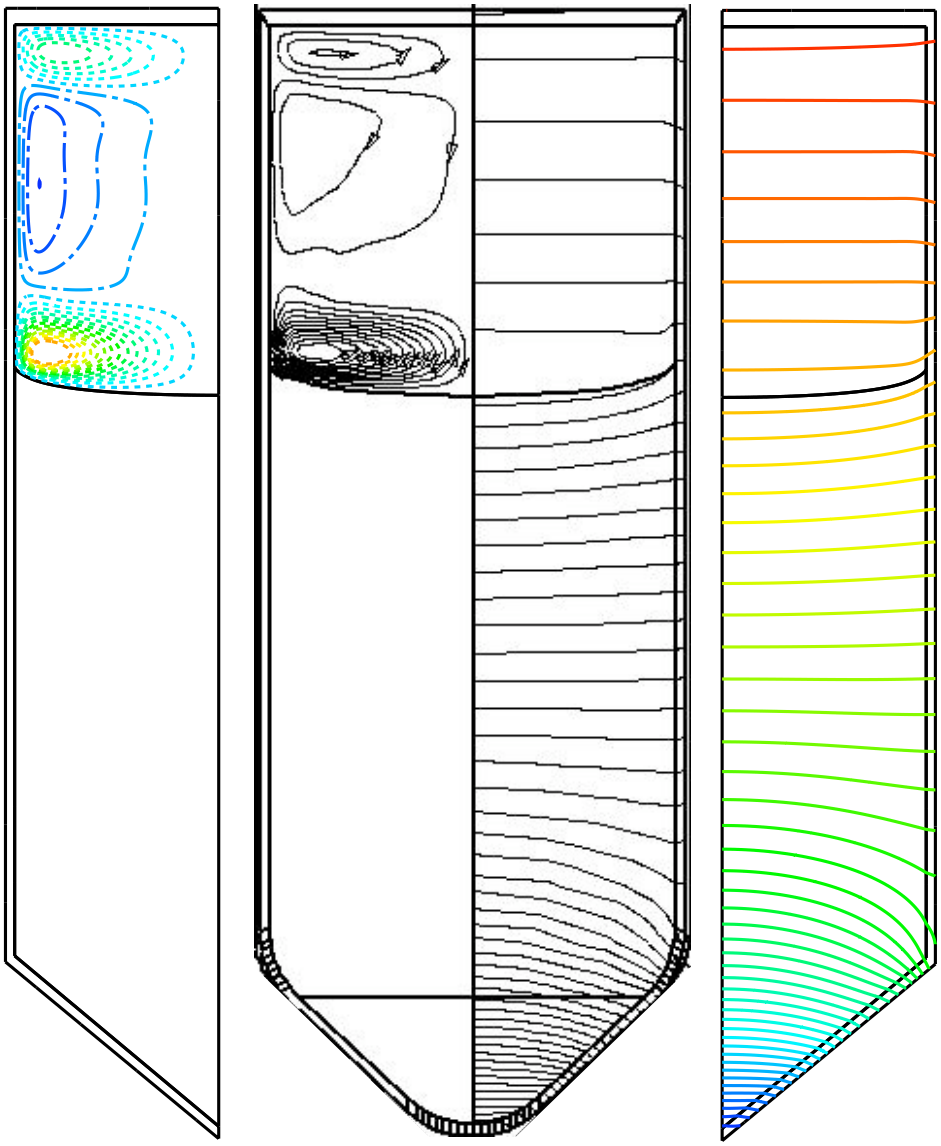

Figure 3.2: Comparison of results between the global furnace model (CrysMAS, in the middle) and coupled, local crystal growth model (Cats2D, on both sides). For global model, the circulation direction of flow cells is indicated by the arrow. For local model, the direction is indicated by the different dash pattern, namely clockwise (- — -) and counter-clockwise (- -).

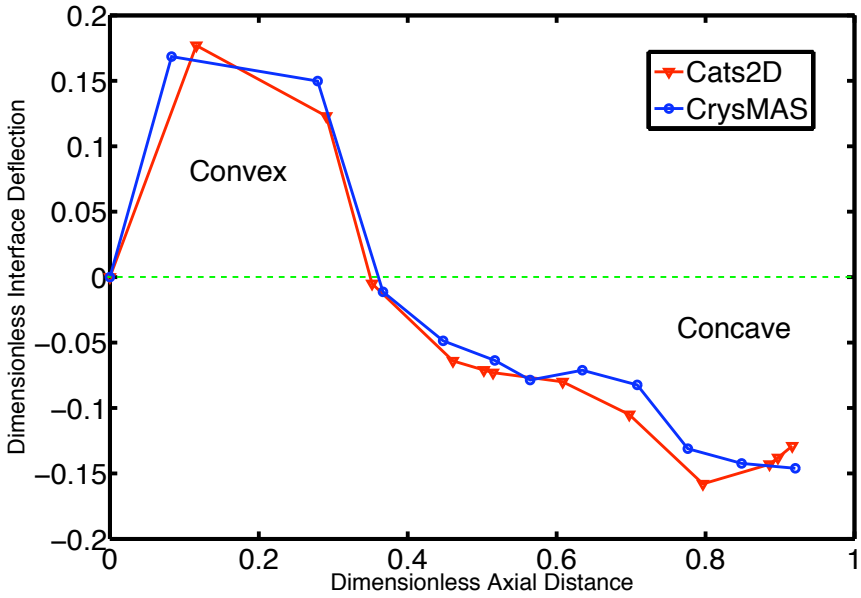

Figure 3.3: Comparison of interface deflection between the global furnace model (CrysMAS) and local crystal growth (Cats2D) model.

Lynn using a nominal furnace translation rate of 0.85 mm/h, a nominal initial composition of $Cd_{0.9}Zn_{0.1}Te$ (with excess tellurium to compensate for cadmium evaporation), and an imposed gradient of approximately 28 K/cm. After growth, an axial cross-section sawed lengthwise through the boule was analyzed by co-authors Cui and Burger at Fisk University using photoluminescence (PL) mapping to reveal zinc composition. The photoluminescence mapping was carried out on a JOBIN-YVON LabRam HR800 system in the backscattering geometry and confocal configuration. The excitation source was a He-Ne laser (632.8 nm, 11 mW) with neutral density filters. A 10X microscopic objective was used to focus the laser beam onto a sample. Typical increment steps of the x–y stage were 0.5 mm. The fraction x in $Cd_{1-x}Zn_xTe$ was calculated based on the formula developed by Hjelt *et al.* [183]. More details of the growth and characterization are planned to be published in the future, along with more extensive modeling comparisons.

We preface our discussion with a statement that our model boundary conditions and geometry are a credible, but imprecise, representation of the experimental growth run. While the ampoule dimensions and shape are similar between model and experiment, we have chosen to apply furnace boundary conditions derived, as discussed above, from the similar (but different) case considered by Gasperino *et al.* [167]. Another uncertainty for our model is the initial condition, which we take in this simulation to be a stationary ampoule containing a small amount of crystallized material in the cone region and with a uniform melt of composition of x=0.1112. The slightly enriched zinc mole fraction in the computation is needed for quantitative agreement with the PL data and is rationalized by the scenario whereby a relative enrichment of zinc in the melt is caused by cadmium evaporation preceding growth.

With these caveats, Figure 3.4 shows the experimental results plotted alongside the model prediction. The color scale of the calculation was chosen to approximately match the PL data plot. Focusing on the first-to-grow solid in the cone region, the model and experimental results both show an axial gradient in zinc that matches reasonably well. Upon growing out of the cone region of the ampoule, there is again reasonably good correspondence between the predicted shape and magnitude of the zinc composition field. The comparison is certainly not exact. This is not surprising, owing to the several idealizations in ampoule shape and the thermal conditions in the cone region. However, both data and model show the same upward bowing of the zinc compositional field in the central part of the crystal. Towards the end of growth, both data and model show a radial flattening of the zinc profile, followed later by an increasingly prominent dip near the ampoule walls (see,

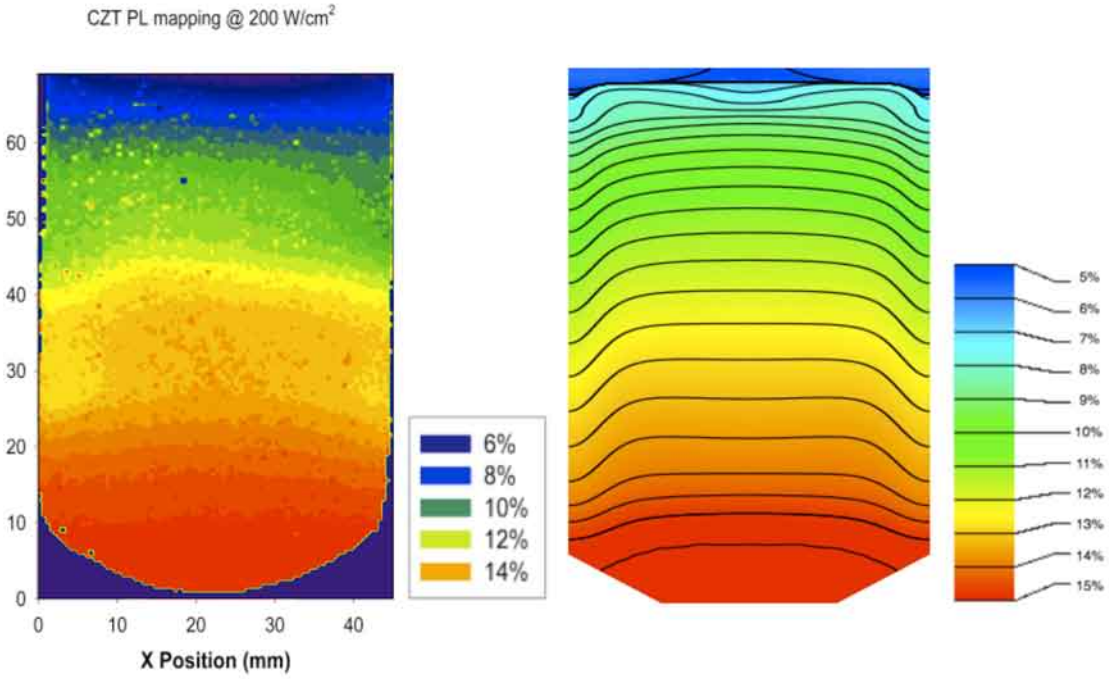

Figure 3.4: Measurement of zinc composition in growth experiment using PL mapping (left) compares well with prediction of zinc composition by the coupled model (right).

e.g., the 10% band of data and the corresponding model predictions).

In a more specific comparison, Figure 3.5 plots the zinc composition along the centerline as a function of axial distance for both model and experiment. The agreement is excellent, except for the last-to-freeze region, between dimensionless distances of 0.95–1. The mismatch in the last-to-grow segment of the boule is caused by our model's assumption of a melt that is enclosed by the end of the ampoule, which differs from an upper melt surface with vapor overhead in the actual system.

Significantly, we have not fitted any parameters of the model to match the growth data, other than the above-described adjustment of the initial condition to account for enriching of the zinc level via cadmium evaporation. We believe that the extent of agreement between this experiment and computation argues convincingly that our segregation model is valid and that its predictions represent physically faithful outcomes.

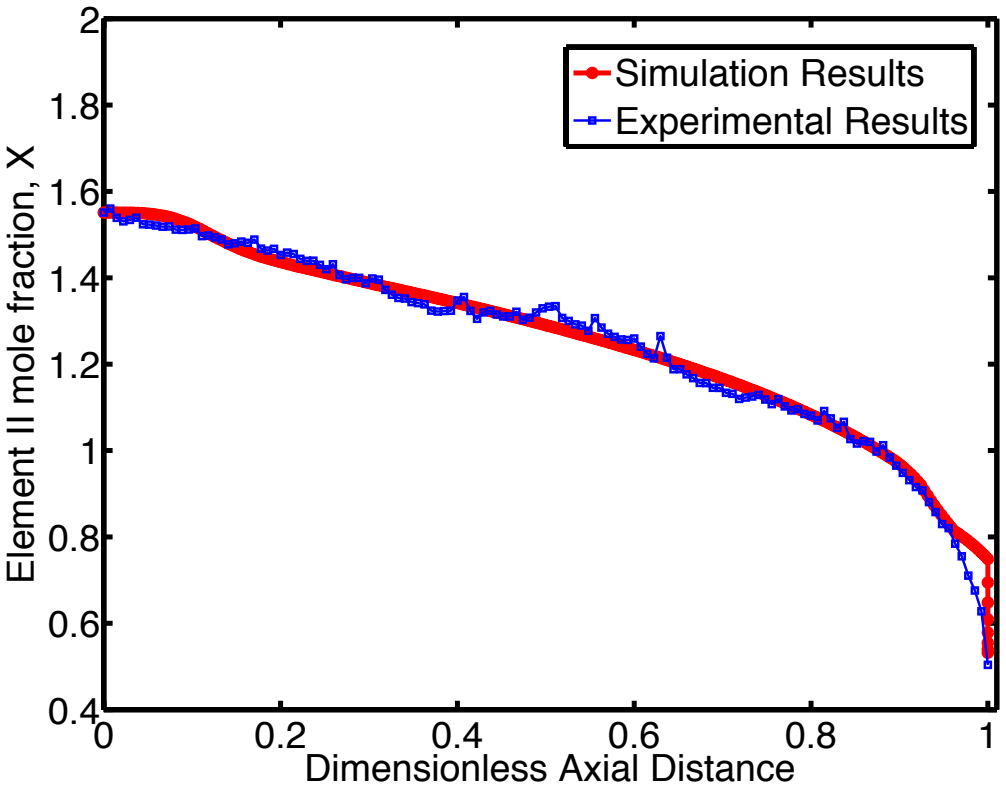

Figure 3.5: Comparison of axial concentration of zinc along the centerline.

3.5 Results and Discussion

We consider nominally two-inch diameter CZT ingots (5.34 cm inner ampoule diameter) grown in a PBN ampoule in the EDG furnace using the conditions employed at Washington State University (see details in [138, 167]). The furnace set-points represented a classical fit of constant hot and cold zone temperatures, bracketing the melting point of 1365 K, connected by a linear temperature segment with a gradient of approximately 20K/cm. This profile was electrodynamically translated at rates on the order of several mm/hr.

Each transient growth simulation with the coupled model starts with a small amount of initially solidified CZT at the bottom of the ampoule and a uniform melt composition. We assume that the initial solid was formed in equilibrium with the melt and has a uniform zinc composition kx_0, where x_0=0.10 is the initial composition of the melt and k=1.35 is the segregation coefficient. The initial temperature and flow fields correspond to those computed with the ampoule at rest and are shown along with the initial distribution of solid and melt in Figure 3.6. At time zero, the external temperature field, $\mathcal{T}_{\mathcal{F}}(z,t)$, is translated upward at a steady rate, which we refer to, somewhat anachronistically and in the context of the vertical Bridgman process, as the pull rate, V_p.

To produce the data needed for $\mathcal{T}_{\mathcal{F}}(z,t)$, 11 quasi-steady-state calculations were performed using a system of approximately 115,000 degrees of freedom in CrysMAS. Solution times for these cases varied from approximately 12 hours to 24 hours on a Dell Precision Workstation outfitted with two Quad Core Intel Xeon Processors running at 2.66 GHz. These computations need only to be performed once to establish the transient furnace profiles for a growth run, thus their cost is amortized over the many ensuing Cats2D calculations.

For most cases, the transient, finite-element computations of Cats2D employed a mesh comprising 65×125 biquadratic elements, shown in the Cats2D inset of Figure 3.1, and a total of 141,656 mathematical unknowns. For this system, an LU decomposition of the Jacobian matrix required approximately 200 seconds on a iMac with an Intel Core 2 Duo 2.8 GHz processor. A variable time step size was used, along with a modified Newton's method, where a single factorization was reused for several time steps, so that the computational time needed for a single transient computation was typically about 3 hours. Accurate computation for the smallest solid-state diffusion coefficient considered here ($\mathcal{D}_s = 5 \times 10^{-8}$ cm^2/s) proved especially challenging. For this case, a mesh of 65×220 elements, comprising a total of 199,436 unknowns, was employed with a maximum time step five times smaller

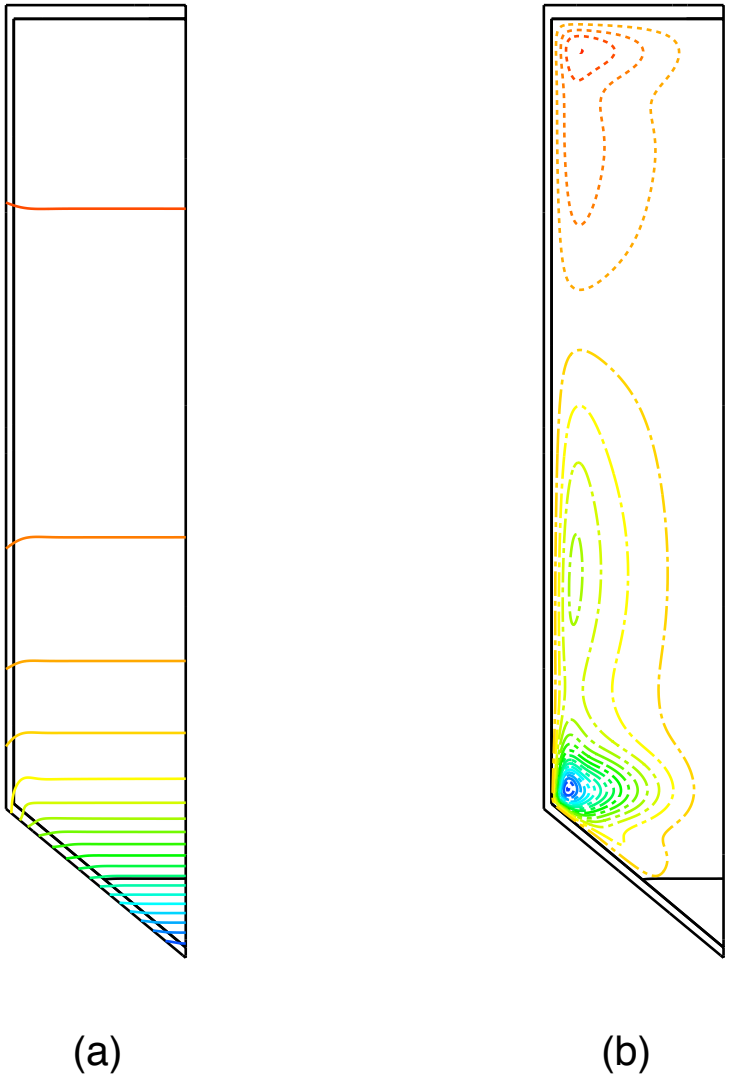

Figure 3.6: Isotherms and streamlines for the system at rest, employed as the initial condition, t = 0. The bold line indicates the melt-crystal interface. (a) $\triangle T = 8K$ (b) $\Psi_{max} = 6.8296 \times 10^{-4}$ (counter-clockwise - -), $\Psi_{min} = -3.2444 \times 10^{-3}$ (clockwise - — -).

than that used for the other cases. This run required over 6 hours for its computation.

3.5.1 Base case

The initial state of the system, which exists while the furnace thermal profile is stationary, $V_p = 0$, is shown in Figure 3.6. A small amount of the crystalline phase is present at the bottom of the crucible. The flow field in the melt consists of two vortices, as indicated by the streamlines plotted in the figure, that are driven by buoyant forces. The lower vortex circulates in the clockwise direction, with warmer fluid rising along the heated wall of the ampoule and descending along the cooler centerline. A weaker flow cell is nested in the upper corner of the crucible and driven in a counter-clockwise motion by thermal end effects. Note that the thermal field through the system shows larger gradients in the lower-conductivity region of crystal and that the initial shape of the melt-crystal interface is ever-so-slightly convex with respect to the melt. While we have not directly assessed the stability of this axisymmetric state, we believe it to be stable to 3D disturbances, based on prior 3D computations of CZT flows in similar Bridgman systems [163, 184].

Immediately after time $t = 0$, a steady furnace profile translation rate of $V_p = 2.67$ mm/h is imposed to initiate growth. Figure 3.7 shows two early stages of growth via a series of plots showing isotherms, melt streamlines, and zinc iso-concentration curves for each growth stage. At a time of $t = 10.1$ hours of growth, shown by Figures 3.7(a)–(c), the interface has grown out of the conical region of the ampoule. The interface shape is convex toward the centerline and concave near the ampoule wall. The reversal of the radial thermal gradient, as signaled by this interface shape, drives two counter-rotating flow vortices adjacent to the interface. The vortex near the wall rotates in the counter-clockwise direction, while the vortex along the centerline rotates in the clockwise direction. Above the cells along the interface, a clockwise vortex fills much of the melt domain. The uppermost flow cell remains nearly unchanged from the initial condition.

The zinc composition at this stage of growth is extremely complicated, as shown in Figure 3.7(c). While the cone region is of nearly uniform composition, an axial transient of decreasing zinc concentration is seen in the crystal just outside of the cone region. In the ensuing solid, there are several, significant rearrangements of the radial zinc composition profile, due to the evolving, multiple-cell flows near the solidification interface. In the melt, the Zn-depleted diffusion layer near the solidification interface is distorted by the flows near the interface. The very strong effect of melt convection is seen by the iso-

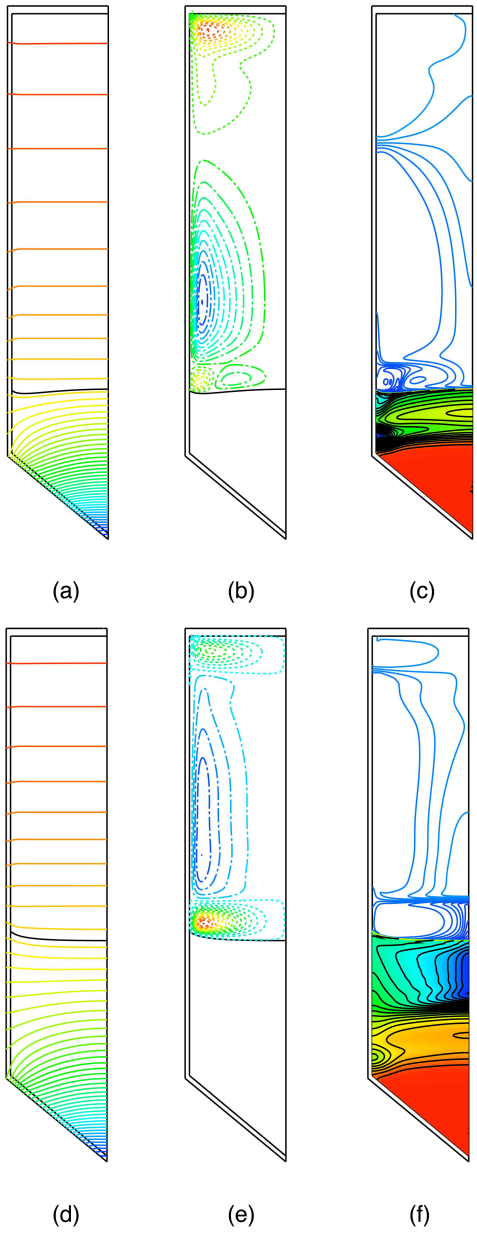

Figure 3.7: Isotherms, streamlines, and iso-concentration curves for the base-case growth run. The bold line indicates the melt-crystal interface. Positive streamfunction values (Ψ) indicate counter-clockwise flows (- -), while negative are clockwise flows (- — -). At $t = 10.1$ h: (a) $\triangle T = 3.7K$ (b) $\Psi_{max} = 4.4267 \times 10^{-4}$, $\Psi_{min} = -5.0624 \times 10^{-4}$, (c) $\triangle x = 0.003562$ in melt, $\triangle x = 0.005981$ in crystal. At $t = 17.16$ h: (d) $\triangle T = 3.7K$ (e) $\Psi_{max} = 8.5659 \times 10^{-4}$, $\Psi_{min} = -2.8511 \times 10^{-4}$, (f) $\triangle x = 0.003485$ in melt, $\triangle x = 0.01276$ in crystal.

concentration contours in the melt that mimic the shape of the streamlines. However, diffusion is important near the solidification interface and also through the shear layers that separate the axially nested flow cells in the melt.

Figures 3.7(d)–(f) show the system state at $t = 17.16$ hours. The interface has evolved to be concave in shape due to latent heat evolution. The local effect of latent heat release on the temperature field creates a single flow cell near the interface that rotates in the counter-clockwise direction, opposite that of the larger vortex above. The upper-most vortex, driven by thermal end effects, has weakened from the prior state. Ignoring the relatively unimportant upper flow cell, the two-vortex state observed here, namely a counter-clockwise vortex along the interface beneath a clockwise vortex in the bulk of the melt, is a classical behavior for most Bridgman systems. Its effects on zinc transport are seen in Figure 3.7(f). Note also that the complicated zinc compositional field in the solid of the prior state has relaxed somewhat due to the effects of solid-state diffusion.

The final stages of growth are shown in Figure 3.8. It is evident that the interface shape and thermal fields do not change appreciably from the prior growth stage (at $t = 17.16$ hours). However, the height of the melt region continues to contract, and its geometry begins to affect the structure of the melt flows. The flow field at $t = 40.2$ hours, shown by Figure 3.8(b), is comparable to the prior state, and the segregation behavior remains very similar, as depicted in Figure 3.8(c). Namely, incomplete mixing near the interface leads to substantial radial segregation of zinc, and there is a continuing and relatively uniform decrease of zinc concentration in the axial direction.

At $t = 50$ hours, shown by Figures 3.8(d)–(f), the melt is confined to a small enough space that the lower and far upper (counter-clockwise) vortices have combined, nearly eliminating the clockwise cell. While the influence of these cells is still apparent on the composition field in the melt, the segregation pattern in the solid remains similar to the prior growth stages. Finally, comparing the composition pattern in the solid in Figure 3.8(f) to those in the prior stages, the smoothing effect of solid-state diffusion can be seen.

3.5.2 Effect of translation rate

A second transient simulation was conducted at a slower furnace profile translation rate of $V_p = 1.335$ mm/h, half of that employed in the base case. All other parameters and properties are identical to the base case, and the same initial condition is applied (see Figure 3.6).

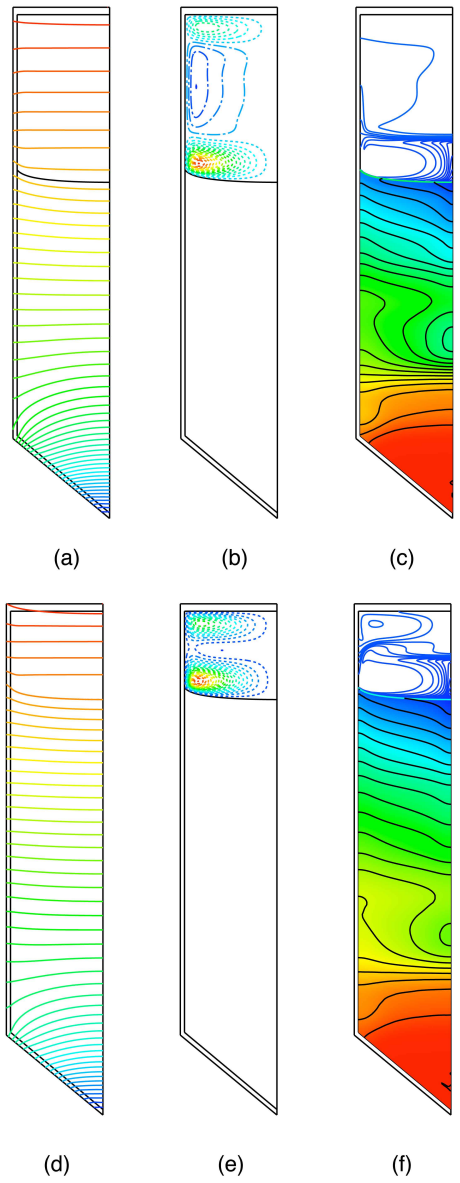

Figure 3.8: Isotherms, streamlines, and iso-concentration curves for the base-case growth run. The bold line indicates the melt-crystal interface. Positive streamfunction values (Ψ) indicate counter-clockwise flows (- -), while negative are clockwise flows (- — -). At $t = 40.2$ h: (a) $\triangle T = 3.7K$ (b) $\Psi_{max} = 1.1887 \times 10^{-3}$, $\Psi_{min} = -2.5811 \times 10^{-4}$, (c) $\triangle x = 0.002988$ in melt, $\triangle x = 0.01874$ in crystal. At $t = 50$ h: (d) $\triangle T = 3.7K$ (e) $\Psi_{max} = 1.1703 \times 10^{-3}$, $\Psi_{min} = -4.0344 \times 10^{-5}$, (f) $\triangle x = 0.002464$ in melt, $\triangle x = 0.02749$ in crystal.

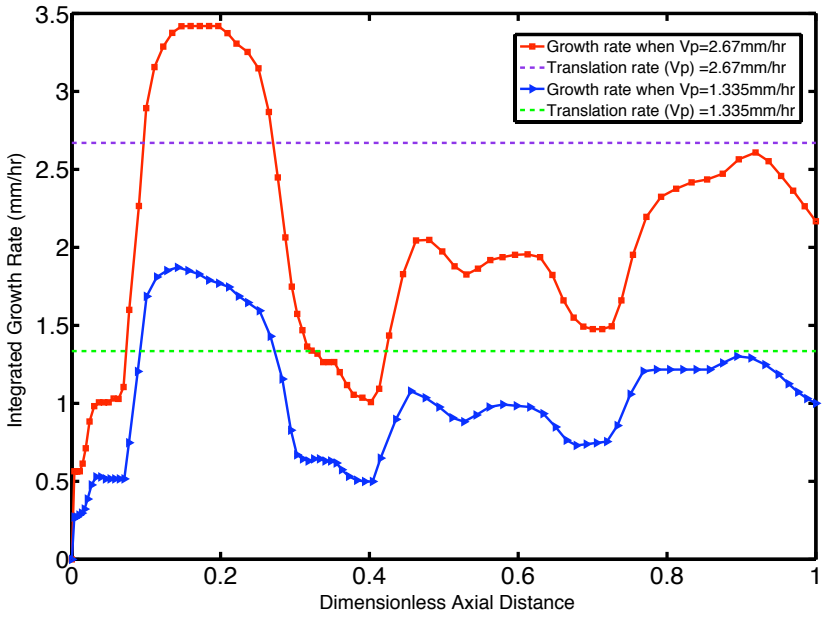

Figure 3.9: Comparison of average growth rates for $V_p = 2.67$ mm/hr and $V_p = 1.335$ mm/hr growth runs.

Figure 3.9 plots the average growth rate over the melt-solid interface as a function of length solidified. Both cases show similar, complicated behaviors. There is an initial transient, with the growth rate overshooting the applied translation rate for both cases, with a maximum occurring near the point where the cone region has enlarged to full radius (at approximately a dimensionless axial distance of 0.15). After, there is a dramatic drop in growth rate to less than half the translation rate, followed by recovery to higher growth rates via another non-monotonic transient. Notably, neither case approaches the ideal of a constant growth rate. Interestingly, long growth transients have been reported in many CZT growth experiments [148, 185]. Finally, a quantitative comparison between the two cases reveals that the slower translation rate results in smaller excursions of the interface velocity, thus achieving slightly more uniform growth conditions.

The applied translation rate also has a noticeable effect on axial segregation in this system, as shown in Figure 3.10, which plots the zinc concentration profiles along the centerline versus the dimensionless axial distance through both solid and melt phases. For comparison, the classical Scheil segregation profile is also plotted against the simulation

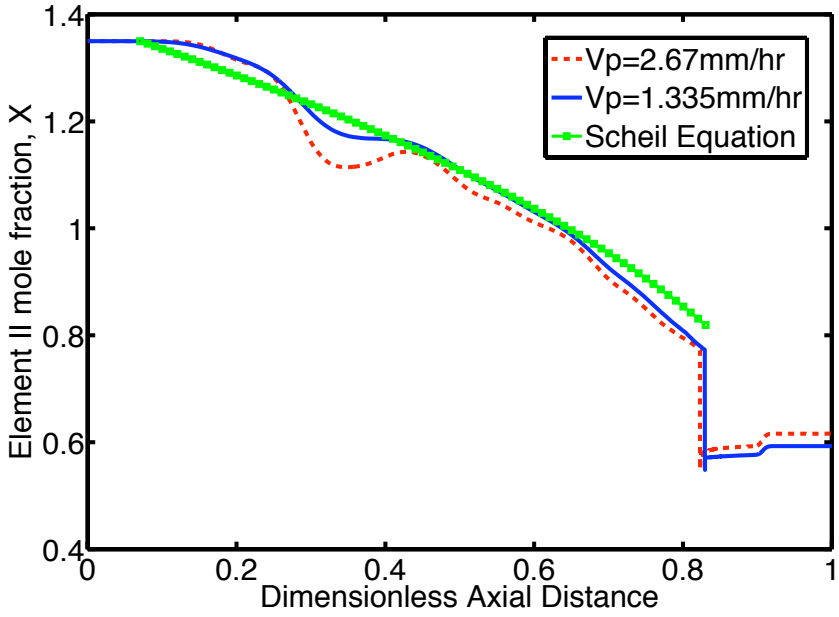

Figure 3.10: Comparison of axial concentration distributions of zinc at the centerline near the end of growth for $V_p = 2.67$ mm/hr, $V_p = 1.335$ mm/hr, and the Scheil profile.

results. While both curves follow the general downward concentration profile of the Scheil curve, both also exhibit notable excursions from the monotonic shape of the Scheil profile. These excursions are smaller for the $V_p = 1.335$ mm/h case compared to the $V_p = 2.67$ mm/h case. Note that faster growth decreases the size of the diffusion layer at the interface (since it scales as $\mathcal{D}_\ell/V$), thus making diffusive transport of the zinc near the solidifying interface more sensitive to disruption via fluid flow and convective transport. This explains why the axial segregation profile deviates more for faster growth than for slower growth.

3.5.3 Effect of solid-state diffusion

All of the above cases were computed using a solid-state diffusivity of $\mathcal{D}_s = 5 \times 10^{-7}$ cm^2/s for zinc, which was assumed to be independent of temperature, composition, and solid-state structure. As was noted in the discussion of the base case, it is evident that solid-state diffusion acts to smooth the zinc composition in the crystal with time. We investigate this effect here by repeating the growth run simulations for the case of $V_p = 2.67$ mm/h but using different values for the zinc solid-state diffusion coefficient. All other parameters are

the same as used for the base case, as is the initial condition.

Iso-concentration contour plots are shown in Figure 3.11 for the system near the final stage of growth for three values of $\mathcal{D}_s$. The middle image, Figure 3.11(b), corresponds to the previous simulations with $\mathcal{D}_s = 5 \times 10^{-7}$ cm^2/s. When an increased value of $\mathcal{D}_s = 5 \times 10^{-6}$ cm^2/s is employed, nearly all of the radial variation of the zinc composition field in the crystal relaxes, leaving a profile that is predominantly axial in nature. A smaller solid-state zinc diffusivity of $\mathcal{D}_s = 5 \times 10^{-8}$ cm^2/s preserves many more of the segregation features in the crystal. In this case, the zinc composition in the crystal exhibits a very complicated pattern, with several local minima and maxima.

The axial zinc composition along the centerline of each of these cases is shown in Figure 3.12. Clearly, the very complicated profile that is present for the $\mathcal{D}_s = 5 \times 10^{-8}$ cm^2/s case is successively smoothed for larger solid-state diffusion coefficients.

3.6 Discussion and conclusions

We have presented results for simulations of heat, momentum and solute transport using a transient, coupled model employing CrysMAS and Cats2D and have focused on the analysis of both axial and radial segregation of zinc during the growth of CZT via the EDG process. This model was mathematically verified by comparison with heat transfer, flow, and interface shape predicted by CrysMAS, and very good agreement was demonstrated. Validation of the model's ability to describe segregation in real systems was provided by comparison of predicted Zn composition with PL mapping of a smaller boule grown in a similar EDG system. While the match was not perfect, the segregation model predicted essential characteristics of the segregation pattern and was deemed to faithfully represent the behavior of the experimental system.

The most surprising and important result obtained in our analysis was the prediction of very complicated, anomalous segregation patterns in zinc composition that would occur in this EDG growth of CZT. To our knowledge, such complicated patterns have not before been predicted for Bridgman-type melt crystal growth systems.

Our first challenge is to explain why such segregation patterns arise in this system. Fortunately, our model results allow us to closely examine the physical mechanisms at play during the growth run. We focus on the simulation that sets the solid-state diffusion coefficient for zinc as $\mathcal{D}_s = 5 \times 10^{-8}$ cm^2/s, since this case more effectively freezes the instantaneous segregation from growth without significant smoothing effects. We plot snapshots

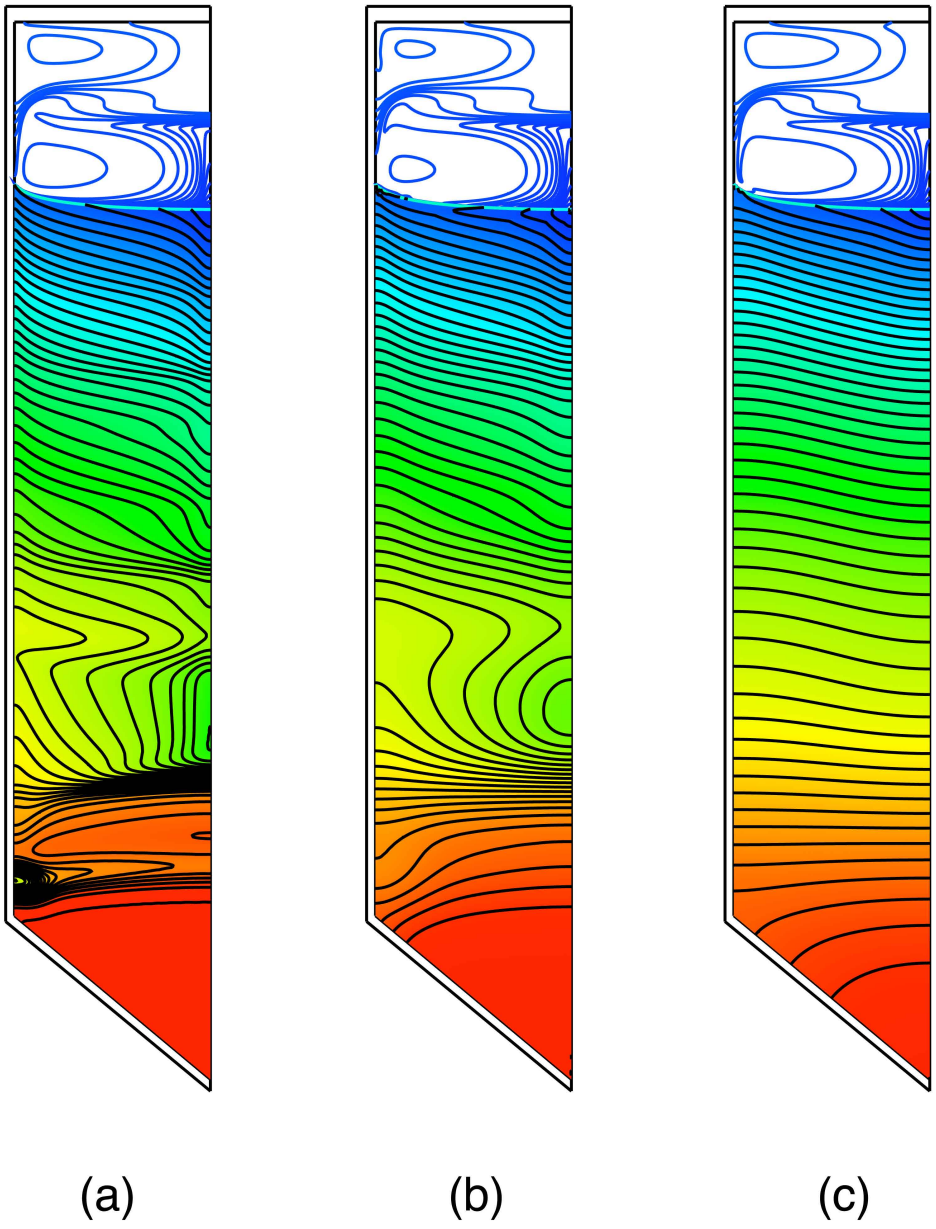

Figure 3.11: Comparison of final-stage concentration distribution for (a) $D = 5\times10^{-8}cm^2/s$, (b) $D = 5 \times 10^{-7}cm^2/s$, and (c) $D = 5 \times 10^{-6}cm^2/s$. Spacing of iso-concentration lines is as follows: (a) $\triangle x = 0.00243$ in melt, $\triangle x = 0.0113$ in crystal; (b) $\triangle x = 0.00244$ in melt, $\triangle x = 0.01132$ in crystal; (c) $\triangle x = 0.00246$ in melt, $\triangle x = 0.01139$ in crystal.

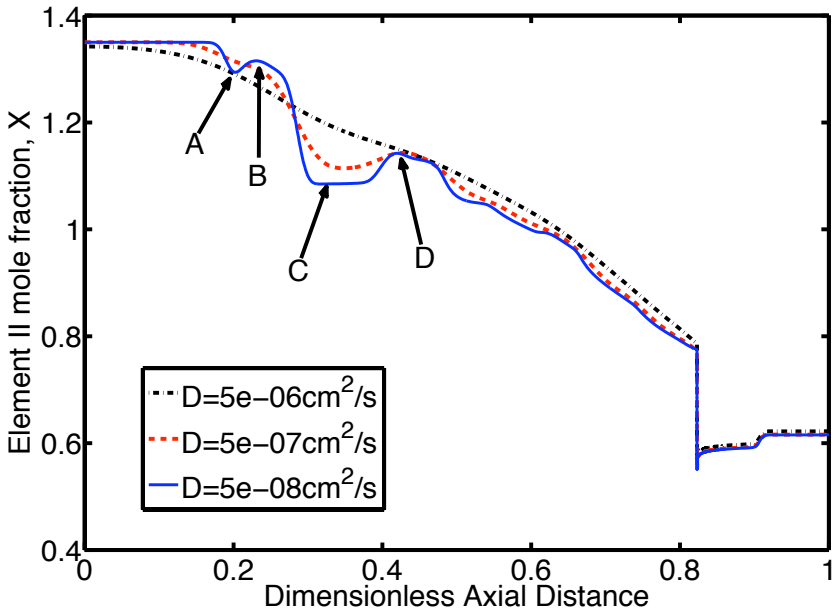

Figure 3.12: Comparison of axial concentration distributions of zinc at the centerline near the end of growth for different solid-state diffusion coefficients. Capital letters indicate states shown in Figure 3.13.

of the system zinc composition and melt flow in Figure 3.13 for the labeled points indicated in Figure 3.12, and we focus on the shape of the Zn axial profile. There is an initial region where the zinc composition is nearly uniform, followed by dip to point A and a rise to point B. We attribute this behavior to the rapid increase and decrease of the effective growth rate, as seen in Figure 3.9, over this period. This change in growth rate affects the size of the diffusion (depletion) layer forming in front of the interface.

From point B to C, there is a sharp decrease in the axial zinc profile. Through these stages of growth, there is a significant rearrangement of the flows near the interface, as was observed previously in Figure 3.7(b) (for the system at time of t=10.1h). Specifically there is the emergence and strengthening of a counter-clockwise vortex nested in the corner formed by the ampoule wall and the melt-solid interface. This new flow cell emerges due to changes in the shape of the interface from convex to concave. By the time the system arrives at point C, the counter-clockwise flow has grown to cover the entire interface. This flow strengthens from C to D, driving a local increase in the axial zinc composition along the centerline. From this point onward during growth, there are no significant structural changes in the flow (until end effects become significant near the very end of the growth run), thus the axial segregation profile is much smoother, although the growth rate variations shown in Figure 3.9 do produce some small oscillations over this time period.

Also extremely significant are the radial variations in zinc composition that arise from the changing flows along the interface as growth proceeds. These radial variations lead to islands of local minima and maxima in the Zn composition of the grown crystal, as shown in Figures 3.13(a) and (b).

After all of this excitement, explaining the behavior of the system with respect to translation rate and magnitude of solid-state diffusion is quite routine. First, growth under a slower furnace profile translation rate allows the system to more easily accommodate changing heat transfer, thus the slower growth velocity results in more uniform growth conditions. With respect to segregation behavior, faster growth decreases the size of the diffusion layer at the interface (since it scales as $\mathcal{D}_\ell/V$), thus making diffusive transport of the zinc near the solidifying interface more sensitive to disruption via fluid flow and convective transport. This explains why the axial segregation profile deviates more for faster growth than for slower growth, as shown in Figure 3.10. The smoothing effect of solid state diffusion becomes apparent when considering that the characteristic diffusion distance over a time t is $L^* = \sqrt{\mathcal{D}_s t}$. If we consider a characteristic time of the growth run of $t \approx 100$ hours and the largest solid-state diffusion coefficient used in the simulations of $\mathcal{D}_s = 5 \times 10^{-6}$

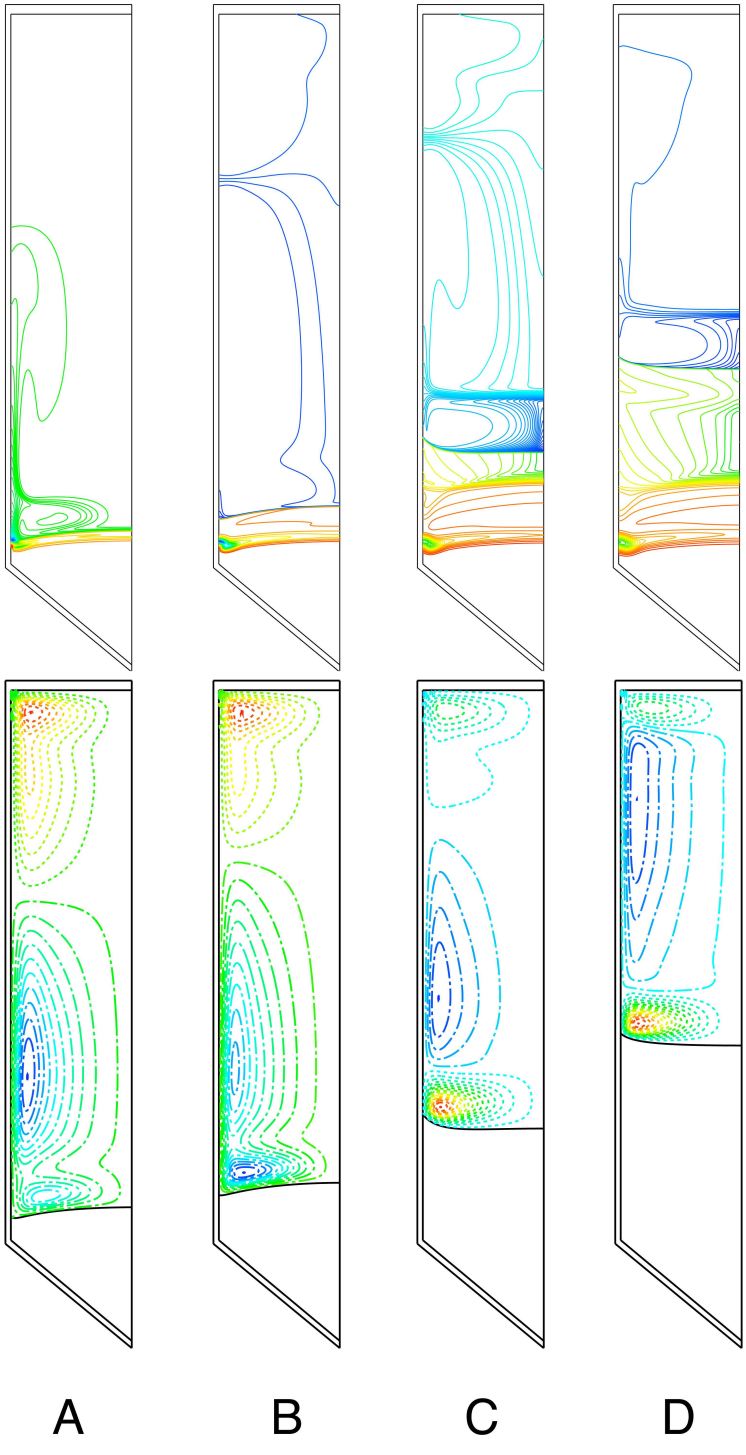

Figure 3.13: States that correspond to the points indicated in Figure 3.12. Above: zinc composition. Below: Flow patterns in the melt, showing clockwise (- — -) and counter-clockwise (- -) vortices.

cm^2/s, we find that $L^* \approx 1.3$ cm, a distance large enough to flatten radial gradients of the composition field but not large enough to substantially alter the axial distribution, namely the result shown in Figure 3.11(c).

Our results have demonstrated, for the first time, the potential for Zn composition fields in melt-grown CZT crystals to be strongly non-uniform. This non-classical segregation behavior arises from the very strong influence of convection on mass transfer in the melt, especially flows near the melt-solid interface. Although the influence of quasi-steady, incomplete mixing near the interface has been long known [77, 151, 152], the effect of time-evolving, multi-cellular flow transitions on producing such complexity of segregation patterns during growth has not been theoretically demonstrated before (other than the effect of high-frequency striations produced by oscillating or turbulent flows [186, 187, 188]). Another important factor at play here is the propensity of CZT flows to rearrange themselves as a function of a changing thermal environment. This behavior arises from the relatively large Prandtl number of 0.4 for this material, indicating that the coupling between flow and heat transfer is one to two orders of magnitude greater than for more typical semiconductors [157, 189].

There is evidence of such complicated compositional patterns in CZT growth experiments. Indeed, anomalous segregation of zinc has been reported in [190, 191, 192], and recent segregation measurements of Babentsov *et al.* [148] also exhibit disconcertedly large zinc compositional variations across their grown crystals. One may speculate that others have avoided publication of similar, adverse results showing Zn non-uniformity in growth. Of course, there are other possible causes of compositional non-uniformity than melt flows, chief among them being grain structures that would strongly affect the local diffusion of zinc through the solid. There are also segregation patterns that are not so complicated, such as that shown in Section 3.4.2 here. The explanation is simple: these simpler, classical compositional patterns arise when there are no significant structural changes to the flow during growth.

The transient computations presented here demonstrate that the melt phase during CZT growth may exhibit multi-cellular flows that change their structure as a delicate function of changing heat transfer conditions. When this occurs, our computations have demonstrated that this mechanism will result in anomalous segregation that leads to very non-uniform zinc composition. We believe that this outcome is a factor contributing to the difficulty in obtaining zinc uniformity in many CZT melt growth processes. A thorough understanding of melt flows and their control will be needed to address this issue, and computational

modeling can provide the necessary tools.

Chapter 4

Maintaining convex interface shapes during electrodynamic gradient freeze growth of cadmium zinc telluride(CZT) using a dynamic, bell-curve furnace profile

4.1 Chapter Summary

A novel, bell-curve furnace temperature profile is presented and predicted to achieve macroscopically convex solid-liquid interface shapes during melt growth of CZT in an EDG furnace. A strategy is also presented to dynamically adapt this furnace profile so that uniform, convex interface shapes are maintained through an entire growth run. This approach represents a significant advance over traditional gradient-freeze profiles, which always yield concave interface shapes, and static heat transfer designs, such as pedestal design, that achieve convex interfaces over only a small portion of the growth run. Importantly, this strategy may be applied to any Bridgman configuration that utilizes multiple, controllable heating zones. Realizing a convex solidification interface via this adaptive bell-curve furnace profile is postulated to result in better crystallinity and higher yields than conventional CZT growth techniques.

4.2 Introduction

Cadmium zinc telluride (CZT) remains a material of great interest for use in room-temperature gamma radiation detectors [193], in spite of tremendous difficulties associated with its melt growth [144, 194, 195, 147]. Improving the quality of CZT will require challenges to established growth techniques, and computational modeling can provide a testbed to evaluate such new ideas. In the study presented here, we employ modeling to assess and design a novel furnace profile that promises improved solid-liquid interface shapes during growth via the electrodynamic gradient freeze (EDG) technique.

Controlling the shape of the solid-liquid interface has long been desired for melt crystal growth processes. In general, an interface shape that is convex with respect to the crystal has been postulated to minimize the potential for defects, such as dislocations, grains, or twins that may arise from deleterious ampoule wall interactions, to propagate toward the bulk crystal [33, 18]. Such defects are particularly acute in the growth of crystalline CZT due to its weak mechanical strength (giving rise to large dislocation densities in grown material) and its propensity to lose its single-crystal character during growth via the generation of new grains [144, 194].

There is experimental evidence to support the contention that convex interface shapes give rise to better quality CZT. For example, heat transfer naturally promotes convex interface shapes during the growth of CdTe and CZT by the traveling heater method (THM), and observations of concave interface shapes in this process have been correlated with the unwanted formation of new grains [196, 197]. Further, in important recent papers, Carcelén et al. [198] and Crocco et al. [199] demonstrated how changes in pedestal heat transfer, that ostensibly promoted a more convex interface shape during the first stages of the vertical Bridgman growth, resulted in a dramatic reduction in the number of grains in the fully grown ingot. The success of this growth strategy illustrates that changes in the heat transfer environment designed to produce convex solid-liquid interface shapes will benefit CZT growth.

The shape of the solid-liquid interface shape is primarily determined by heat transfer in melt crystal growth processes. Early analyses of heat transfer during Bridgman growth [38, 46, 44, 200, 201] clarified many of the factors affecting the shape of the solid-liquid interface, such as the thermal conductivities of the melt, crystal, and ampoule, latent heat generation, and simple furnace characteristics. In particular, Adornato and Brown [39] studied the effect of furnace profiles and ampoule materials on interface shape and favorably

compared their results to experiments of Wang and Witt [48]. Jasinski and Witt [202, 203] provided notable insights on how interface shape may be controlled in Bridgman processes and considered the growth of CdTe as an example system.

Our particular interest is controlling the solid-liquid interface shape during CZT growth, and we have performed several prior studies of this topic [102, 12, 13, 14, 204, 205, 167]. Indeed, these analyses were cited by Carcelén et al. [198] and Crocco et al. [199] as major influences on their growth system design. However, changes in pedestal design and ampoule cone geometry will affect only the initial stages of growth. As indicated by our prior computations [14, 204, 205, 167], the interface reverts to a concave shape in growth beyond the cone region of the ampoule.

Here, we report on a novel approach that promises to achieve convex interface shapes throughout the growth process. Our strategy is inspired by the traveling heater method for CZT, which routinely achieves convex solidification interfaces (see, e.g., [196, 197]), and informed by the astute analysis of Jasinski and Witt [202]. In THM, interface convexity arises from local heating near the interface by the traveling heater. Jasinski and Witt explained that additional heat input near the solidification interface, similar to the effect in THM, should be able to achieve convex interfaces in classical Bridgman systems.

The key idea, then, is to replace classical Bridgman furnace thermal profiles with one that preferentially directs heat into the system near the solidification interface. We call this a "bell-curve" profile, based on the shape of the temperature profile over the melt phase. Calculations presented here show that this new, bell-curve furnace profile can be designed to achieve macroscopically convex CZT solidification interfaces through the entire growth process, as long as the profile can be changed in time, as is possible with multiple-zone Bridgman and EDG furnaces.

4.3 Model approaches

We employ several modeling approaches to carry out the analyses considered here. To assess the viability of achieving a bell-curve profile and its effect on interface shape, we apply CrysMAS, a powerful, finite-volume code developed by the Crystal Growth Laboratory of the Fraunhofer Institute of Integrated Systems and Device Technology (IISB) in Erlangen, Germany [135, 136, 137]. CrysMAS is capable of computing realistic furnace heat transfer, along with thermal, flow, and interfacial phenomena in melt crystal growth systems. We use CrysMAS to perform quasi-steady computations using its inverse mode, where furnace

set point temperatures are specified and the heater powers are solved as unknowns.

To model an entire growth run, we employ Cats2D [206], our in-house, finite-element model that solves for time-dependent melt flow, heat transfer, solid-liquid interface position, and solute segregation in both melt and solid phases. This model has been previously been applied to and validated for the CZT EDG system considered here by Zhang et al. [207]. The ability to perform transient simulations also allows for a model-based approach to designing the bell-curve thermal profile; further details are provided in Section 4.4.2.

4.4 Results and Discussion

Our ideas are developed using a prototypical system that is based on Mellen electrodynamic gradient freeze (EDG) furnace with 18 controlled heating zones (12 one-element zones and six four-element zones) that has been employed by Lynn and co-workers at Washington State University [208]. We consider the growth of CZT in a 2.1-inch inner-diameter, PBN ampoule under a constant translation rate $V_p = 1.335$ mm/hr for all runs simulated in this paper. Figure 4.1 shows a representation of the domains and meshes for the CrysMAS and Cats2D models. Please refer to Chapter 2 for a more complete model description and a list of physical properties employed are described in Table 6.1 and Table 3.2 in Chapter 3.

4.4.1 Quasi-steady, CrysMAS computations

Base case assessment

Figure 4.2 shows the temperature along the outer surface of the PBN ampoule plotted as a function of dimensionless distance along the furnace axis, where $z = 0$ denotes the bottom tip of the ampoule and $z = 1$ corresponds to the ampoule height, L. A "traditional" thermal profile, namely that employed by Lynn and co-workers [208, 204, 138], is shown as a dashed curve, and the "bell-curve" profile that we develop here is shown by the solid curve. The traditional thermal profile is based on two linear segments designed to yield a gradient in the melt of approximately 20 K/cm and a steeper cooling rate in the crystal. Our bell-curve profile employs a similar low-temperature, linear segment but replaces the upper with a curved, parabolic segment that increases to a maximum temperature near the mid-point of the melt and then decreases. A mathematical description of our bell-curve profile is presented in the appendix. Both profiles are translated upward at a constant rate to drive crystal growth; the profiles shown in Figure 4.2 correspond to a point at which

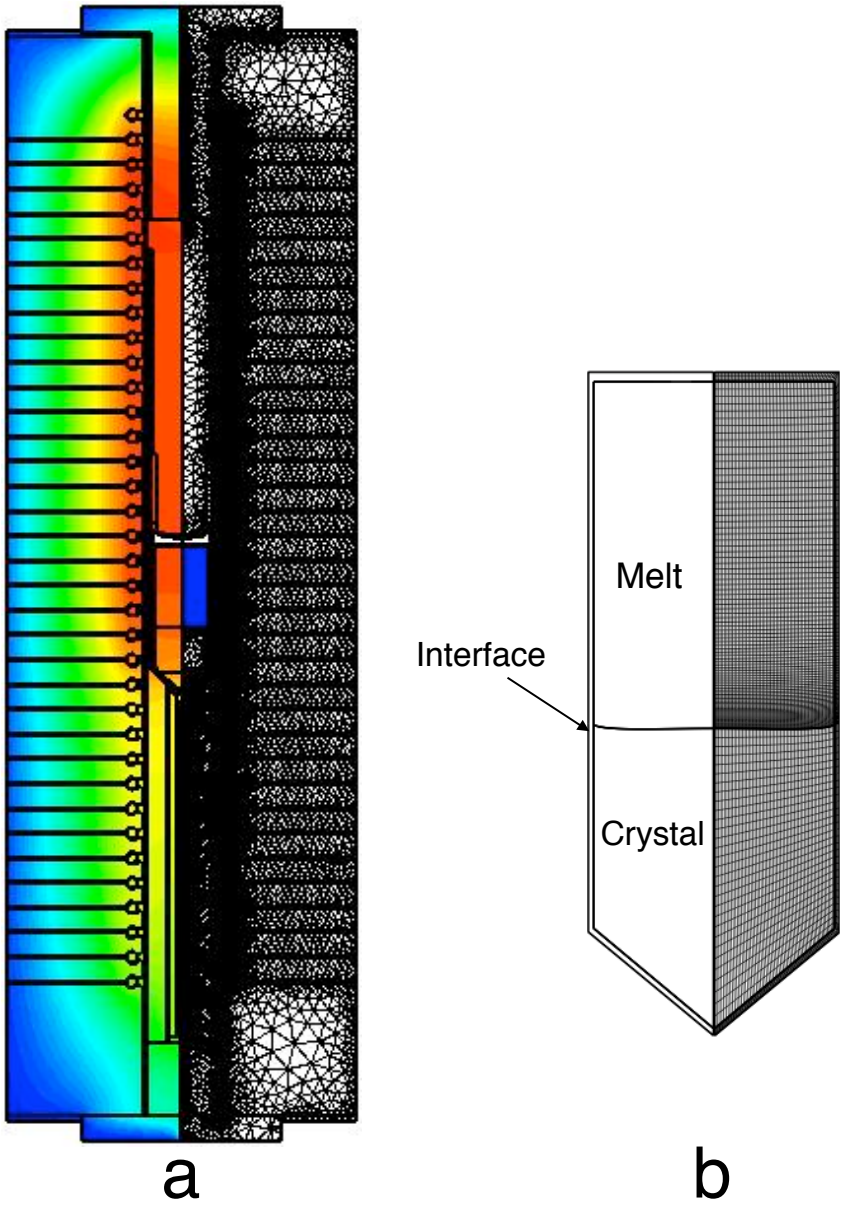

Figure 4.1: Schematic diagrams of the EDG crystal growth models employed in this study. (a) Quasi-steady states of the entire furnace and growth system are computed using CrysMAS. (b) Transient simulations of the ampoule, crystal, and melt are performed using Cats2D with idealized representations of heat exchange with the furnace. More details of both models are provided in the text.

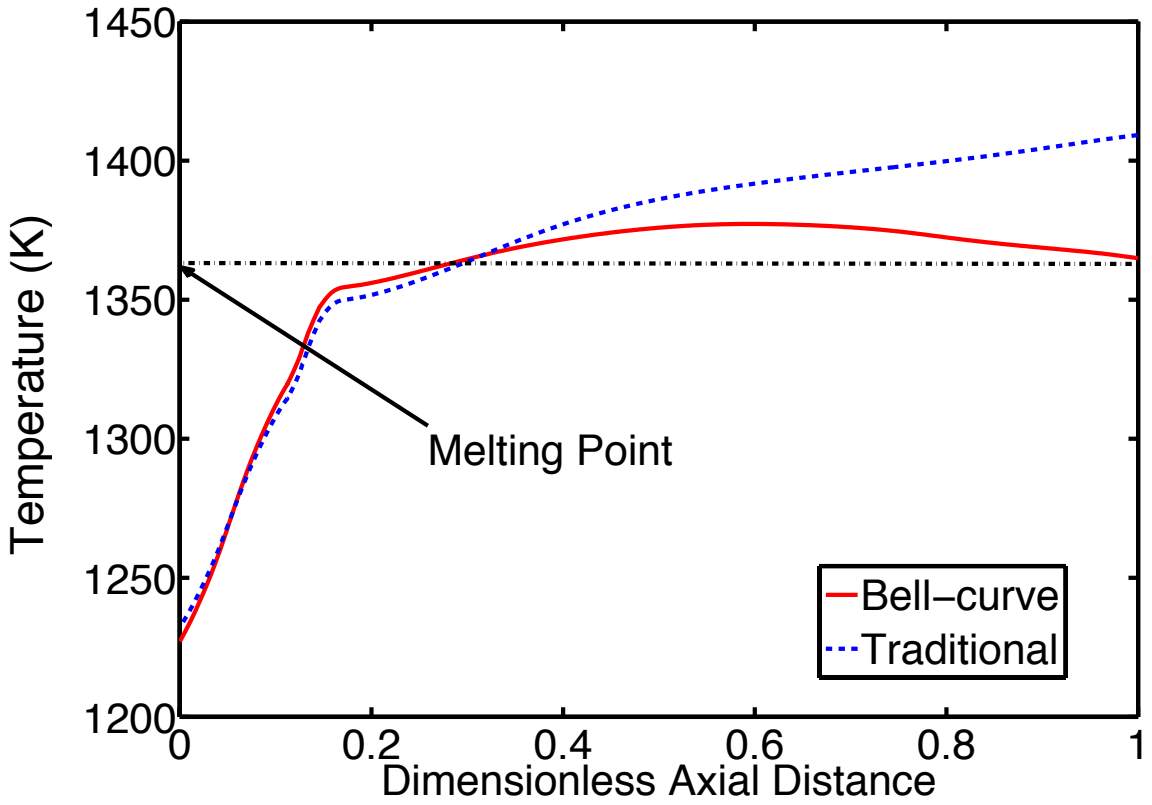

Figure 4.2: Temperature profiles along the outer surface of the ampoule are plotted as functions of dimensionless axial distance for CrysMAS computations using a traditional furnace profile consisting of linear segments and the new, bell-curve profile described in the text.

approximately one quarter of charge has been solidified.

The corresponding base-case, CrysMAS predictions for the quasi-steady thermal field, melt flow structure, and solidification interface shape are presented in Figure 4.3. Figure 4.3(a) shows the case that is typical of nearly all classical Bridgman semiconductor crystal growth systems. The melt temperature decreases in a fairly uniform manner as the interface is approached from above. This is the classical "stabilizing" configuration, where cooler liquid underlies warmer liquid, and, as a result, the flows are relatively weak and do not strongly affect the thermal field, except in the boundary layers near the inner ampoule wall. There are two, toroidal flow cells in the melt driven by thermal buoyant forces. The upper cell circulates in a counter-clockwise sense, with upward flows along the hotter am-

poule wall and downward flows along the centerline. The lower cell rotates in a clockwise direction; the melt is warmer at the centerline, due to the effects of latent heat release at the solidification interface, and flows upward, with a continuity-enforcing downward motion at the inner ampoule wall. Finally, the shape of the solid-liquid interface is concave with respect to the crystal.

In stark contrast, the system under the bell-curve profile, shown in Figure 4.3(b), exhibits dramatically different thermal and melt flow fields and, significantly, a solidification interface shape that is primarily convex with respect to the crystal. Compared to the classical configuration, the isotherms throughout most of the melt are strongly curved by convective transport caused by the flow. Due to the destabilizing axial gradient in the upper portion of the melt, the flow field of this case is approximately an order of magnitude stronger than that of the traditional case and consists of a very large, counter-clockwise cell driven by higher temperatures along the ampoule wall, along with a clockwise cell nested in the upper ampoule corner that is driven by thermal end effects. The interface shape is convex over most of the central region of the crystal and flattens as it approaches the ampoule wall. The changing shape of the interface near the ampoule is caused by the mismatch in thermal conductivities between solid, melt, and ampoule, known as the "interface effect" originally discussed by Jasinski and Witt [202].

Figure 4.4 shows a messy, but enlightening, plot of heat flux vectors, scaled with the local magnitude of heat flow, in the melt domains of the traditional and bell-curve cases. The traditional case of Figure 4.4(a) shows heat entering along the upper surfaces and traveling nearly perfectly downward through most of the melt. Note, however, the significant outward heat flux from the melt along the ampoule wall as the solidification interface is approached. This outward tilt of the flow of heat is consistent with the concave solid-liquid interface shape.

Again, a dramatically different situation is shown in the bell-curve case of Figure 4.4(b). The vectors in the bulk of the melt reflect the heat transfer in the strongly distorted thermal fields shown in Figure 4.3(b). Because of the deceasing thermal profile applied by the bell-curve to the upper melt regions, there are significant outward heat flows along the upper crucible surfaces. In particular, there is a significant inward flux of heat at the ampoule wall above the solid-liquid interface. This heating overcomes the outward flux of the traditional case, redirecting heat flows in a manner that results in a convex interface.

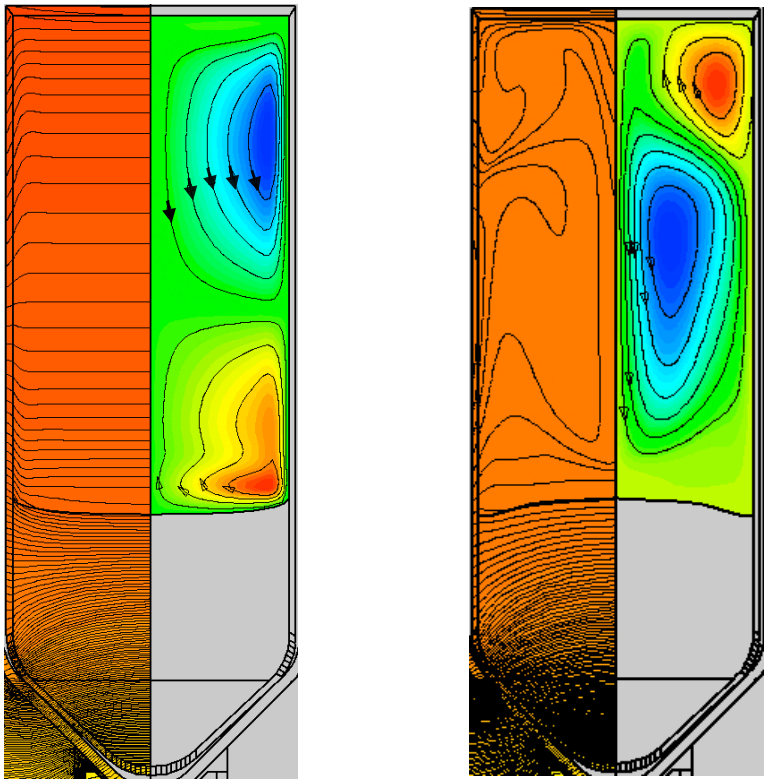

Figure 4.3: Comparison of isotherms (left), melt streamlines (right), and interface shape from quasi-steady CrysMAS simulations of EDG growth of CZT. Isotherm spacing of $\triangle T = 1.5K$ is used for all plots. Streamfunction limits are listed for each case. (a) State obtained with traditional furnace profile: $\Psi_{max} = 2.55 \times 10^{-02} m^2/s$ (clockwise), $\Psi_{min} = -3.36 \times 10^{-02} m^2/s$ (counter-clockwise). (b) State obtained with bell-curve furnace profile: $\Psi_{max} = 2.96 \times 10^{-01} m^2/s$ (clockwise), $\Psi_{min} = -6.74 \times 10^{-01} m^2/s$ (counter-clockwise).

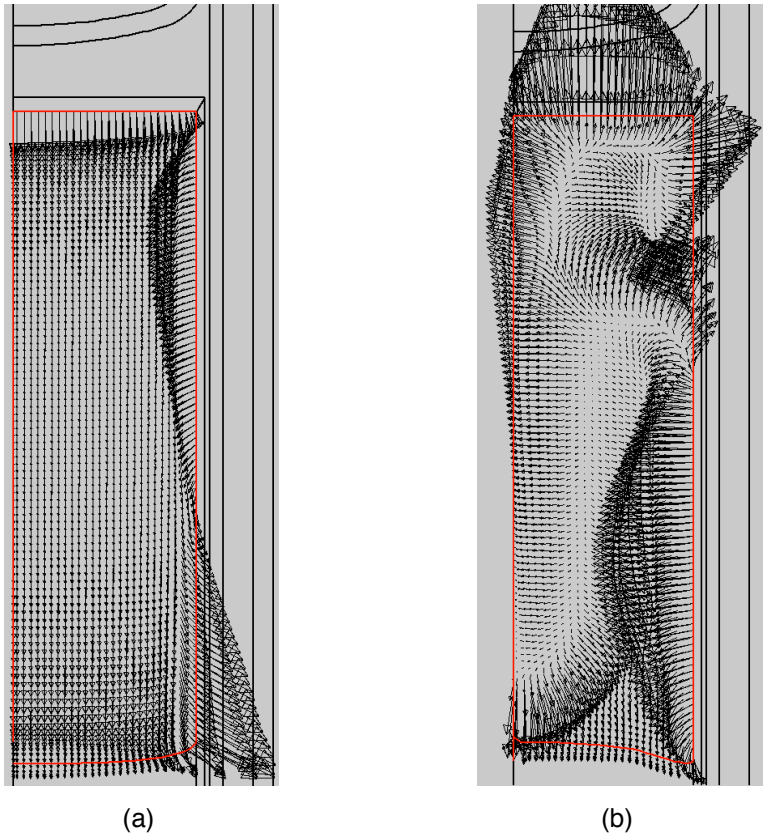

Figure 4.4: Heat fluxes in the melt are indicated by arrows (magnitude is proportional to length) for the simulations of prior figure. The red line outlines the melt domain. (a) State obtained with traditional furnace profile. (b) State obtained with bell-curve furnace profile.

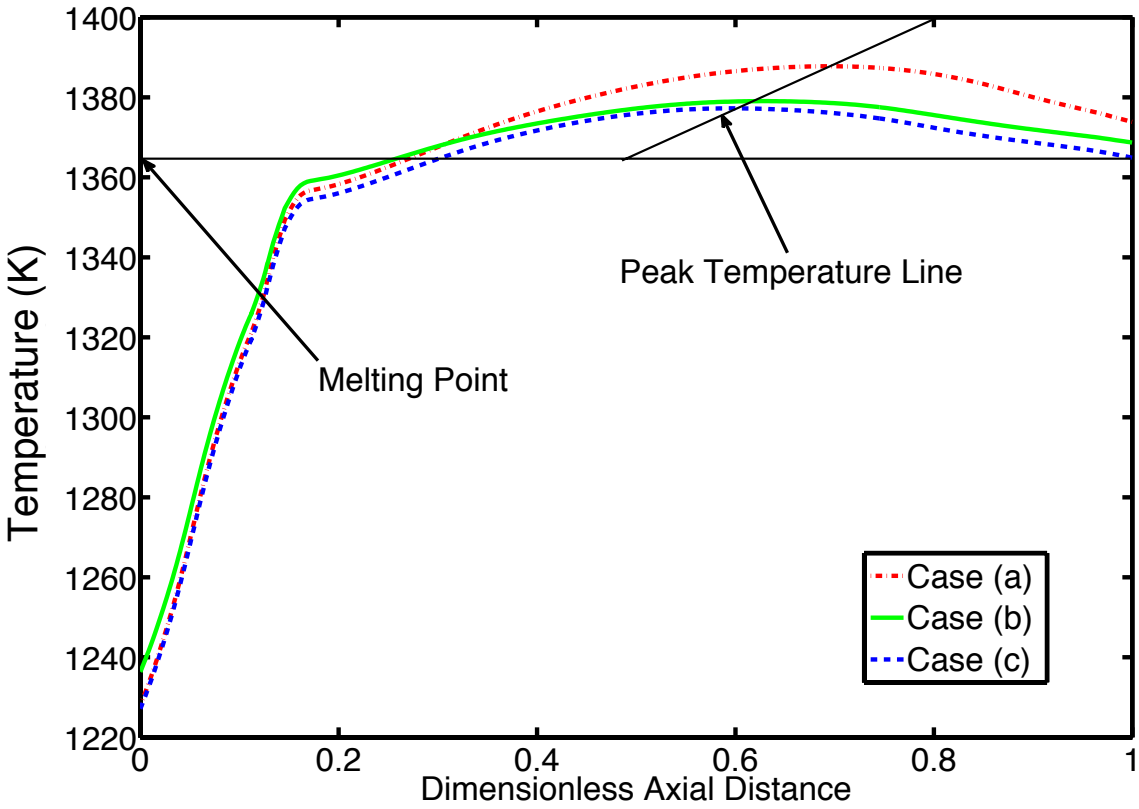

Figure 4.5: Temperature profiles along the outer surface of the ampoule are plotted as functions of dimensionless axial distance for CrysMAS computations using different bell-curve profiles; (a), (b), and (c) correspond to the cases in the following figure.

Bell-curve parameters

There are two parameters that specify the bell-curve profiles we test here, the peak temperature and the axial shift. Several combinations of these parameters were tested via a series of quasi-steady, CrysMAS simulations using profiles shown in Figure 4.5. These profiles were chosen in a directed manner, namely increases in the peak temperature were accompanied by upward axial shifts to keep the furnace profile at the solidification interface approximately constant. We indicate this shift in Figure 4.5 as the peak temperature line.

The crystal growth outcomes, shown in Figure 4.6, indicate the significant sensitivity of the solidification interface shape to these different bell-curve profiles. Figure 4.6(a) shows a system where the temperature peak has been moved upward and increased. For this

profile, the temperature peak is relatively far above the interface, and the axial thermal profile is stabilizing in the lower melt region. As a result, the melt is almost stagnant immediately above the interface, a conduction-dominated temperature field is established, and the solid-liquid interface is nearly flat. As the temperature peak is moved downward, more heat is directed radially inward and closer to the interface as indicated by the states shown in Fig. 4.7(b) and (c), thus rearranging heat fluxes to make the solidification interface macroscopically convex, as indicated by the states shown in Figures 4.6(b) and (c). The sensitivity of this system to even small changes of the bell-curve profile is evident from the noticeable shift in interface shape between cases (b) and (c), even though the corresponding furnace profiles are hardly different, as shown in Figure 4.5.

Furthermore, if we take a closer look at the relationship between the position displacement of the temperature peak along the crucible and the increase of the temperature peak from the melting point, we find a linear relationship as shown in Fig. 4.8. Here we see that the interface will be more concave if the position of temperature peak shifted upward, getting close to the conventional temperature profile. If the position of peak temperature moves downward, the more convex interface will occur. A transition stage exists between the two limits as shown in Fig. 4.8. In the ensuing transient calculations, we choose the position of the peak to be half way between the interface and end of ampoule; see appendix.

4.4.2 Transient, Cats2D computations

The thermal profile in a multi-zone Bridgman or EDG furnace can be changed dynamically, potentially providing interface shape control during an entire growth run. This feature makes such a strategy more compelling than static design changes, such as the pedestal modifications suggested by our prior computations [14, 204, 205, 167] and deployed by Carcelén et al. [198] and Crocco et al. [199], which affect the shape of the solid-liquid interface only during the initial stages of growth. We assess the dynamics associated with the bell-curve profile and interface convexity in the following computations.

Due to the computational expense associated with transient compared to quasi-steady simulations, we turn to our powerful and efficient finite-element code Cats2D for all computations considered here. In these calculations, a flux boundary condition is applied along the outer ampoule surface so that the ampoule exchanges heat with a specified furnace profile, $T_f(z,t)$, as follows,

$$-k(\mathbf{n}\cdot\nabla T) = h(T - T_f(z,t)) + \sigma\epsilon(T^4 - T_f^4(z,t)), \tag{4.1}$$

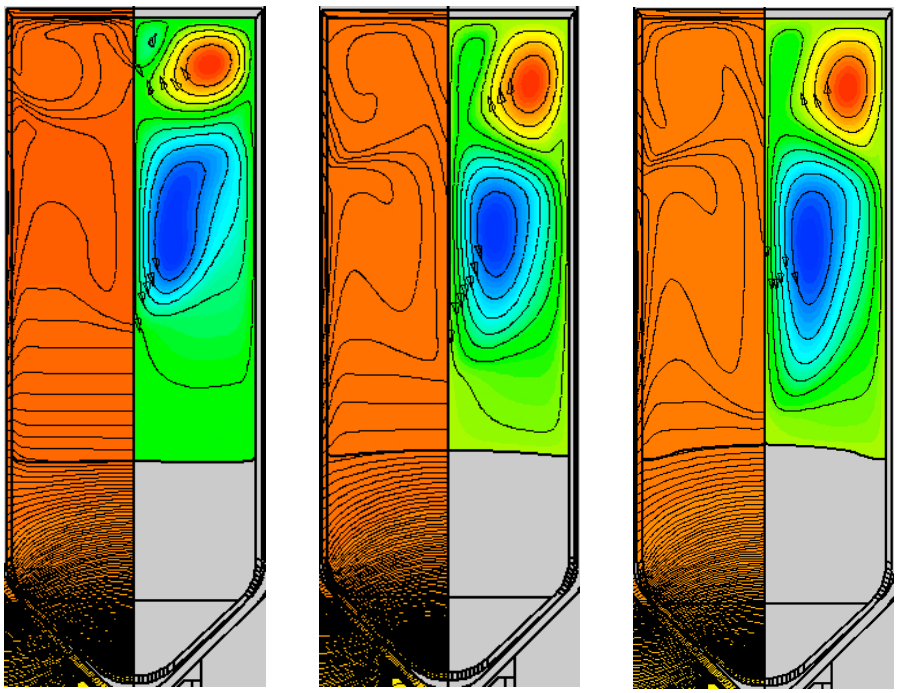

Figure 4.6: Comparison of isotherms (left), melt streamlines (right), and interface shape from quasi-steady CrysMAS simulations of EDG growth of CZT. Cases correspond to the profiles shown in previous figure. Isotherm spacing of $\triangle T = 1.5K$ is used for all plots. Streamfunction limits are: (a) $\Psi_{max} = 4.13 \times 10^{-01} m^2/s$ (clockwise), $\Psi_{min} = -4.43 \times 10^{-01} m^2/s$ (counter-clockwise). (b) $\Psi_{max} = 3.02 \times 10^{-01} m^2/s$ (clockwise), $\Psi_{min} = -6.06 \times 10^{-01} m^2/s$ (counter-clockwise). (c) $\Psi_{max} = 2.96 \times 10^{-01} m^2/s$ (clockwise), $\Psi_{min} = -6.74 \times 10^{-01} m^2/s$ (counter-clockwise).

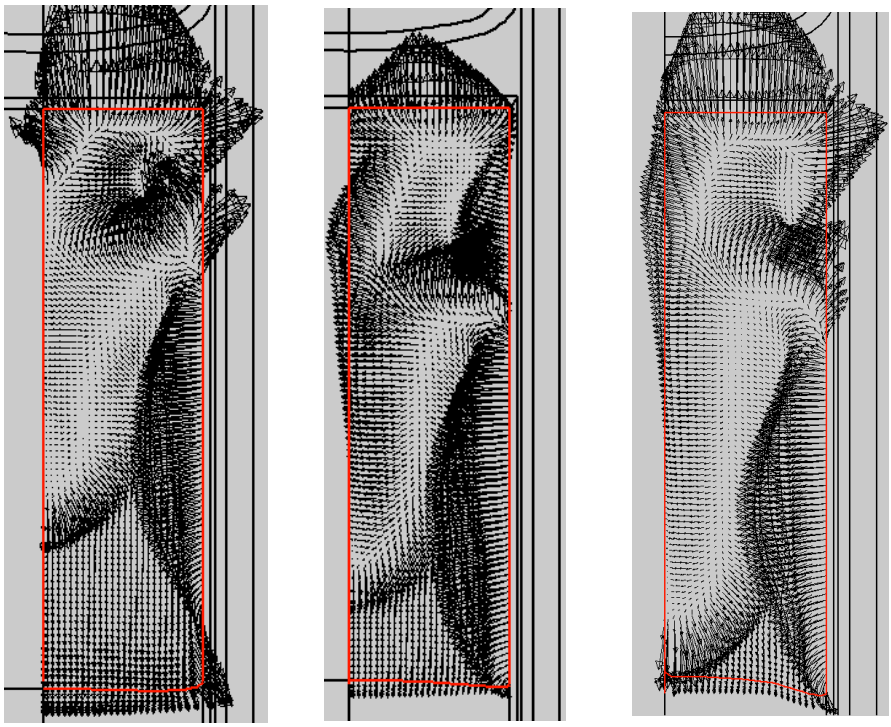

Figure 4.7: Comparison of heat flux from quasi-steady-state simulations of the PNNL furnace using PBN crucible among case (a)-(c). The red line indicates the boundary of melt phase.

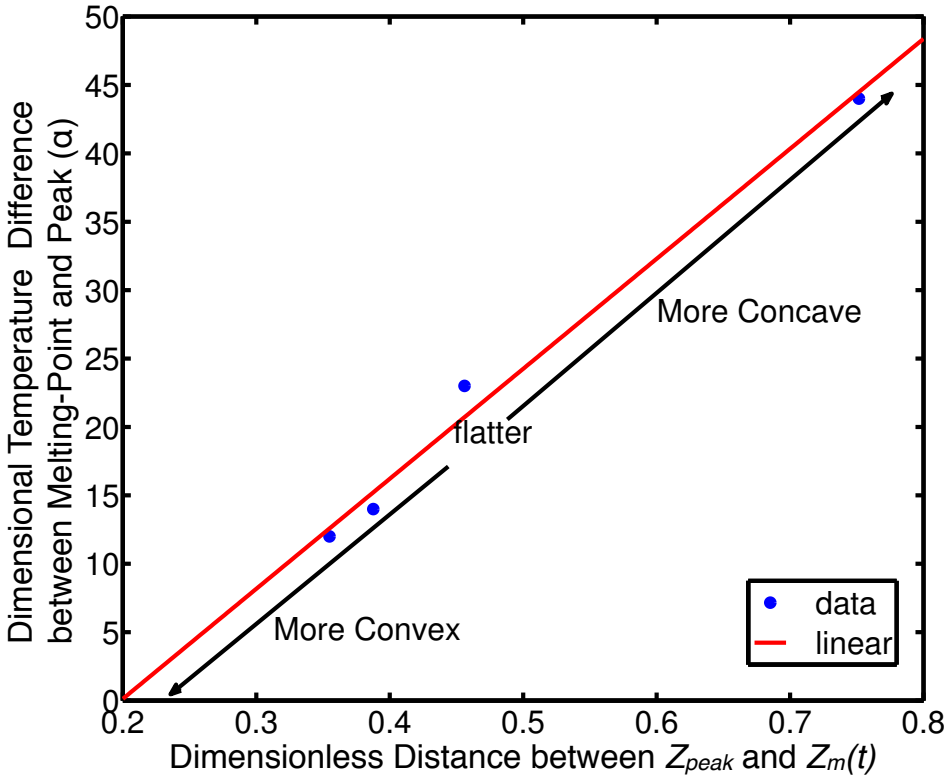

Figure 4.8: Relations between interface shape and potential control parameters

where k is the thermal conductivity of the ampoule, $\mathbf{n}$ is a unit vector pointing outward from and normal to the ampoule surface, T is the absolute temperature of the ampoule surface, h is a Newtonian heat transfer coefficient of convective cooling, σ is the Stefan–Boltzmann constant, and ϵ is the emissivity of the ampoule surface.

The furnace profile, $T_f(z,t)$, is constructed in a prescribed manner: Below the melting point, we assume a linear segment that connects a cold temperature at a fixed location corresponding to the ampoule tip, T_c, with the melting-point temperature, T_m, which is set at a moving axial position $z_m(t)$. To this linear piece, we connect a parabolic segment (the bell-curve) that heats the melt. The parabolic profile is constructed to attain a peak temperature, T_m+a, at an axial distance midway between $z_m(t)$ and the end of the ampoule. A gradient-freeze growth run is simulated by moving the melting-temperature point $z_m(t)$ with time at a constant speed corresponding to the translation rate, V_p. A mathematical representation of $T_f(z,t)$ is presented in the appendix.

Constant bell-curve profile

Our first case considers the application of the furnace profile series depicted in Figure 4.9(a). Here, we set the peak temperature of the bell-curve at $T_m + a_0$ to achieve an initial solid-liquid interface shape that is markedly convex, with an interface deflection of $b \equiv H(0) - H(1) = 0.3$, where $H(0)$ and $H(1)$ are the dimensionless heights of the solid-liquid interface at the centerline and inner ampoule wall, respectively, and scaled with the ampoule inner radius R. Growth is then simulated by simply moving the melting-point temperature, $z_m(t)$, at the translation velocity, V_p, while keeping the peak temperature constant.

The outcome of this strategy is shown in the upper series of plots in Figure 4.10 by the temperature fields and solidification interfaces at various times during growth. Early during the growth run (see A1), the interface shape remains convex. However, the interface begins to flatten as growth proceeds. After 26.8 hours of growth (see A2), the interface is only very slightly convex, and by 42.2 hours it has reverted to the classical concave shape (see A3). Onward to the end of the growth run, the interface shape remains concave.

Adaptive bell-curve profile

Clearly, based on the results presented in the previous section, the bell-curve furnace profile must somehow be adjusted during growth to maintain a convex solidification interface. We

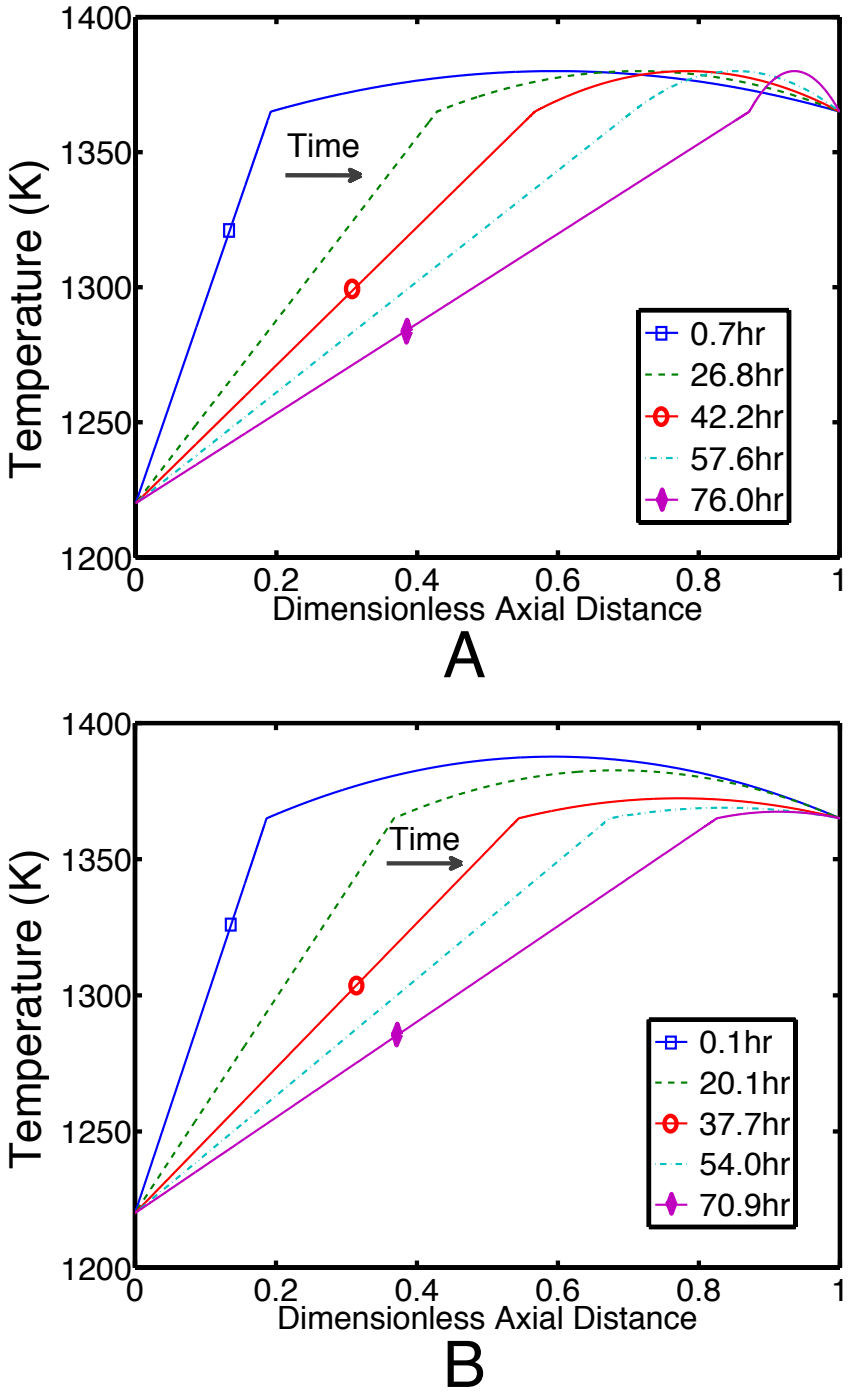

Figure 4.9: Temperature profiles used in the transient, Cats2D simulations, shown at various growth times. A: Bell-curve temperature profile with constant peak temperature. B: Bell-curve temperature profile with variable peak temperature that is changed dynamically to keep the interface shape with a constant, convex deflection. The mathematical form of these profiles is detailed in appendix.

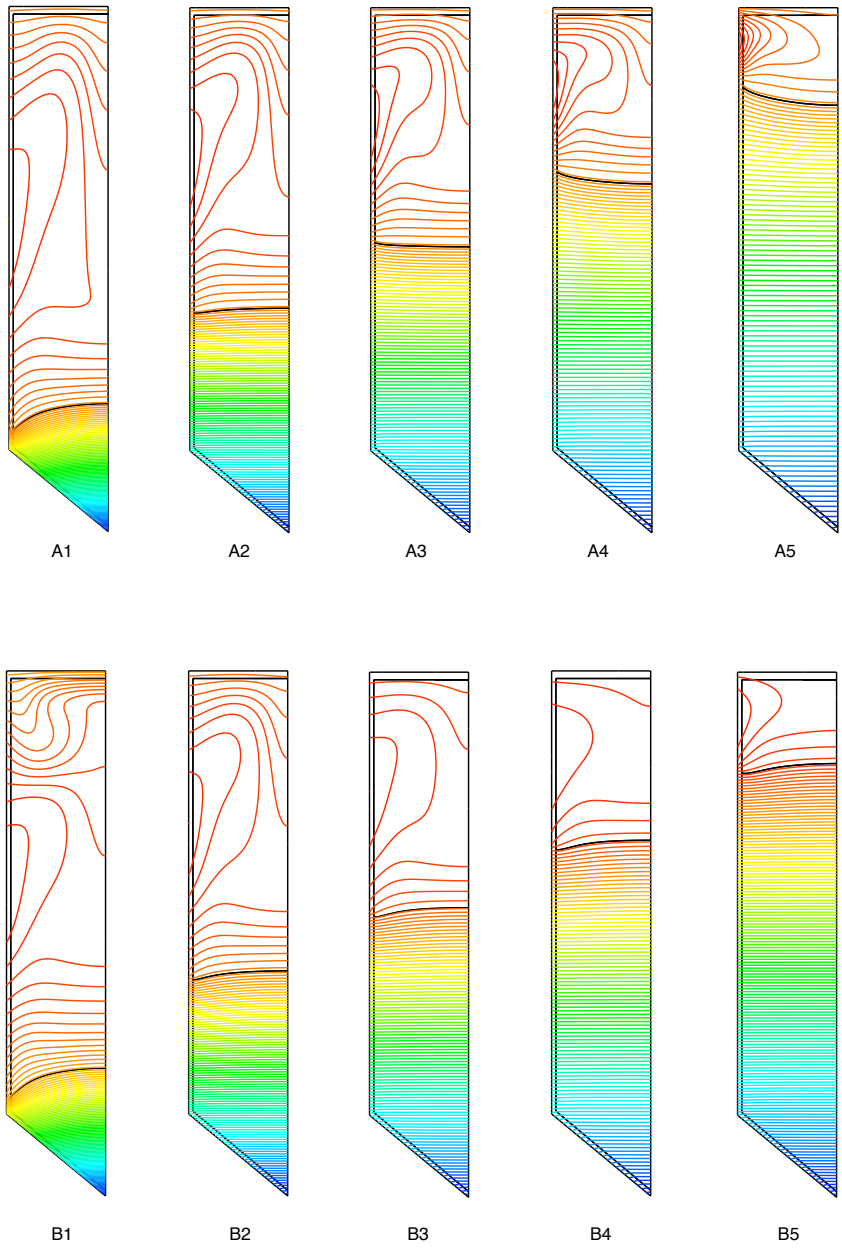

Figure 4.10: The thermal field and interface shapes predicted by a transient simulation using Cats2D are shown at various times corresponding to the furnace profiles of the prior figure. Above: States A1–A5 are achieved with the constant peak temperature profile. Below: States B1–B5 are achieved with the adaptive profile, where the constant peak temperature is determined dynamically.

adopt the following strategy, where we introduce a "control equation" to dynamically adapt the peak temperature as follows,

$$\frac{da}{dt} = g_p \frac{db}{dt} + g_i(b - b_{set}), \tag{4.2}$$

where $a(t)$ is the now time-dependent portion of the peak temperature, $T_m + a(t)$, and b is the interface deflection defined above. The parameters g_p and g_i correspond to proportional and integral gains, respectively, and b_{set} is the desired set point for interface deflection. We emphasize that our intent here is not to simulate a real control strategy; indeed, this approach would be impossible without a means to actually measure the interface deflection during growth. Rather, we use the control construct embodied by eq. (4.2) to compute the dynamically changing bell-curve needed to attain our objective of a convex interface with a prescribed deflection.

Figure 4.9(b) shows the adaptive furnace profile computed using eq. (4.2), with gain parameters set to $g_p = g_i = 1$ and a set point interface deflection of $b_{set} = 0.1$. The initial condition a_0 corresponds to the peak temperature employed for the transient simulation described in the previous section, where the initial interface shape is more convex, with $b = 0.3$ at $t = 0$. The lower series of plots in Figure 4.10 show the temperature field and solidification interface at various times during growth for this adaptive strategy. The initial deflection of the interface is larger than the value prescribed by the set point, so state B1 (at 0.09 hours) exhibits a convex interface with a deflection of $b \approx 0.3$. However, the bell-curve profile is subsequently adjusted so that the desired deflection of $b = 0.1$ is attained quickly. Notably, this interface shape is maintained throughout the remainder of the entire growth run.

The time dependent change of the actual interface deflection, b, and the peak temperature parameter, $a(t)$, of the adaptive bell-curve profile are shown in Figure 4.11. Notice that, after a short initial transient, the interface shape is maintained very near to the desired set point deflection of $b_{set} = 0.1$. After the initial transient, the peak temperature parameter decreases steadily until a mild increase near the end of the run. The decreasing peak temperature coincides with decreasing melt height and volume as growth occurs.

Figure 4.12 shows the axial segregation along the centerline, which agrees very well with the Scheil equation. Due to the convex interface shape during crystal growth, the iso-concentration lines in the crystal also demonstrate the similar shape presented in Figure 4.13. The significance is that the composition field is no longer "anomalous" as predicted

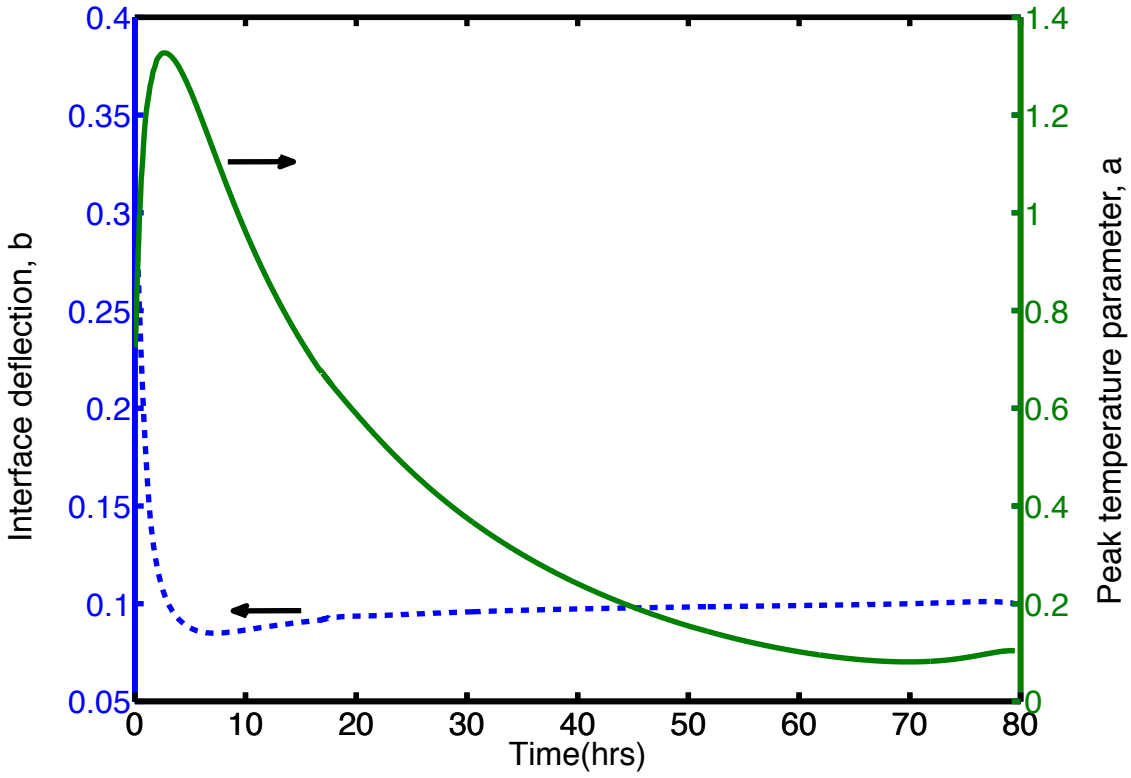

Figure 4.11: The interface deflection, b, and peak temperature parameter a, are plotted as functions of time for the adaptive bell-curve simulation.

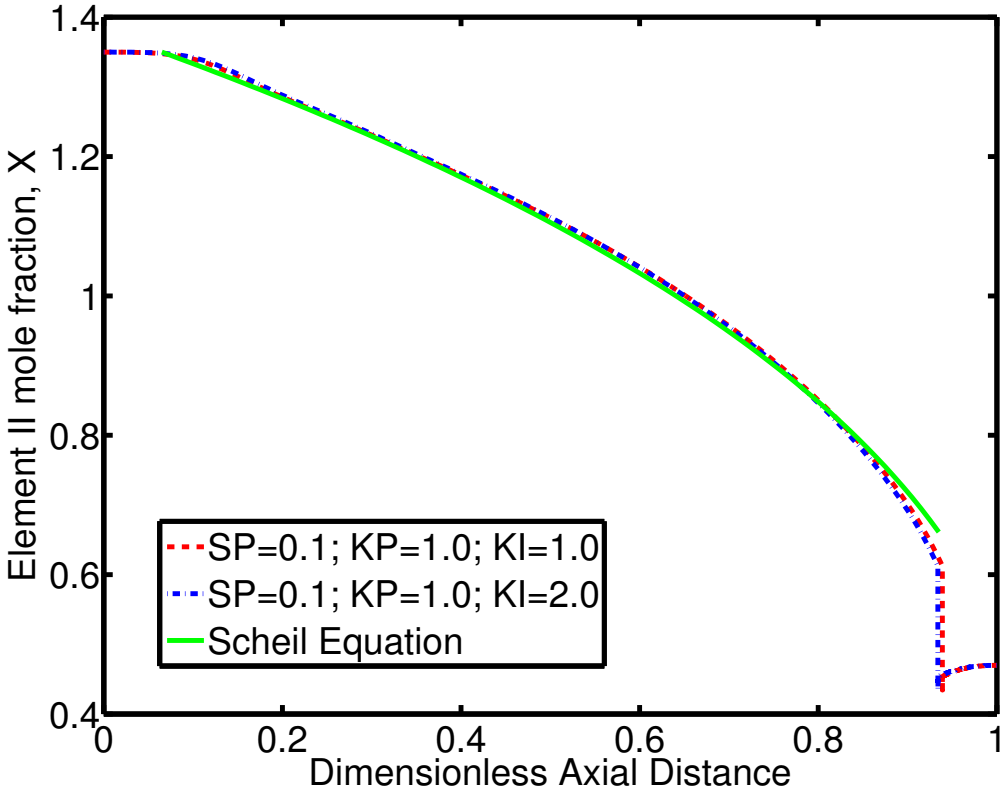

Figure 4.12: The axial segregation behavior of the local model results with PI controller along the centerline, and the Scheil Equation

in calculations of Chapter 3

4.4.3 CrysMAS verification of the adaptive bell-curve profile

The transient results computed using Cats2D employed the idealization of furnace heat transfer represented by eq. (4.1). Quasi-steady CrysMAS simulations were performed for a more rigorous representation of furnace heat transfer to verify these predictions for the adaptive bell-curve simulation. Figure 4.14 shows the results of these computations where several of the adaptive bell-curve profiles for later stages of growth have been applied. The CrysMAS computations are consistent with the Cats2D predictions, demonstrating again that the bell-curve profiles are able to maintain a convex interface shape in later growth

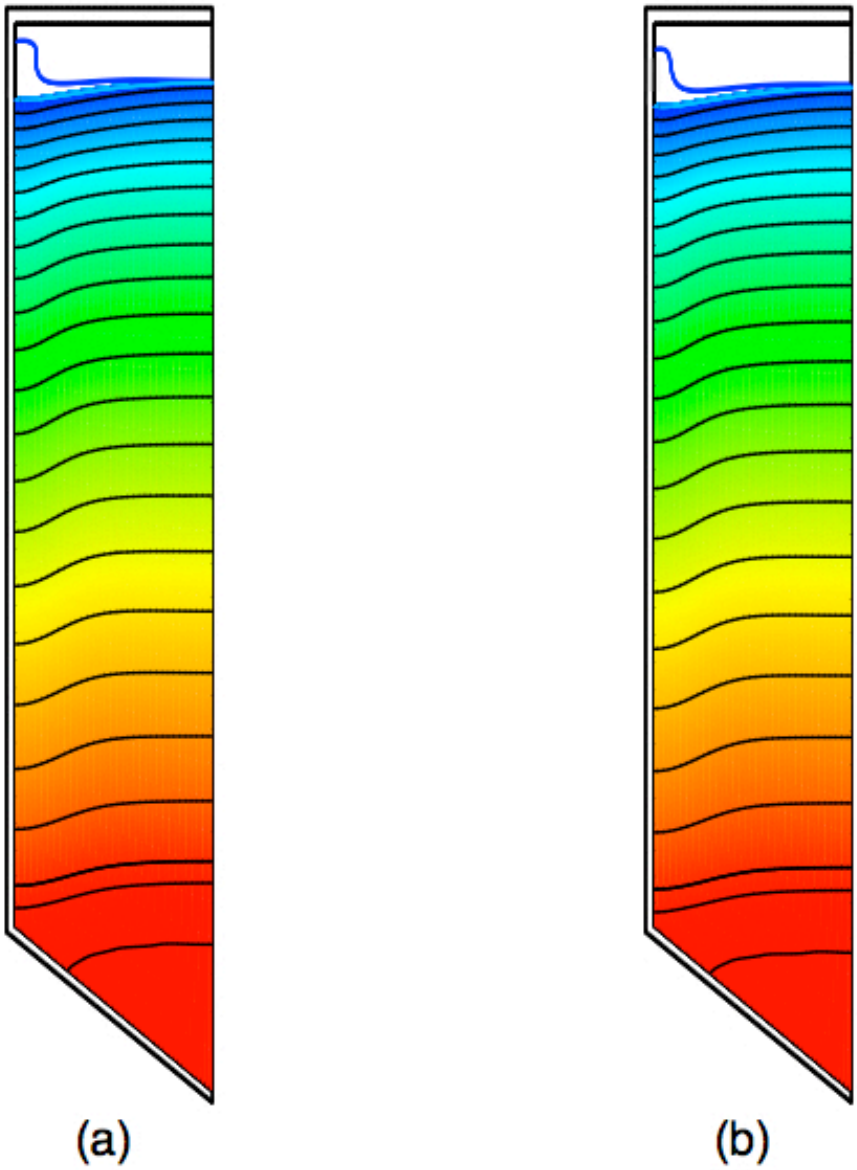

Figure 4.13: The radial segregation behaviors of the local model results with PI controller. (a) $SP = 0.1, KP = 1.0, KI = 1.0$; (b) $SP = 0.1, KP = 1.0, KI = 2.0$

stages.

4.5 Conclusion

We propose a novel furnace profile for an electrodynamic gradient freeze (EDG) process that promotes macroscopically convex interface shapes during the growth of cadmium zinc telluride (CZT). This bell-curve furnace profile is inspired by heat transfer that gives rise to a moving liquid zone and convex interface during growth by the traveling heater method (THM), particularly the notion of directing heat inward near the solidification interface. This general idea is not new; indeed, Jasinski and Witt [202] specifically discussed localized heating of the crucible surface at the interface location to reverse its shape from concave to convex. Yeckel et al. [58] also considered the effect of local heating to modify interface shape in their analysis of a CZT Bridgman system.

Here, we have employed sophisticated, furnace-scale analysis by computing quasi-steady solutions using CrysMAS to further develop these ideas. These computations affirm the ability to redirect heat flows and thereby significantly affect interface shape, even with relatively minor changes in the form of the bell-curve profile. While these profiles successfully achieve the desired convex interface shapes, there are some concerns about this approach. First, as explained by Jasinski and Witt [202], the effects of thermal conductivity mismatch among crystal, melt, and ampoule wall can conspire to give rise to locally concave interface shapes near the ampoule wall; see. e.g., the cases shown in Figures 4.3(b) and 4.6(c). However, this effect is mitigated under some profiles, as demonstrated by the interface shapes shown in the cases of Figure 4.14, which do not seem to exhibit the locally concave interface shape. Second, the heating by the bell-curve profile gives rise to destabilizing axial temperature profiles over the upper portion of the melt, thus driving stronger flows. The transient Cats2D simulations presented here showed no evidence of time-dependent, oscillatory flow instabilities, such as observed by Kim et al. [34, 35] and Müller et al. [52] and predicted by Sonda et al. [209] in destabilizing Bridgman systems. However, such destabilizing configurations may excite three-dimensional instabilities that cannot be represented by our two-dimensional, axisymmetric computations. Both of these issues merit further study.

While prior analyses have suggested heat transfer modifications to achieve convex interface shapes in the context of quasi-steady operation [202, 58], such approaches are static and not able to maintain a convex interface over an entire growth run. Thus, the strategy to dynamically adapt the furnace profile is of particular significance. We have shown that

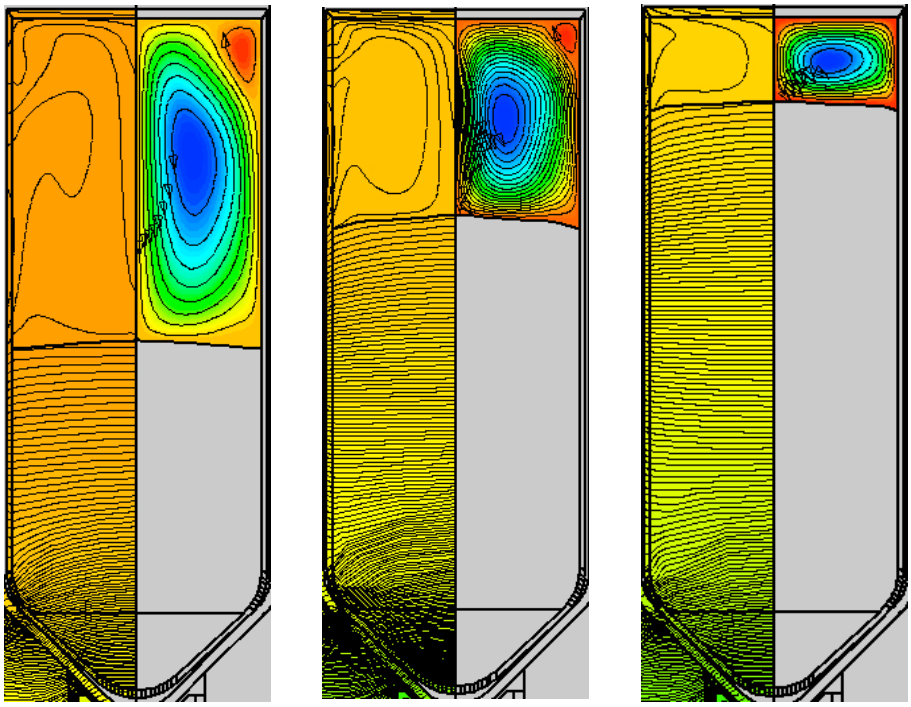

Figure 4.14: Comparison of isotherms (left), melt streamlines (right), and interface shape from quasi-steady CrysMAS simulations of EDG growth of CZT. Cases correspond to selected times that correspond to the adaptive bell-curve profiles. Isotherm spacing of $\triangle T = 1.5K$ is used for all plots. Streamfunction limits are: (a) $\Psi_{max} = 8.74 \times 10^{-02} m^2/s$ (clockwise), $\Psi_{min} = -4.88 \times 10^{-01} m^2/s$ (counter-clockwise). (b) $\Psi_{max} = 3.64 \times 10^{-02} m^2/s$ (clockwise), $\Psi_{min} = -5.37 \times 10^{-01} m^2/s$ (counter-clockwise). (c) $\Psi_{max} = 1.87 \times 10^{-04} m^2/s$ (clockwise), $\Psi_{min} = -1.60 \times 10^{-01} m^2/s$ (counter-clockwise).

a control equation solved in conjunction with transient simulations allows for the computation of a time-evolving, bell-curve profile that keeps the interface shape very nearly constant at all times. With a sufficiently accurate thermal model, this approach may be employed to generate a series of dynamic set points for the heaters in a suitable multi-zone furnace toward achieving interface shape goals. It is easy to envision the extension of these ideas to attain multiple objectives, such as the simultaneous goals of convex interface shape and constant growth rate. It is also likely that dynamic profiles other than the specific one considered here may be successfully employed. Finally, we comment that a segregation analysis for the transient simulation employing the adaptive bell-curve profile shows minimal radial variations (as shown in Figure 4.13) and a Scheil-like axial variation of zinc composition as shown in Figure 4.12, a situation much more favorable than the anomalous zinc segregation sometimes obtained in classical EDG systems [207].

In summary, we have presented a new, bell-curve furnace profile design for the melt growth of CZT in an EDG furnace system that promises to achieve macroscopically convex solid-liquid interface shapes. This strategy represents a significant advance over prior approaches for interface shape modification, such as the pedestal modifications analyzed by Kuppurao et al. [14] and Gasperino et al. [167] and employed by Carcelén et al. [198] and Crocco et al. [199]. Unlike pedestal modification, the bell-curve profile can be applied in a multi-zone furnace without significant design changes in the heat transfer package and it can be dynamically adapted to control interface shape at all times during growth. In line with recent CZT growth results [198, 199], realizing a convex solidification interface via this adaptive bell-curve furnace profile promises better crystallinity and higher yields than traditional CZT growth techniques.

Appendix: Mathematical representation of the bell-curve furnace profile

The bell-curve thermal profile for the furnace contains two pieces, a linear segment applied below the melting temperature and a parabolic segment applied above the melting temperature. Gradient-freeze growth is driven in the system by keeping the end-points of the profile fixed while moving the connecting, melting-temperature point at the desired translation rate. The mathematical form of this profile is described below.

A cold temperature, T_c, is defined at the location of the ampoule tip, which is the origin of our axial coordinate system, $z = 0$. This point is connected by a linear segment to

the melting-point temperature, T_m, which is positioned at an axial point, $z_m(t)$, that is translated in time to achieve solidification. A parabolic bell-curve profile is attached to the melting-point temperature at $z_m(t)$ and is set to the same temperature, T_m, at the top of the ampoule, $z = 1$. The maximum of the bell-curve is set to an amount a above the melting point, namely the peak temperature $T_m + a$, at a point equidistant between $z_m(t)$ and $z = 1$.

Thus, the mathematical form of the furnace profile is

$$T_f(z,t) = \begin{cases} T_m \left(\dfrac{z}{z_m(t)} \right) & \text{for } 0 \le z \le z_m(t), \\ \\ T_m + 4a \left(\dfrac{z - z_m(t)}{1 - z_m(t)} \right)^2 & \text{for } z_m(t) \le z \le 1. \end{cases} \tag{4.3}$$

The growth run is then simulated by moving the melting-point location at a constant speed corresponding to the applied translation rate, namely

$$z_m(t) = z_{m,0} + \left(\frac{V_p}{L} \right) t, \tag{4.4}$$

where $z_{m,0}$ is the position of the melting-point temperature at $t = 0$, V_p is the translation rate, L is the characteristic length used to make z dimensionless, namely the height of the ampoule, and t is time.

I

Chapter 5

Thermal Analysis of Quenching during EDG CZT Growth

5.1 Chapter Summary

A realistic Electrodynamic Gradient (EDG) Furnace model has been developed and employed to analyze the thermal field and interface evolution of quenching process of Cadmium Zinc Telluride (CZT). A variety of quenching cases have been investigated. The work presented here will focus on the thermal analysis without considering the solute-related constitutional supercooling and segregation effects. After a series of case studies, it has been found that the growth behavior, such as interface evolution, in the quenching process is highly dependent on the history of the furnace heating power profile. Compared to the typical growth rate of 1 mm/hr, the quenching growth rate could be 10-100 times larger and even reach to 110 mm/hr in the final growth period. Further work regarding convection effects and solute distribution will provide more information when assessing the effect of quenching during CZT growth.

5.2 Introduction

As noticed, most crystal growth and conventional solidification processes operate at rates of interfacial advance somewhere between micrometer per second to centimeter per second due to certain concerns with respect to various systems. Take CZT growth for example. The growth rate traditionally is around 1 mm/hr during EDG growth. Recently, more

and more experimental results of quenching process of CZT growth, such as quenching by accident and/or on purpose, have demonstrated some interesting phenomena and intrigued many crystal growers for its potential application.

Quenching, in essence, is kind of a "mistake". It occurs when an event causes a power outage and the stable growth condition is suddenly disturbed and nonexistent due to such a "thermal shock". Recently, many crystal growers have taken these failed growth runs and have attempted to analyze the resulting outcome. Typically, this is by a longitudinal etch, which then will often show a crystalline region, a polycrystalline region, and an interface between the two regions as shown in Figure 5.1.

In this study, the CrysMAS [135, 136, 137] code has been employed to simulate the quenching process of CZT during EDG growth. Here, we focused on the thermal field change and interface evolution without considering the solute-related constitutional supercooling and segregation effects. Initially, a typical, monotonically increasing thermal profile was applied by setting the power of each heating element along the furnace. When reaching the stable growth condition after certain growth time, all the power has been pulled out and the quenching process was initiated.

5.3 Model development

For the results presented here, we employ the crystal growth simulation software CrysMAS, developed by Müller *et al.* [135, 136] at the Crystal Growth Laboratory of the Fraunhofer Institute IISB, which is capable of modeling crystal growth in high-temperature furnaces with complex geometry in which radiant heat transfer is predominant. CrysMAS employs the finite volume method on unstructured and structured grids with a quasi-Newton iterative solution method.

Our model is based on Mellen electrodynamic gradient freeze (EDG) furnaces with 18 controlled heating zones (12 one-element zones and six four-element zones) with PBN crucible, as shown in Figure 4.1(a) and Figure 2.8. Initially, a traditional, monotonically increasing thermal profile was employed by setting the power of each heating element along the furnace. After certain growth time, the input powers of all the heating elements were set to be zero to initiate the quenching process. A temperature-dependent heat flux boundary condition is applied at the exterior surface of the furnace. The solid–liquid interface is tracked to coincide with the melting-point isotherm. Please refer to Chapter 2 for a more complete model description. Physical properties for materials used in the furnace are

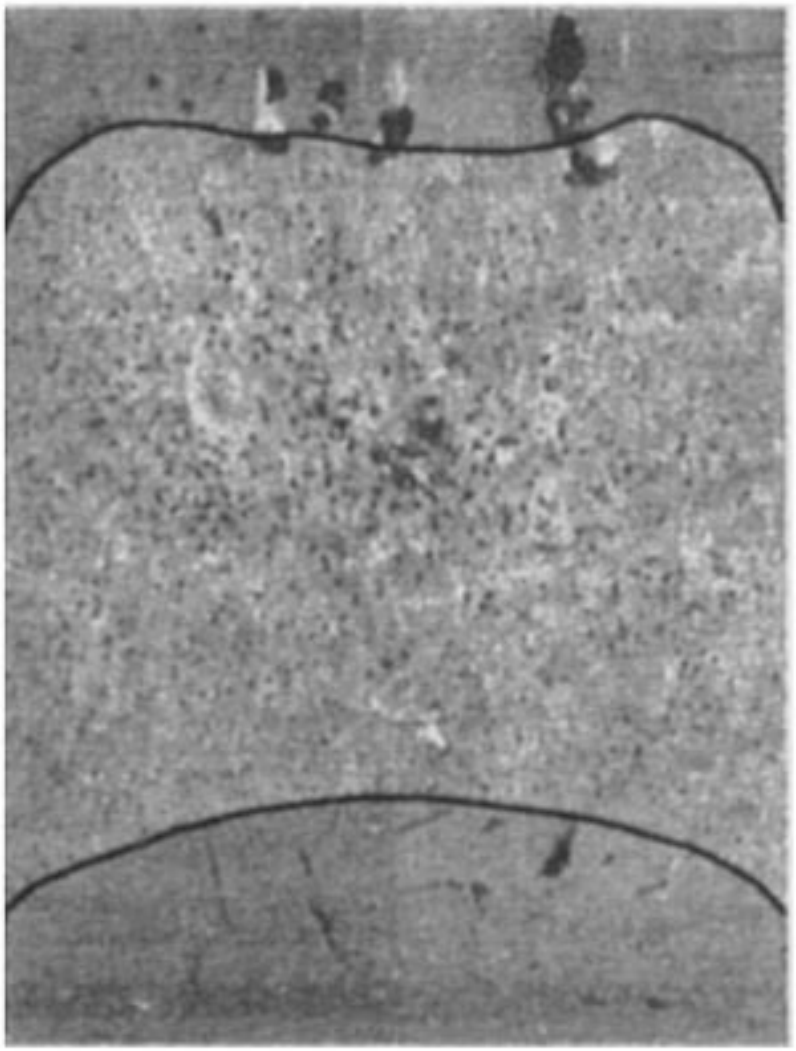

Figure 5.1: A sample outcome of quenching process of CdTe [4]

assumed to be constant with temperature and a list of physical properties employed are described in Table 6.1 and Table 3.2 in Chapter 3.

5.4 Results and Discussion

In order to obtain a initial growth solution, a QSS simulation is performed based on the hybrid mesh (Figure 2.8) where a classical temperature profile similar to the one used by Gasperino et al. [138] is applied by specifying furnace set-point temperatures. Inverse calculation is employed here to obtain the heating power for each of the total 18 heating elements, which will be the initial heating power setting for the following transient quenching growth of CZT crystal where a time-dependent power profile will be applied to each heating element. The QSS result is presented in A1 of Fig. 5.2 and same as B1 and C1 in Fig. 5.3 and Fig. 5.5.

5.4.1 Base case results

The base case results are displayed by Figure 5.2. After initializing the time-dependent simulation from QSS solution A1 of Figure 5.2, the same heating power settings have been maintained for 5 minutes to allow the growing system to accommodate itself to the transient environment. At time= 0.0834 hr, the heating power of each and every heating element is set to zero, and the CZT material will solidify in a quasi-quenching manner, which is simulating the physical quenching process for EDG system in experiments. The transient simulation results are shown in Figure 5.2 from A1 to A10 corresponding to different growth stages. The interface shape and position is marked by the dark black line between upper melt phase and lower solid phase. Only on the right-hand side of each figure the isothermal contours are shown to clearly display the evolution of the interface shape during quenching.

Initially, the interface is convex towards melt phase. After turning off the power, the interface adjacent to the inner crucible gradually changed to concave while still convex in the center region. As quenching proceeds, the melt started to solidify from the contacting area with the inner crucible and the top, which formed a trapped melt region within the solidifying crystal, as shown from A3 of Figure 5.2 to A7. After, the melt has been totally solidified, and no more melt phase exists. We could also notice that the thermal gradient in solid has been increasing indicated by the even denser spacing of isothermal contours, as the melt retreats to the center "island" within the solid, and the gradient inversely decreasing

after the solidification completed. Heat flows from lower inner part to the upper outer part afterward.

5.4.2 The effects of heating power history

In order to fully understand the quenching process of CZT crystal growth in an EDG system, several test runs have been performed. Two sets of results have been presented here in Figure 5.3 and Figure 5.5, case B and case C respectively.

Compared to base case results (Case A), the history of input power of each heating element is designed to reach the stable growth condition with growth rate equal to 1 mm/hr after the initial transient stage, as shown in Figure 5.6(A), and then the quenching process is initiated by setting the power to zero. For case B, the crystal grew from B1 to around B2 of Figure 5.3, a longer stable growth period (about 2 hours) compared to case A, and then quenching process proceeds by turning off powers of all heating elements. As we can see from Figure 5.3, the interface started to be concave as the quenching started, and the solidification also started from the contacting region with inner crucible wall due to the intense outward heat flux. Again, a trapped melt phase occurred, then disappeared. It is notable that the thermal gradient in the solid during quenching did not behave as in case A, but gradually decreased until almost uniform temperature occurred in the very final stage (time=52.6 hr), as shown in B10 of Figure 5.3. Another difference is that the heat flows from upper inner part to the lower outer part, as indicated by the color mapping and shape of isothermal contours in Figure 5.3.

In order to further demonstrate clearly the time-dependent heat flow during the quenching process of CZT crystal growth, several typical states have been captured and presented in Figure 5.4 regarding case B. Here we can easily see the evolution of the heat flux, especially around the interfacial domain. For example, the heat flux is mainly downward, and inward around the edge of interface adjacent to the inner crucible wall, which caused the convex interface shape as shown in D1 of Figure 5.4. Following is the state of D2, where the heat flux is also basically downward but outward around the interface, and the concave interface occurred due to the rapid growth rate and conductivity mismatch. Afterwards, the heat were characteristically flowed outwards from the center melt island (D3), and similar pattern maintained even after the completion of solidification process (D4).

Similarly, the results of case C, as shown in Figure 5.5, presented same characteristics as case B, except that the stable growth condition with growth rate of 1 mm/hr is maintained

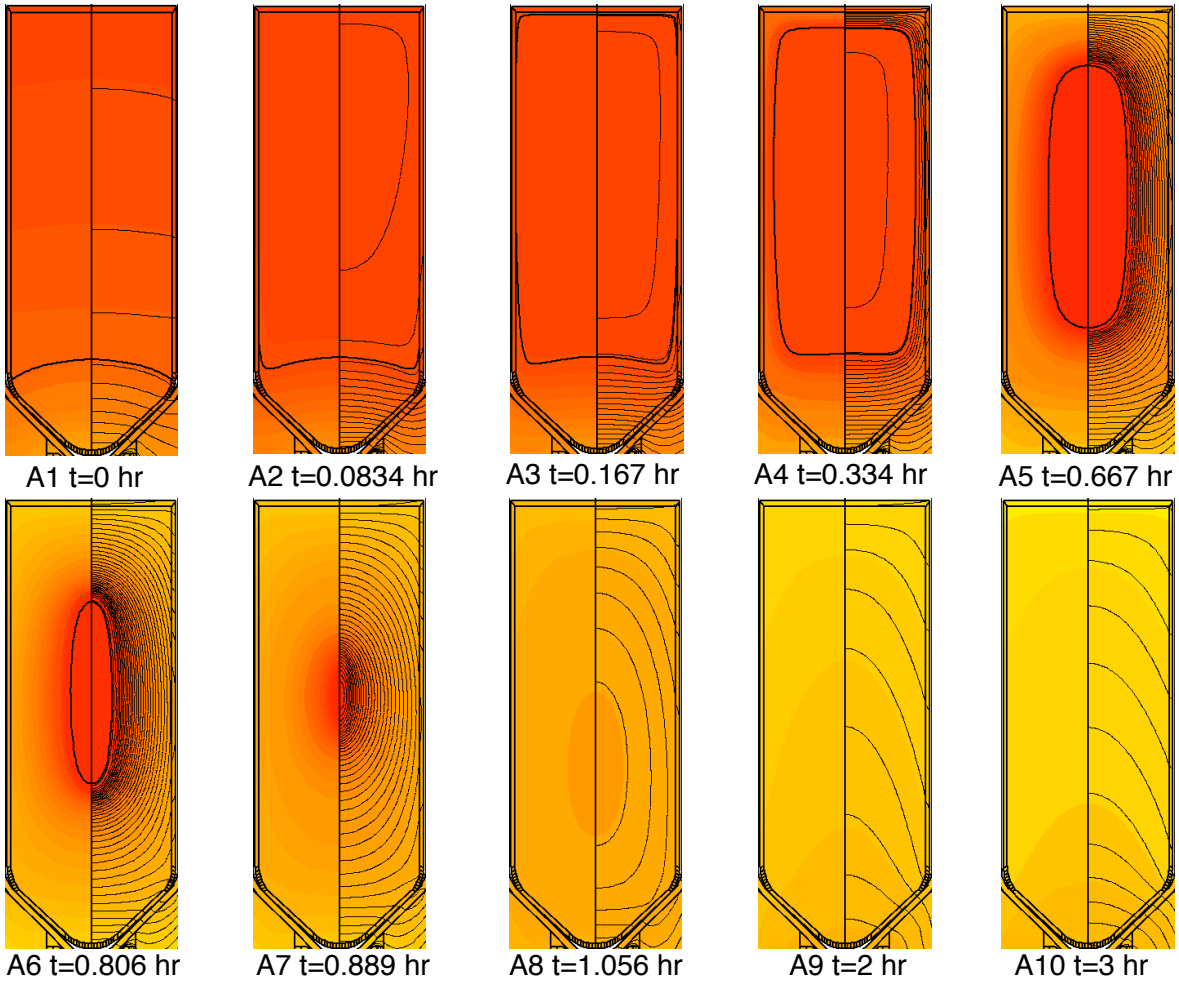

Figure 5.2: Base case results of transient simulation (Case A). The dark black line indicates the interface between melt and crystal. The isothermal contours are shown on the right-hand side of each figure, and spacing between contours is equal for all the results presented here

for an even longer period (around 4 hours), as shown in C2 of Figure 5.5, before starting the quenching process by setting heating powers to zero. Here we noticed that the trapped melt region occurred much closer to the top region (as shown in C7 and C8 in Figure 5.5), and the radial thermal gradient in the solid is much smaller compare to case A and case B, which is beneficial concerning to the thermal stress and strain issue after growth.

5.4.3 Comparison of growth rate

The growth rate presented here is defined as the translation rate of the lower interface along the centerline with units of mm/hr. Figure 5.6 shows the growth rate along the centerline as crystal growth. The Figure 5.6(A) is the zoomed comparison of growth rate during initial transient stage as indicated with the dash circle.

In Figure 5.6(A), we can clearly see the difference of growth rate among three cases by comparing the short-time behavior. For case A, the quenching process was initiated almost immediately (in about 5 minutes) after the growth rate reaching to the applied pulling rate of 1 mm/hr by setting powers to zero. In other words, the quenching process occurred right after the beginning of the solidification process. This case serves as an extreme situation and base case for comparison. For case B and C, the growth rate experienced a initial transient stage, featured by the overshooting of growth rate (2.2 mm/hr) which is about twice of the applied pulling rate, and then dropping back and catching up with the applied pulling rate of 1 mm/hr. Such growth behavior is typical and agrees well with the experimental results [185] and our previous results [207]. Compared to case A, the stable growth period with slower crystallization rate used in practice has been maintained for about 2 hours and 4 hours for case B and C respectively before launching the quenching process.

The long-time behavior is presented in Figure 5.6(B). For case A, the growth rate keeps increasing sharply since the beginning due to the immediate launching of quenching process. While for case B and C with longer stable growth period, because of the low heat conductivity of CZT and the generally high heat capacity of semiconducting compounds (45–60 $J/mol \cdot K$ for CZT), such a "thermal shock" of quenching process by turning off the powers is not capable of dramatically change the rate of interface advance immediately, therefore the system went through a stage with a gradually increasing growth rate after launching the quenching process, then followed by the stage with sharp increase of growth rate, which is similar to case A. Also due to same reason, the position of the final-to-freeze region (the trapped melt) for case A is in the middle within the crucible (about 0.5 of the

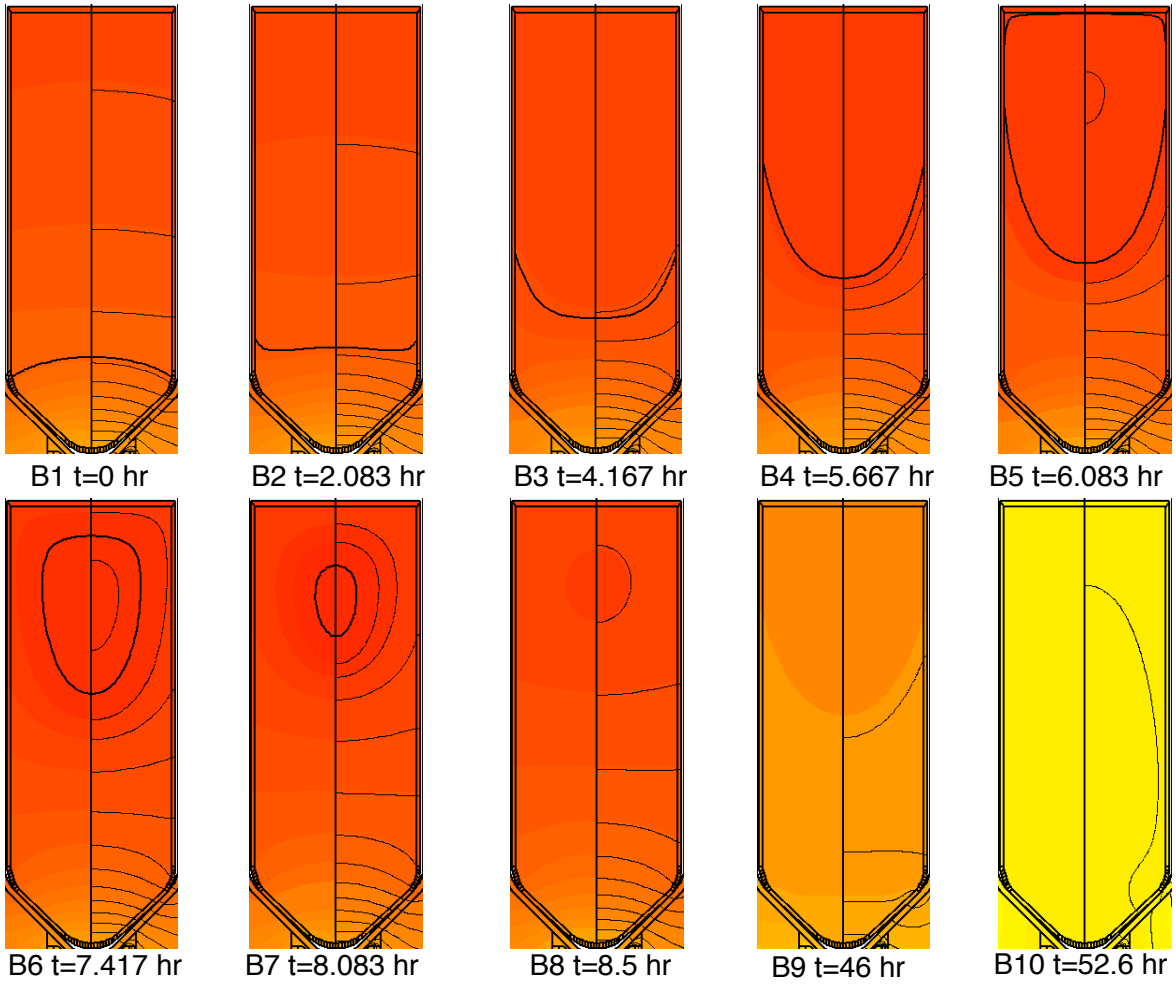

Figure 5.3: Transient simulation results of quenching (Case B). The dark black line indicates the interface between melt and crystal. The isothermal contours are shown on the right-hand side of each figure, and spacing between contours is equal for all the results presented here

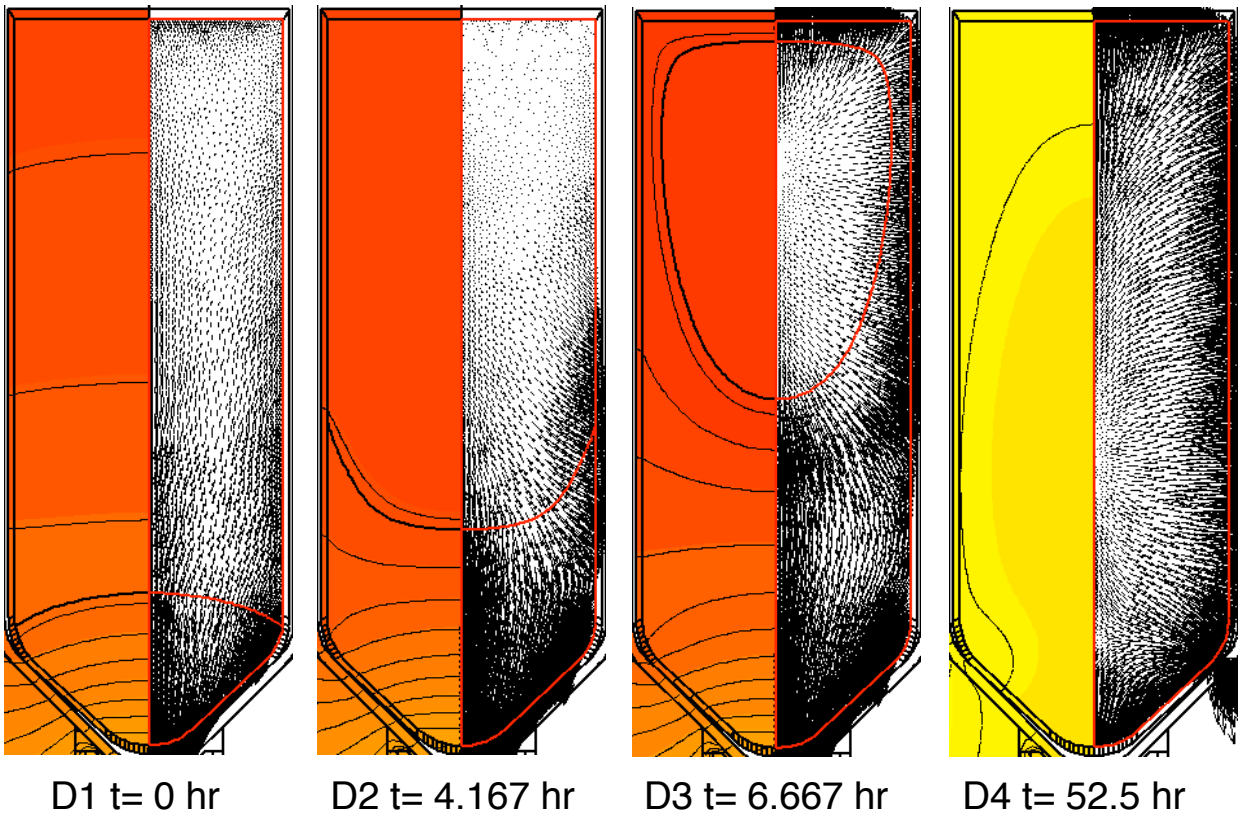

Figure 5.4: Transient pattern of heat flux (Case B). The dark black line indicates the interface between melt and crystal. The heat flux pattern is shown on the right-hand side. The isothermal contours are shown on the left-hand side of each figure, and spacing between contours is equal for all the results presented here

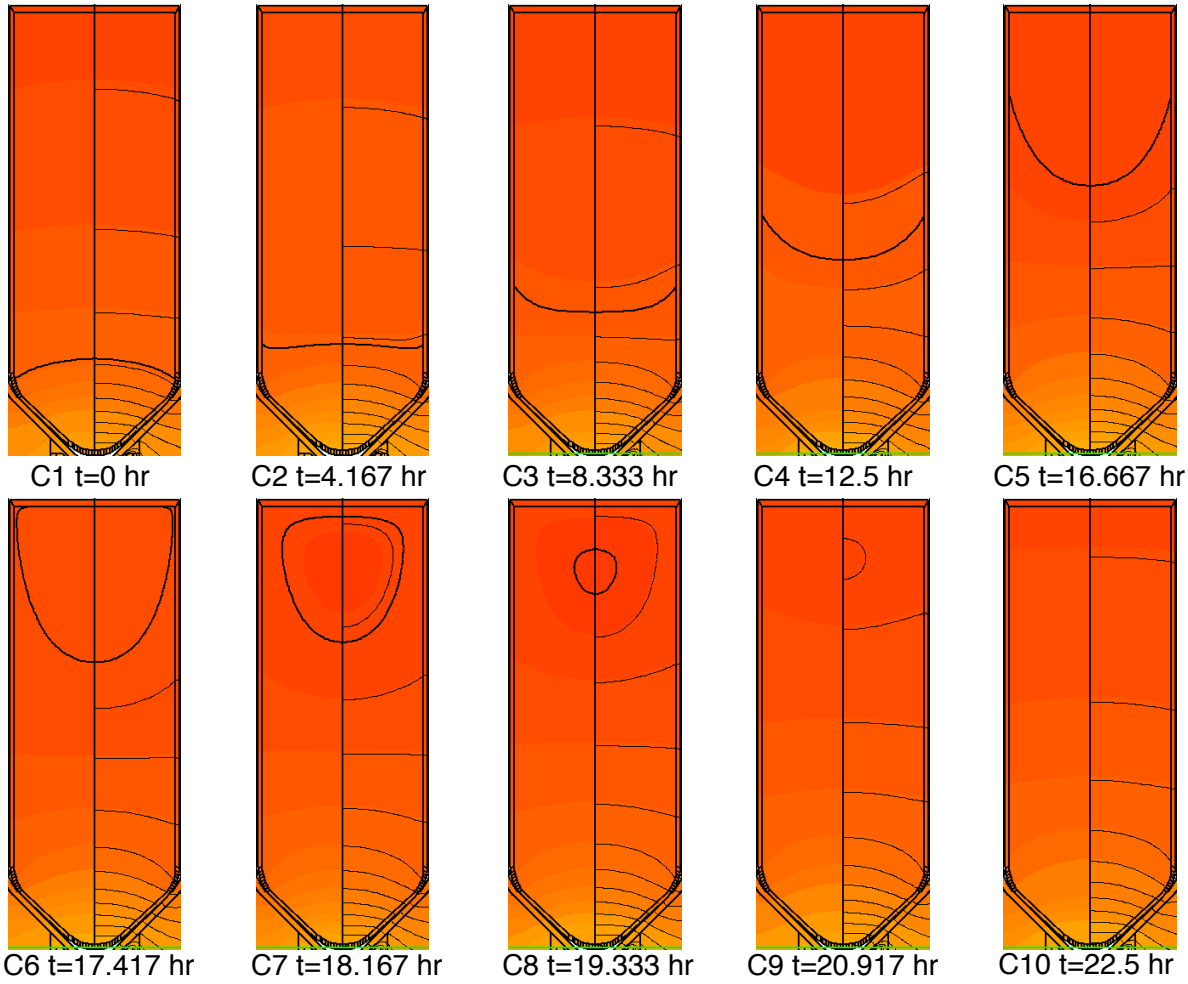

Figure 5.5: Transient simulation results of quenching (Case C). The dark black line indicates the interface between melt and crystal. The isothermal contours are shown on the right-hand side of each figure, and spacing between contours is equal for all the results presented here

dimensionless axial distance), while for case B and C, such a position is close to the top (about 0.85 and 0.9 respectively) as indicated in Figure 5.6(B)

5.5 Discussion and conclusions

The results presented in this work, to the authors' knowledge, are the first to show the theoretical investigation of the quenching process for CZT crystal growth in an EDG system. Although the work has focused only on the thermal field and interface shape evolution, we believe this strategy provides some insights on the process.

Here we presented three cases of results with different histories of heating power profiles. For the base case (case A), there is no time allowed for the system to achieve the stable growth condition before launching the quenching process by setting powers to zero. Therefore, the growth rate in case A increased rapidly and the solidification occurred from all the region next to crucible wall and the trapped melt island existed in the middle region until complete solidification. However, for case B and C with a longer stable growth condition period, the growth rate increased gradually after initiating the quenching process, from the slow solidification rate associated with single crystal growth to a critical growth rate of 10–20 times larger than the slower crystallization rate, in which one may expect that the interface shape would become unstable and lead to polycrystalline growth. Then the growth rate increased in a similar way to case A due to rapid solidification of trapped melt region. Besides, these results showed the evolution of interface shape and position, namely from convex to concave to enclosed circle, and the occurrence of the trapped melt island in the final stage. Also, the thermal gradient in the solid and heat flux pattern is also highly dependent on the heating history of the system in an EDG growth, especially the initial transient stage with/without a stable growth period before launching the quenching process.

Due to the low heat conductivity of CZT and the generally high heat capacity of semiconducting compounds (45–60 $J/mol \cdot K$ for CZT), such a "thermal shock" of quenching process by turning off the powers is not capable of dramatically change the rate of interface advance immediately, therefore one can expect that such a quenching strategy is not capable of freezing the interface shape. However, a stable growth condition is very sensitive to the redistribution of solute. Consequently, a small excess of Te (3–4 at%) in the CZT melt could be used to produce a constitutional supercooled zone in the melt. The infraction of the criterion of constitutional supercooling by breaking the stable growth condition

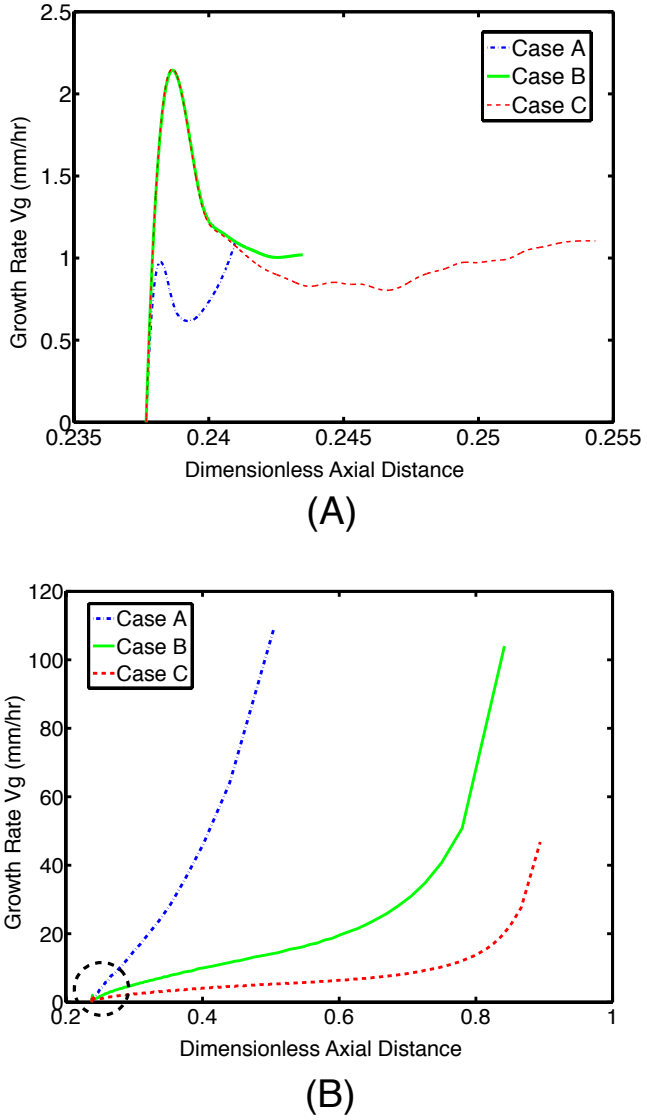

Figure 5.6: Comparison of growth rate of Case A, B and C. The initial transient stage is zoomed and presented in (A).

would allow the interface shape to be sharply visible as presented in[210]. Unfortunately, in this theoretical investigation, we ignored the effects of solute distribution and convection, although we do not expect the convection would play a key role in such a process because of the very small thermal gradient in the melt phase.

Chapter 6

Simulation of Heat Transfer and Convection During Sapphire Crystal Growth in a Modified Heat Exchanger Method

6.1 Chapter Summary

Quasi-steady-state (QSS) and transient models, developed using the CrysMAS code, are employed to study the effects of transport mechanisms and cold finger design on the temperature distribution, melt flow field, and melt-crystal interface shape during the crystal growth of sapphire by a small-scale, modified heat exchanger method (HEM). QSS computations show the importance and effects of various heat transfer mechanisms in the crystal and melt, including conduction, internal radiation, and melt convection driven by buoyant and Marangoni forces. The design of the cold finger is demonstrated to have significant effects on growth states. Notably, transient computations on an idealized heat transfer model, supplemented with QSS calculations of a model with rigorous heat transfer representation, show that non-uniform growth conditions arise under uniform cooling of the system via a linear decrease in furnace set points. We suggest that more uniform HEM growth conditions may be achieved by using nonlinear cool-down strategies.

6.2 Introduction

Sapphire single crystals have been in continuous production for over 130 years [211] and have recently garnered much attention as an important substrate material for the fabrication of gallium-nitride light-emitting-diodes (LEDs). Theses solid-state devices promise great energy savings over both incandescent and compact fluorescent lighting technologies, and the market is expanding at double-digit growth rates annually. Key to continuing cost reduction for such LED-based lighting is reducing the cost of sapphire without compromising quality. In this regard, the heat exchanger method (HEM) represents a promising crystal growth method for producing large boules of high-quality sapphire [211, 212, 213, 214].

In the HEM process, depicted schematically in Fig. 6.1, the charge within the crucible is melted by the heating element, with a seed crystal preserved via cooling from a heat exchanger touching the base of the crucible. Growth ensues by a programmed reduction in heater power. Therefore, the thermal field within the crucible, including both the melt and crystal phase, is sensitive to the design of heating elements around the crucible and the heat exchanger cooling system below the base of the crucible. However, detailed knowledge about growth conditions are nearly impossible to obtain from experiments in these high-temperature growth systems constructed of refractory materials. The predominant role of thermal radiation throughout the system, particularly internal radiation through the semi-transparent sapphire crystal, complicates the understanding of heat transfer. Radiant heat transfer is strongly nonlinear and sensitive to system geometry. Understanding internal radiation in sapphire crystal growth systems is particularly challenging, as past studies have shown [215, 216, 217, 218, 28, 29, 219]. In addition, the time-dependent nature of growth, driven by a prescribed cool-down schedule, complicates the understanding of this growth system.

There have been relatively few modeling efforts directed at understanding the heat exchanger method. Wang et al. [220] studied the thermal and flow fields of the HEM system for bismuth germanate (BGO) crystals using a finite element model. They assumed idealized heat transfer conditions, namely that the crucible wall was adiabatic and that the bottom of the crucible, where the heat exchanger attached, was isothermal. Brandon et al. [218, 221] employed a finite-element method to study the importance of internal radiation and predicted its effects on the interface shape and thermal field during the gradient solidification method (GSM) process of sapphire growth. Lu and Chen [222, 223, 224] studied the thermal and velocity fields and influence of the crucible geometry on the shape of the melt-crystal

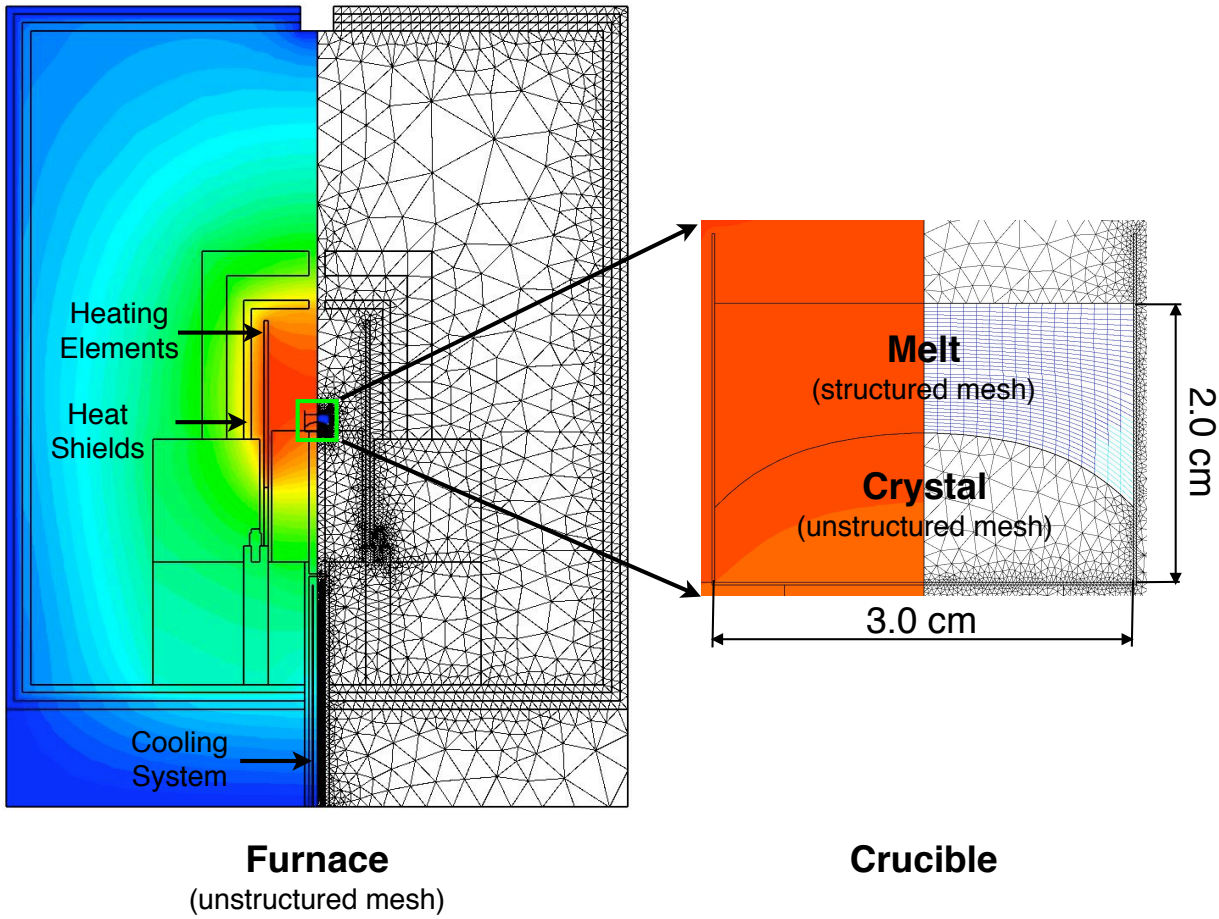

Figure 6.1: A schematic of the two-dimensional, axisymmetric HEM furnace model, showing the meshed domains employed for simulations on the right of the furnace's axis of symmetry and the geometry of the crucible on the right.

interface during growth of sapphire crystals by heat exchanger method; however, the models developed in these studies employed highly idealized representations of furnace heat transfer.

In the present study, we apply a furnace-scale model to assess sapphire crystal growth in a modified HEM growth system employed by co-author Park at the Korea Polytechnic University. This research-scale growth system employs a relatively small crucible, a simple heater configuration, and a water-cooled cold finger, rather than the helium-cooled heat exchanger featured in the original HEM system [212, 213, 214]. We consider the importance of fundamental heat transfer mechanisms and cold finger design on growth conditions, particularly interface shape, and probe the transient nature of growth in this system in the ensuing analyses.

6.3 Computational model

We employ the code CrysMAS, a powerful, finite-volume code developed by the Crystal Growth Laboratory of the Fraunhofer Institute of Integrated Systems and Device Technology (IISB) in Erlangen, Germany [135, 136, 137]. CrysMAS is capable of computing realistic furnace heat transfer, along with thermal, flow, and interfacial phenomena in melt crystal growth systems. CrysMAS solves the energy conservation equations using an unstructured triangular grid and the finite volume method. The interface between melt and crystal is tracked to coincide with the melting-point isotherm of the system. A hybrid method allows for the generation of a structured mesh over the melt for the computation of fluid flow and heat transfer in that domain. Radiation heat transfer calculations are performed via view factors and an enclosure method. Inverse calculations are performed to compute heater powers needed to obtain a specified set-point temperature in both quasi-steady and transient calculations.

The model developed here is based on the HEM furnace in Korea Polytechnic University. A schematic diagram of the system and the computational domain for the model, showing the location of the heating elements, the cooling system, and a representation of the finite volume mesh, is presented in Fig. 6.1. A molybdenum crucible, 3 cm diameter by 2 cm high, sits upon a refractory ceramic base in which a molybdenum cold finger is centered. The crucible is surrounded by graphite heating elements and several heat shields, and the cold finger is cooled by circulating water well below the crucible bottom.

Due to the axial symmetry of the experimental furnace, a simplified two-dimensional, axisymmetric model is applied with the vertical system axis aligned with gravity. A

temperature-dependent heat flux boundary condition is applied at the exterior surface of the furnace. All solid surfaces in contact exchange heat via conduction, and all exposed surfaces within the furnace exchange heat via thermal radiation. Conduction heat transfer is calculated within all solid furnace elements. For all cases in this study, a set-point temperature is specified for the top center of the sapphire melt, from which the corresponding heater input is computed.

Various heat transfer mechanisms are considered to be active within the melt and crystal, including conduction and internal radiation within the crystal and conduction and convection within the melt. The melt-crystal interface is assumed to lie upon the melting-point isotherm, and latent heat is generated by solidification at this interface. Internal radiant heat transfer is approximated by assuming a perfectly transparent medium and computing enclosure radiation within the crystal, a technique that provides a good approximation for systems with low optical thickness [215, 216, 217]. No-slip boundary conditions for melt flow are employed at all solid surfaces within the crucible. Buoyancy body forces created by temperature distributions drive flows in the melt, and a traction boundary condition is applied to account for the Marangoni traction forces at the melt-vapor interface.

Both quasi-steady-state (QSS) and transient simulations are employed. Finally, physical properties for materials used in the furnace are list in Table 6.1 and are assumed to be constant with temperature.

6.4 Results and Discussion

6.4.1 QSS calculations

In order to assess the relative importance of various heat transfer mechanisms and cold finger design, a series of quasi-steady-state (QSS) computations were carried out and are presented below. This approach assumes that the time scales associated with heat transfer and melt flow are much shorter than that of the growth cycle, so that the state of the system at any point in time is represented by a steady-state calculation for the temperature and flow fields. For these computations, we assume that the melt-crystal interface is growing at a uniform velocity of 6 mm/hr set by the cool-down rate in the furnace, unless otherwise stated.

Table 6.1: Physical properties for the furnace simulations

Property [Unit]	Description	Value	Ref.
Thermal conductivity $[W/cm \cdot K]$	Sapphire crystal	3.5×10^{-2}	[225]
	Sapphire melt	3.5×10^{-2}	[225]
	Molybdenum crucible	1.0	[221]
Density $[g/cm^3]$	Sapphire crystal	3.96	[226, 227]
	Sapphire melt	3.0	[224]
Emissivity	Sapphire crystal	1.0	[221]
	Sapphire melt	0.33	[224]
	Molybdenum crucible	0.3	[228, 226]
Heat Capacity$[J/g \cdot K]$	Sapphire crystal	1.56	[222]
	Sapphire melt	1.3	[221]
Heat of Fusion $[J/g]$	Sapphire	1100	[226]
Melting Temperature $[K]$	Sapphire	2323.15	[226]
Thermal Expansivity $[1/K]$	Sapphire melt	1.8×10^{-5}	[221]
Dynamic Viscosity $[Pa \cdot s]$	Sapphire melt	4.75×10^{-2}	[229]
Thermalcapillary coefficient$[dyn//m \cdot K]$	Sapphire melt	-3.5	[221]

Effects of internal radiation and melt convection

QSS calculations for the system at an early stage of growth, all featuring the same set-point temperature at the top center of the melt, are shown in Fig. 6.2. The calculation shown in Fig. 6.2(a) shows isotherms for the case where conduction heat transfer alone is assumed to occur in the crystal and melt phases. The maximum temperature occurs along the outer crucible wall, and isotherms show the effect of heat flowing radially inward from these walls while flowing out of the system toward the upper melt surface and the crucible bottom. A relatively thin crystal is present, with a convex interface shape curving downward. The smaller thermal conductivity of the crystal is reflected by the closer isotherm spacing and higher gradients than in the melt phase above.

Internal radiant transfer within the crystal is added for the case shown in Fig. 6.2(b), which also assumes conduction only in the melt phase. The high temperature along the solidification interface radiates heat through the transparent crystal to cooler surfaces and results in a net increase in total heat flux through the crystal. This increased heat flux deflects the interface upward and makes the melt-crystal interface more curved, compared to the prior case without internal radiation.

The effects of melt convection, driven both by buoyancy and Marangoni effects, is shown

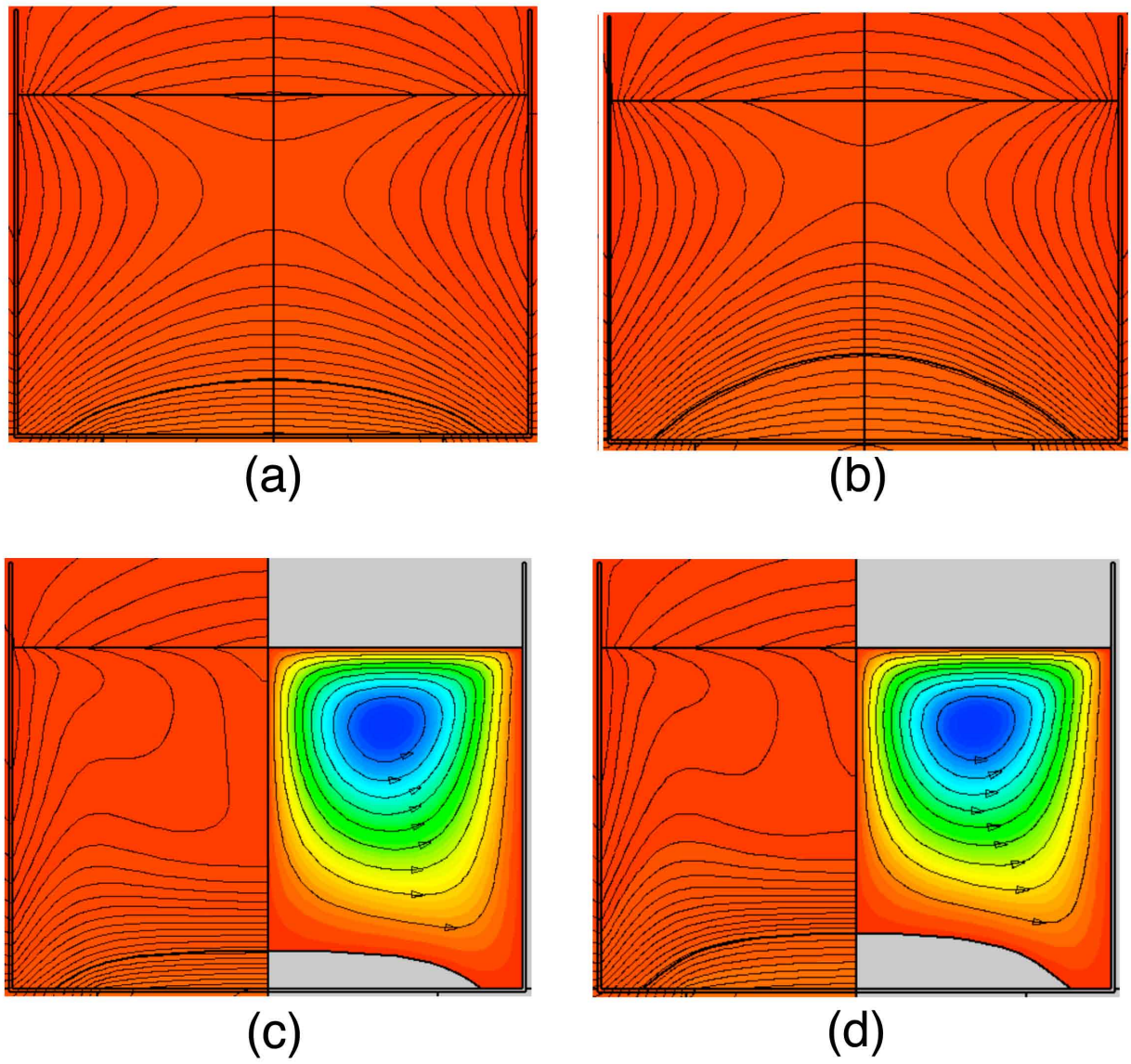

Figure 6.2: QSS simulations for early stage of growth ($t = 17.5$ min, $V_g = 6$ mm/hr) under different combinations of heat transport mechanisms in the crystal and solid. Isotherms are spaced at $\Delta T = 3$ K, and bold line indicates the melt-crystal interface. (a) Conduction only in crystal and melt. (b) Conduction and internal radiation in crystal; conduction only in melt. For the next plots, 9 equally-spaced streamfunction contours are plotted between 0 and ψ_{max} to indicate melt flows. (c) Conduction only in crystal; conduction and convection in melt, $\psi_{max} = 0.0165$ m^2/s. (d) Conduction and internal radiation in crystal; conduction and convection in melt, $\psi_{max} = 0.0162$ m^2/s.

in Fig. 6.2(c), where isotherms are displayed on the left and streamlines in the melt on the right. For this case, conduction only is computed in the crystal domain. Buoyancy moves the warmer fluid near the crucible wall upward, while cooler fluid descends along the system centerline. Marangoni flows, driven by temperature-induced gradients in surface tension, act to reinforce this flow pattern, drawing liquid along the melt surface toward the centerline, the coolest point on the melt surface. Compared to the analogous case in Fig. 6.2(a), without convection, the effects of flow are clearly visible by the distorted isotherms in the melt and the significant flattening of the solidification interface shape.

Adding internal radiant transport through the crystal, shown by the case in Fig. 6.2(d), increases the crystal size by increasing heat flows through the crystal. However, flow still acts to significantly flatten the interface over the center of the growing crystal. For this most realistic representation of the system, the driving forces for melt convection are relatively small due to the small crucible employed. For the case in Fig. 6.2(d), the maximum temperature difference across the melt is $\Delta T_{max} = 75$ K and the maximum melt velocity is $V_{max} = 0.22$ cm/s. If we use these values to compute dimensionless Grashof and Reynolds numbers, we find

$$Gr^* = \frac{R^3 g \beta \Delta T_{max}}{\nu^2} = 179, \tag{6.1}$$

$$Re^* = \frac{R V_{max}}{\nu} = 2.05, \tag{6.2}$$

respectively, where R is the crucible inner diameter, g is the gravitational acceleration, β is the thermal expansivity of the melt, and ν is the melt kinematic viscosity.

Overall, crystal transparency promotes larger deflections, while melt convection decreases interface deflection.

6.4.2 Effects of growth rate

We performed a series of calculations to probe the effects of growth rate V_g on the interface shape under quasi-steady conditions. Our first series of computations, shown in Fig. 6.3, considers conduction and internal radiation in the crystal and melt conduction alone for several growth rates, from a high value of $V_g = 6$ mm/hr to a low value of $V_g = 0.6$ mm/h. A careful examination of these cases reveals that the interface increases slightly as the growth rate is decreased, reflecting the lower amount of latent heat released along the interface.

The same growth rates are considered by the cases of Fig. 6.4, which include the effects

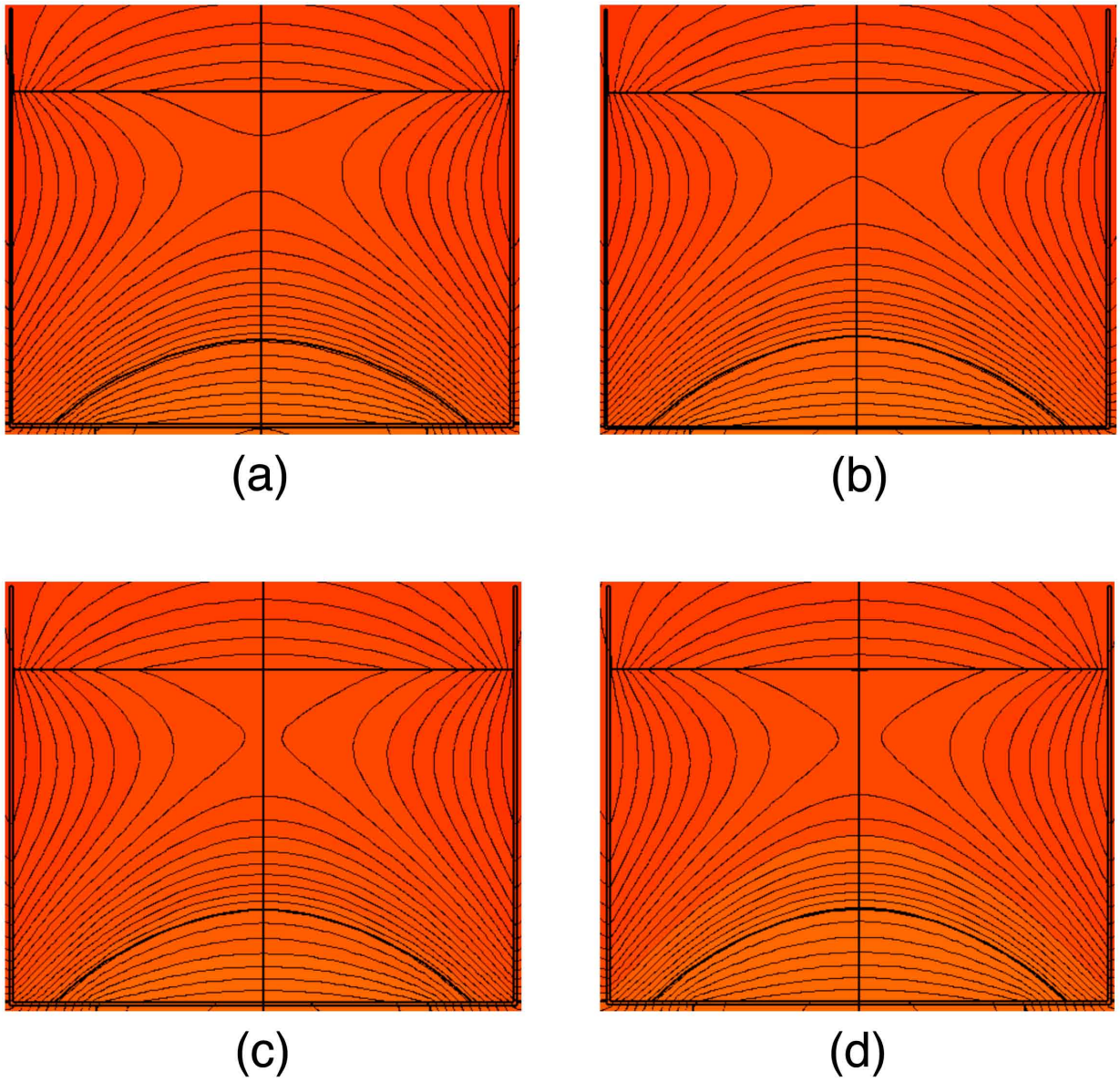

Figure 6.3: QSS simulations for early stage of growth (t = 17.5 min) with conduction and internal radiation in crystal and conduction only in melt. Isotherms are spaced at $\Delta T = 3$ K, and bold line indicates the melt-crystal interface. Growth rate is: (a) $V_g = 6$ mm/hr; (b) $V_g = 3$ mm/hr; (c) $V_g = 1$ mm/hr; (d) $V_g = 0.6$ mm/hr.

of melt convection (both buoyant and Marangoni flows). A very slight increase of interface deflection is seen as the growth rate is decreased.

6.4.3 Effects of crucible support geometry

One of the primary features of the HEM is the cold finger and its effect on heat transfer and growth. The cold finger promotes the flow of heat from the bottom of the crucible due to its much higher thermal conductivity compared to the refractory materials used for the remainder of the crucible base. Here, we consider several design variations of the molybdenum cold finger of this system.

The calculations are performed for the case of conduction and internal radiation in the crystal and with conduction and convection in the melt. Fig. 6.5 shows the variation of thermal and flow fields and interface shape with diameter of the cold finger. The base case design, with a 25 mm-diameter cold finger, is shown in Fig. 6.5(a). For the same furnace set-point temperature, a smaller cold finger, of 12.5 mm-diameter, results in a significantly different growth state, as shown in Fig. 6.5(b). Because of less heat extraction through the cold finger, the melt-solid interface is higher and its shape is more two-dimensional and curved.

Another variant in cold finger design is shown in Fig. 6.6. A wider-diameter cold finger obviously increases the heat flow from the crucible bottom, but the heat flow in such a wide finger is quite two dimensional. In these cases, we consider the effect of a smaller-diameter neck placed below the wide cold finger, with the idea that this shape might reduce the outward radial heat flow through the cold finger and promote more axially-directed cooling of the crucible.

We consider cases at a later stage of growth than those shown in the prior figure. The cases shown in Fig. 6.6(b) and (c) show that such necks substantially effect the shape of the solidification interface. As the neck is made longer, less heat is removed from the bottom of the crucible, resulting in a lower interface height for the same furnace set point. However, the more axially directed flux caused by the neck also flattens more of the center portion of the interface as the length of the neck is increased.

6.4.4 Transient calculations

Transient effects in this system are considered by the sequence of computations shown in Fig. 6.7. Fully transient simulations including internal radiation and melt convection proved

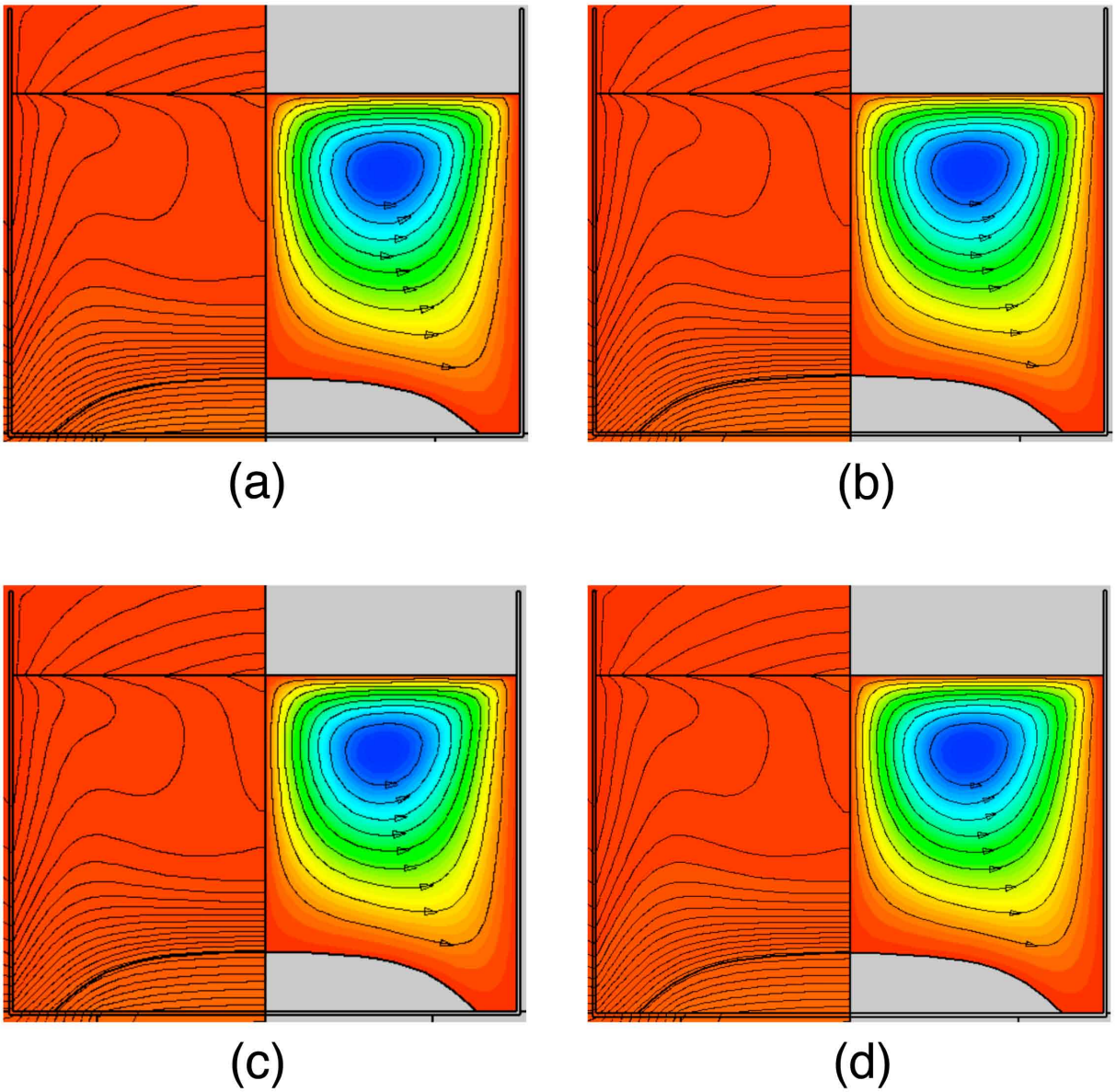

Figure 6.4: QSS simulations for early stage of growth (t = 17.5 min) with conduction and internal radiation in crystal and conduction and convection in melt. Isotherms on left are spaced at ΔT = 3 K, 9 equally-spaced streamfunction contours are plotted on the right between 0 and ψ_{max}, and bold line indicates the melt-crystal interface. Growth rate is: (a) V_g = 6 mm/hr, ψ_{max} = 0.01617 m^2/s; (b) V_g = 3 mm/hr, ψ_{max} = 0.01612 m^2/s; (c) V_g = 1 mm/hr, ψ_{max} = 0.01609 m^2/s; (d) V_g = 0.6 mm/hr, ψ_{max} = 0.01608 m^2/s.

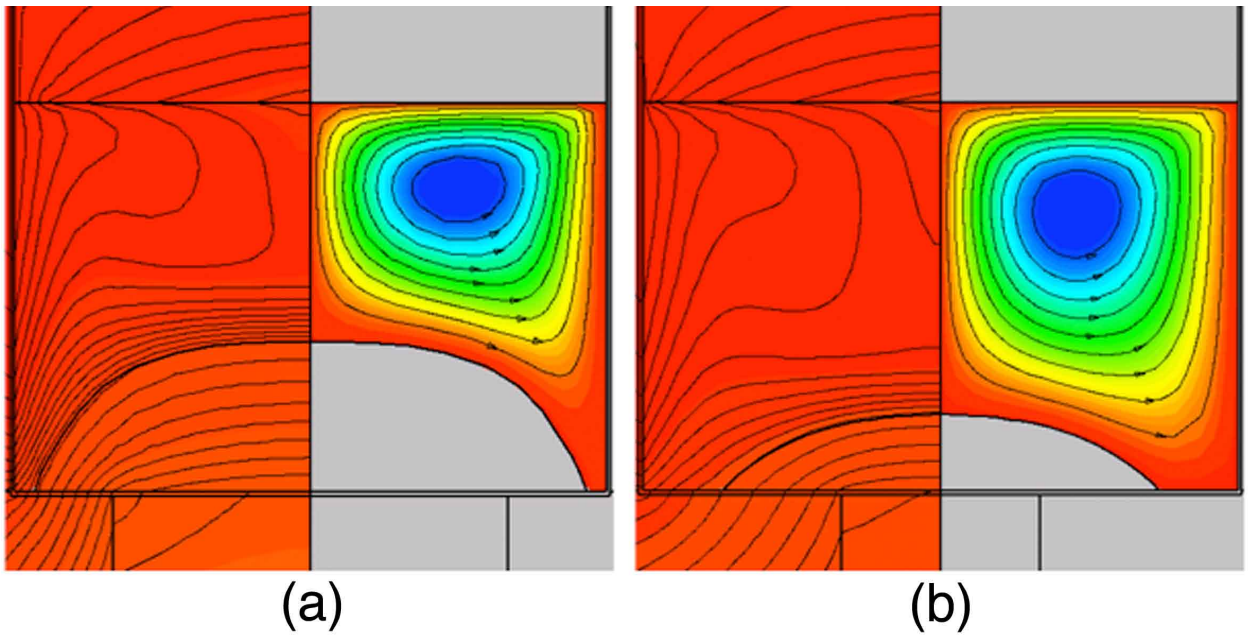

Figure 6.5: The effect of diameter of cold finger on thermal field, flow field, and interface shape under the same furnace set point. Isotherms on left are spaced at $\Delta T = 3$ K, 9 equally-spaced streamfunction contours are plotted on the right between 0 and ψ_{max}, and bold line indicates the melt-crystal interface. Cold finger diameter of: (a) 25 mm, $\psi_{max} = 0.0030$ m^2/s; (b) 12.5 mm, $\psi_{max} = 0.0147$ m^2/s.

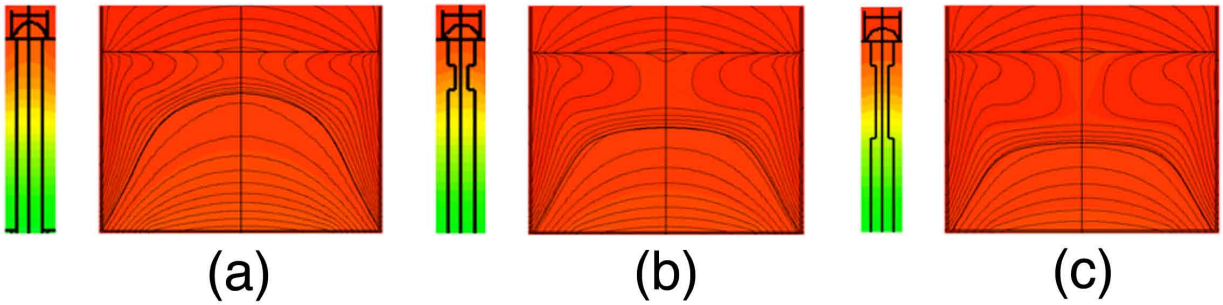

Figure 6.6: Change in temperature field and interface shape with variation in neck shape of cold finger under the same furnace set point. (a) No neck. (b) Neck length = 2 cm. (c) Neck length = 6 cm.

to be too computationally demanding, so a simplified system was employed which, while computing full exterior furnace heat transfer and the solidification interface, considered only conduction in the melt and solid. Results from this transient calculation are shown for various times in the top two rows of Fig. 6.7. As time proceeds, the crystal grows higher in the crucible and the interface becomes more deflected. Between state (g) and (h), the solidification interface breaks the surface of the melt at its coolest point, the top center. As growth continues from state (h) onwards, an annular ring of molten sapphire surrounds the top-center crystal surface, and growth continues outward until this ring of melt is fully solidified, state (j), after approximately 160 minutes.

To consider the effects of internal radiation and melt convection, shown to be very important by the results of the prior sections, we perform a series of QSS computations including these effects for the set-point temperatures corresponding to the transient cases shown in cases (a)–(e) and for an assumed growth rate of $V_g = 6$ mm/hr. These cases, which compute for more realistic heat transfer through melt and crystal, are indicated in Fig. 6.7 as cases (a*)–(e*). Qualitatively, these growth states appear similar to the idealized transient states (a)–(e), although melt convection acts to flatten the center of the interface, especially at earlier states when the melt volume is larger and the flows are stronger. We expect these computations to be reasonably accurate, even with the assumed constant growth rate they employ, due to the rather minor effect of latent heat in this system (as evidenced by the cases discussed in Section 6.4.2; also see, e.g, the discussion by Virozub and Brandon [230]).

Figure 6.8 presents a plot of the set-point temperature versus time used for the transient simulation, showing the linear ramp in set point which corresponds to a uniform growth rate of 6 mm/hr. On the same plot are data showing the height of the interface at the system centerline as a function of time, with the connected points representing the transient computation for conduction only and the open points showing results from the QSS computations for more realistic heat transfer, states (a*)–(e*) from the prior figure.

The transient interface position for the simplified heat transfer model indicates that, despite the linear set-point ramp, the growth velocity is not constant. The slope of this curve represents the instantaneous growth velocity of the interface at the centerline and is shown in Fig. 6.9. This plot indicates that, despite initial spikes showing a spurious growth and melt-back transient caused by numerics, the growth first lags behind the desired rate of 6 mm/hr. The system then approaches a period of nearly quasi-steady growth where the interface velocity is quite close to 6 mm/hr (the value indicated by the dotted line). However, after a time of approximately 90 minutes, the instantaneous growth rate increases

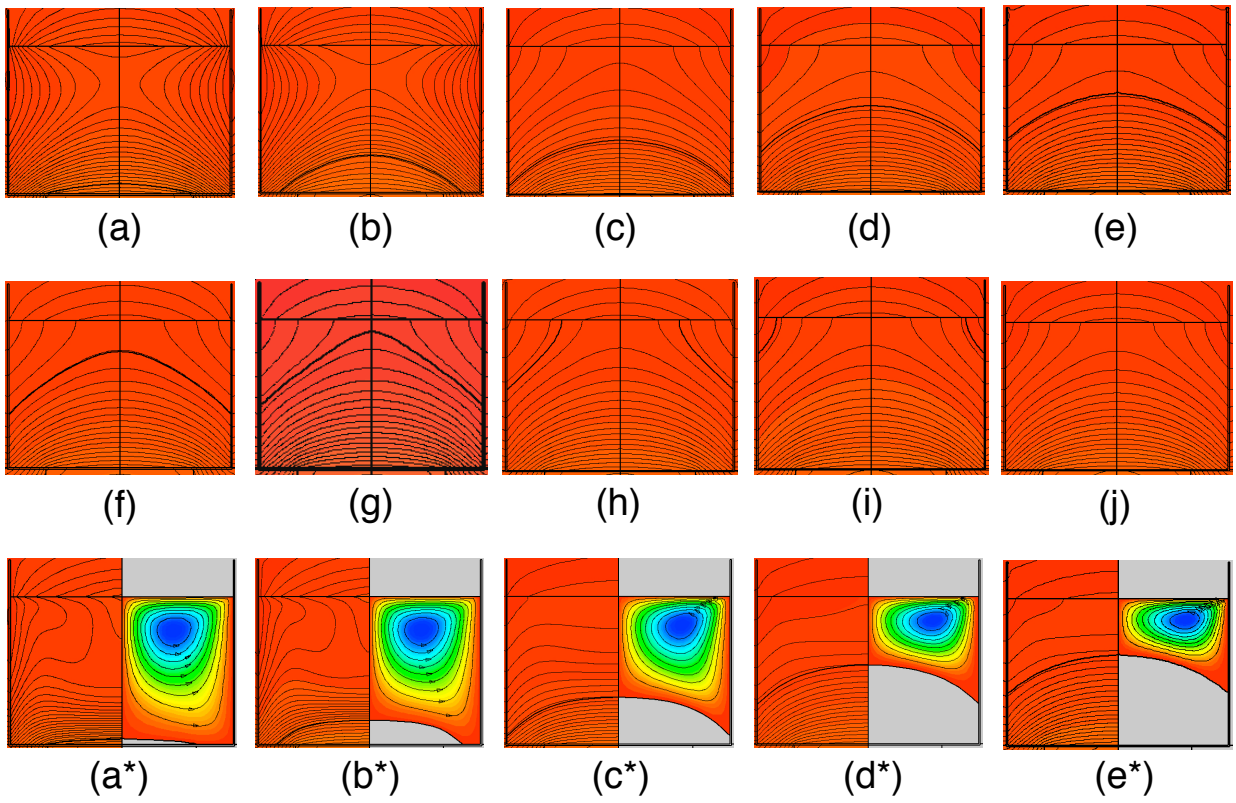

Figure 6.7: Upper rows show transient growth simulation results at various times for the case of conduction only in crystal and melt. Isotherms on left are spaced at $\Delta T = 3$ K, and bold line indicates the melt-crystal interface. (a) $t = 0$ min; (b) $t = 17.5$ min; (c) $t = 67.5$ min; (d) $t = 100$ min; (e) $t = 107.5$ min; (f) $t = 120$ min; (g) $t = 121.5$ min; (h) $t = 135$ min; (i) $t = 152.5$ min; (j) $t = 167.5$ min. Bottom row shows QSS simulation results for the case of conduction and internal radiation in crystal and conduction and convection in melt. Nine equally-spaced streamfunction contours are plotted on the right between 0 and ψ_{max}. Growth times for each case are identical to those for the states shown in the uppermost rows. (a*) $\psi_{max} = 0.0168$ m^2/s; (b*) $\psi_{max} = 0.0162$ m^2/s; (c*) $\psi_{max} = 0.00326$ m^2/s; (d*) $\psi_{max} = 0.00289$ m^2/s; (e*) $\psi_{max} = 0.00282$ m^2/s;

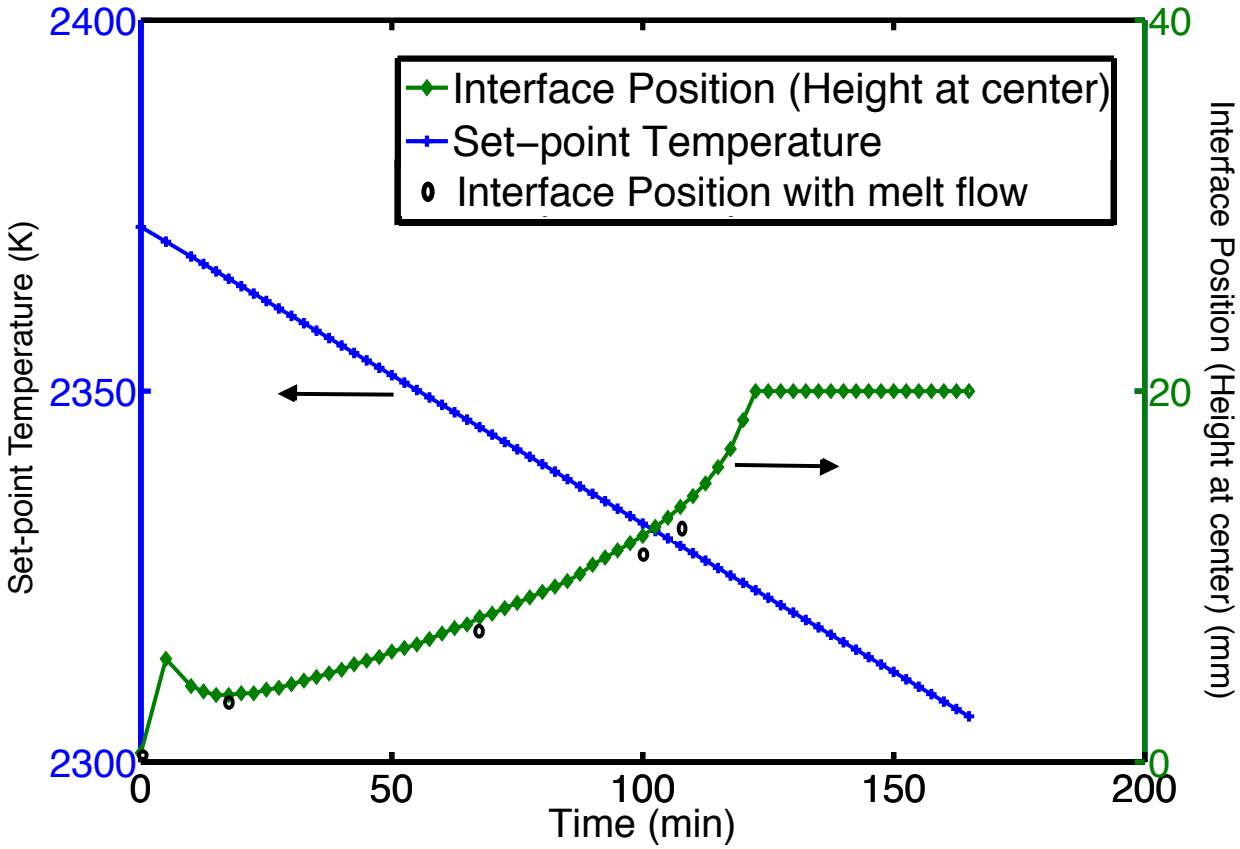

Figure 6.8: The furnace set-point temperature and melt-crystal interface heights are plotted as functions of time for the simulations shown in the previous figure. Note that even though the set-point is decreased linearly in time, the growth interface position is nonlinear.

significantly due to thermal end effects, until the interface abruptly stops after breaking through the surface of the melt at approximately 122 minutes.

Interface position for QSS computations including internal radiation and melt convection, shown as open points in Fig. 6.8, track the general trend of those of the simplified heat transfer model. However, their values are smaller, reflecting the flattening effect of convection on the interface early during growth and reducing the thermal end effects that accelerate growth in the conduction-only computation. With such a few QSS computations, we do not attempt to solve for the instantaneous velocity but note that the slope between adjacent pairs of points shows the trends of the simpler system, notably slower growth early on and faster growth (though not as much as the simple model) later in the run.

6.5 Discussion and conclusions

We have applied the powerful, crystal growth simulation code CrysMAS to model heat transfer, melt convection, and interface shape during sapphire growth in a small-scale, modified heat exchanger method employed by co-author Park at Korea Polytechnic University. Quasi-steady-state computations show that a simple model of conduction only in the crystal and melt give a qualitatively correct prediction of this small-scale system, but that internal radiation in the crystal and convection in the melt make important contributions to system behavior. In particular, internal radiation acts to move heat away from the interface through the crystal, resulting in higher interface positions and lower thermal gradients in the crystal for a given furnace set point. Melt convection acts to counter these effects by moving heat toward the melt-crystal interface, flattening its shape and reducing its overall height. QSS calculations also show that the heat transfer in this system is largely unaffected by latent heat released by solidification, with only very small changes in interface shape caused by an order of magnitude change in growth rate.

Different cold finger designs give rise to significant effects on crystal growth. Some effects were rather obvious; for example, a larger-diameter cold finger promoted greater heat flows from the crucible and more crystallization for a given furnace set point. Interestingly, alterations to the shape of the cold finger could also affect significant changes in crystal growth behavior. Here, a design with a thinner neck region below a wider contact area made the heat extraction more uniformly axial in direction, changing the interface shape. Such computations show the importance of the design of the furnace and cold finger. It is noteworthy that all states shown in Figs. 6.5 and 6.6 correspond to exactly the same set-

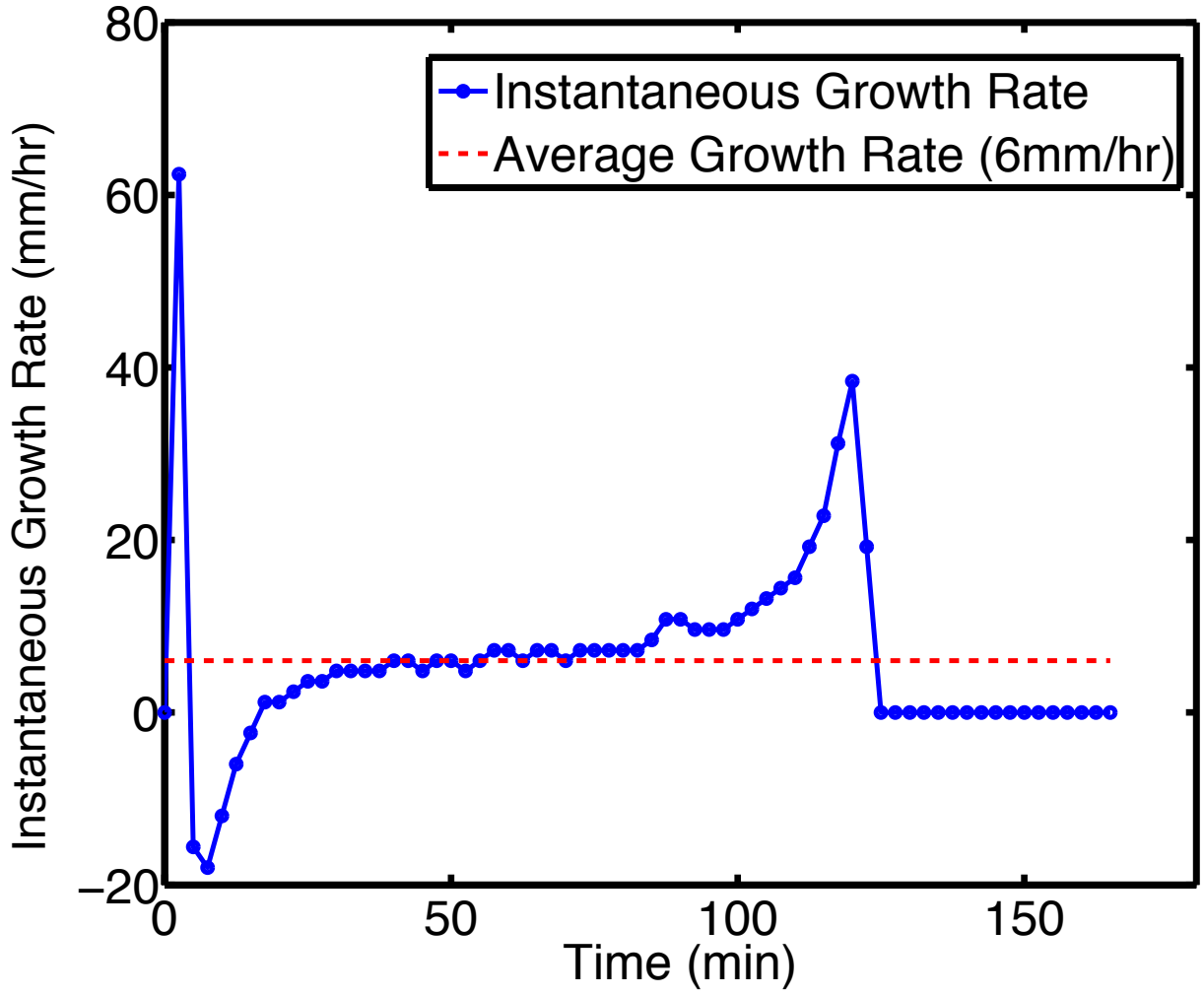

Figure 6.9: The instantaneous growth rate at the centerline is plotted as a function of time for the transient simulation of the idealized system, which considers conduction only in crystal and melt. The instantaneous growth rate matches the applied cool-down rate (average growth rate) for less than one third of the total growth cycle.

point temperature for the system and each exhibits a markedly different interface height and shape.

A fully transient computation of crystal growth, using simplified heat transfer in the crystal and melt, showed that crystal growth conditions vary significantly during the course of a growth run. In this simulation, quasi-steady-state growth rates matching the applied, linear ramp-down in temperature were achieved for less than a third of the entire growth time. Early on, the instantaneous growth rate was less than the desired rate. Growth during later stages was characterized by much faster instantaneous growth velocities, to greater than six times the desired rate, followed by an interface break-through event at the center of the melt and corner melt cooling, all quite non-uniform in time.

QSS computations with more realistic heat transfer, including internal radiation and melt convection, were performed to simulate specific states along the growth transient. While these computations showed slightly different interface shapes, they followed the general trends predicted by the simpler, transient model. Here, the convective flows were very weak, owing to the small size of the crucible. We would expect larger-scale system to be much more strongly affected by melt convection. Nevertheless, these more rigorous computations showed non-constant growth rates and non-uniform growth conditions through the run, similar to those exhibited by the transient model with only conduction.

In summary, we believe that our results demonstrate the utility of crystal growth computations for understanding heat transfer and growth in these surprisingly complicated systems. We have explained the general effects caused by different heat transfer mechanisms. In this small-scale growth system, the overall effects of internal radiation and melt convection almost counter each other; however, we would suspect that melt convection will become much more important in larger-scale HEM systems. We also observe that relatively minor changes in cold finger design can have a strong impact on melt-crystal interface shape. Finally, our computations show that growth conditions, as judged here by interface velocity, are significantly nonuniform, even when solidification is driven by a simple, linear reduction in furnace set-point temperature.

For future HEM optimization and design, we believe that rigorous computational models will play an important role. These computational tools can be employed to design suitable growth strategies for desired outcomes, such as the dynamic furnace thermal profiles constructed to achieve constant interface deflection during Bridgman growth presented in [231]. Such an approach could be applied to HEM systems to achieve nearly constant solidification velocities over the entire growth run by constructing an appropriate, nonlinear set-point re-

duction schedule. Such an approach would yield more uniform growth conditions, which may yield significant benefits in improved crystal quality and increased process yields from the heat exchanger method.

Chapter 7

Concluding Remarks

7.1 Thesis Summary

The goal of the research presented in this thesis has been to cast new light on and push forward our understanding and control of transport processes in complicated crystal growth systems via multi-scale numerical experiments. Through the application of detailed, realistic models employing validated governing equations and verified solution techniques, we have illuminated non-intuitive transport processes that could not have been characterized by experiment alone. In Chapter 2, we described the continuum transport equations used in our crystal growth models, and introduced the numerical methods used for their solution throughout the model domain. And in the following chapters, we described how our attention to details during model design has led to the creation of models that accurately describe the physical processes of various crystal growth systems they are meant to represent.

In Chapter 3, we presented our work on building a more realistic model of a vertical Bridgman system by coupling two disparate computer codes, one which modeled the furnace and the other which modeled the growing crystal domain. The codes were coupled through heat transfer boundary conditions along a shared boundary position. We also have presented results for simulations of heat, momentum and solute transport using such a transient, coupled model employing CrysMAS and Cats2D and have focused on the analysis of both axial and radial segregation of zinc during the growth of CZT via the EDG process. This model was mathematically verified by comparison with heat transfer, flow, and interface shape predicted by CrysMAS, and very good agreement was demonstrated. Validation of the models ability to describe segregation in real systems was provided by

comparison of predicted Zn composition with PL mapping of a smaller boule grown in a similar EDG system. While the match was not perfect, the segregation model predicted essential characteristics of the segregation pattern and was deemed to faithfully represent the behavior of the experimental system. The most surprising and important result obtained in our analysis was the prediction of very complicated, anomalous segregation patterns in zinc composition that would occur in this EDG growth of CZT. To our knowledge, such complicated patterns have not before been predicted for Bridgman-type melt crystal growth systems.

Our results have demonstrated, for the first time, the potential for Zn composition fields in melt-grown CZT crystals to be strongly non-uniform. This non-classical segregation behavior arises from the very strong influence of convection on mass transfer in the melt, especially flows near the melt-solid interface. Although the influence of quasi-steady, incomplete mixing near the interface has been long known [77, 151, 152], the effect of time-evolving, multi-cellular flow transitions on producing such complexity of segregation patterns during growth has not been theoretically demonstrated before (other than the effect of high-frequency striations produced by oscillating or turbulent flows [186, 187, 188]). Another important factor at play here is the propensity of CZT flows to rearrange themselves as a function of a changing thermal environment. This behavior arises from the relatively large Prandtl number of 0.4 for this material, indicating that the coupling between flow and heat transfer is one to two orders of magnitude greater than for more typical semiconductors [157, 189].

There is evidence of such complicated compositional patterns in CZT growth experiments. Indeed, anomalous segregation of zinc has been reported in [190, 191, 192], and recent segregation measurements of Babentsov *et al.* [148] also exhibit disconcertedly large zinc compositional variations across their grown crystals. One may speculate that others have avoided publication of similar, adverse results showing Zn non-uniformity in growth. Of course, there are other possible causes of compositional non-uniformity than melt flows, chief among them being grain structures that would strongly affect the local diffusion of zinc through the solid. There are also segregation patterns that are not so complicated, such as that shown in Section 3.4.2 here. The explanation is simple: these simpler, classical compositional patterns arise when there are no significant structural changes to the flow during growth. The transient computations presented here demonstrate that the melt phase during CZT growth may exhibit multi-cellular flows that change their structure as a delicate function of changing heat transfer conditions. When this occurs, our computations

have demonstrated that this mechanism will result in anomalous segregation that leads to very non-uniform zinc composition. We believe that this outcome is a factor contributing to the difficulty in obtaining zinc uniformity in many CZT melt growth processes. A thorough understanding of melt flows and their control will be needed to address this issue, and computational modeling can provide the necessary tools.

In Chapter 4, We presented a novel furnace profile for an electrodynamic gradient freeze (EDG) process that promotes macroscopically convex interface shapes during the growth of cadmium zinc telluride (CZT). This bell-curve furnace profile is inspired by heat transfer that gives rise to a moving liquid zone and convex interface during growth by the traveling heater method (THM), particularly the notion of directing heat inward near the solidification interface. Here, we have employed sophisticated, furnace-scale analysis by computing quasi-steady solutions using CrysMAS to further develop these ideas. These computations affirm the ability to redirect heat flows and thereby significantly affect interface shape, even with relatively minor changes in the form of the bell-curve profile.

While prior analyses have suggested heat transfer modifications to achieve convex interface shapes in the context of quasi-steady operation [202, 58], such approaches are static and not able to maintain a convex interface over an entire growth run. Thus, the strategy to dynamically adapt the furnace profile is of particular significance. We have shown that a control equation solved in conjunction with transient simulations allows for the computation of a time-evolving, bell-curve profile that keeps the interface shape very nearly constant at all times. With a sufficiently accurate thermal model, this approach may be employed to generate a series of dynamic set points for the heaters in a suitable multi-zone furnace toward achieving interface shape goals. It is easy to envision the extension of these ideas to attain multiple objectives, such as the simultaneous goals of convex interface shape and constant growth rate. It is also likely that dynamic profiles other than the specific one considered here may be successfully employed. Finally, we comment that a segregation analysis for the transient simulation employing the adaptive bell-curve profile shows minimal radial variations and a Scheil-like axial variation of zinc composition, a situation much more favorable than the anomalous zinc segregation sometimes obtained in classical EDG systems [207].

This strategy represents a significant advance over prior approaches for interface shape modification, such as the pedestal modifications analyzed by Kuppurao et al. [14] and Gasperino et al. [167] and employed by Carcelén et al. [198] and Crocco et al. [199]. Unlike pedestal modification, the bell-curve profile can be applied in a multi-zone furnace

without significant design changes in the heat transfer package and it can be dynamically adapted to control interface shape at all times during growth. In line with recent CZT growth results [198, 199], realizing a convex solidification interface via this adaptive bell-curve furnace profile promises better crystallinity and higher yields than traditional CZT growth techniques.

The results presented in Chapter 5, to the authors' knowledge, is the first to demonstrate the theoretical study of the quenching process of CZT crystal growth in an EDG system. Here we presented three cases of results with different histories of heating power profiles. For the base case (case A), there is no time allowed for the system to achieve the stable growth condition before launching the quenching process by setting powers to zero. Therefore, the growth rate in case A increased rapidly and the solidification occurred from all the region next to crucible wall and the trapped melt island existed in the middle region until complete solidification. However, for case B and C with a longer stable growth condition period, the growth rate increased gradually after initiating the quenching process, from the slow solidification rate associated with single crystal growth to a critical growth rate of 10–20 times larger than the slower crystallization rate, in which one may expect that the interface shape would become unstable and lead to polycrystalline growth. Then the growth rate increased in a similar way to case A due to rapid solidification of trapped melt region. Besides, these results showed the evolution of interface shape and position, namely from convex to concave to enclosed circle, and the occurrence of the trapped melt island in the final stage. Also, the thermal gradient in the solid and heat flux pattern is also highly dependent on the heating history of the system in an EDG growth, especially the initial transient stage with/without a stable growth period before launching the quenching process.

Although the work has focused only on the thermal field and interface shape evolution, we believe this strategy provides some insights on the process. Due to the low heat conductivity of CZT and the generally high heat capacity of semiconducting compounds (45–60 $J/mol \cdot K$ for CZT), such a "thermal shock" of quenching process by turning off the powers is not capable of dramatically change the rate of interface advance immediately, therefore one can expect that such a quenching strategy is not capable of freezing the interface shape. However, a stable growth condition is very sensitive to the redistribution of solute. Consequently, a small excess of Te (3–4 at%) in the CZT melt could be used to produce a constitutional supercooled zone in the melt. The infraction of the criterion of constitutional supercooling by breaking the stable growth condition would allow the in-

terface shape to be sharply visible as presented in[210]. Unfortunately, in this theoretical investigation, we ignored the effects of solute distribution and convection, although we do not expect the convection would play a key role in such a process because of the very small thermal gradient in the melt phase.

In Chapter 6, we presented the numerical simulation of sapphire crystal growth via Heat-Exchanger Method (HEM). Sapphire single crystals are an important substrate for the fabrication of gallium-nitride light-emitting-diodes (LEDs) that emit white light. Theses solid-state devices promise great energy savings over both incandescent and compact fluorescent lighting technologies, and their market is expanding at double-digit growth rates. Key to continuing cost reduction for such LED-based lighting is reducing the cost of sapphire without compromising quality. The heat exchanger method (HEM) represents a possible yield improvement over existing growth technologies (primarily Kyropoulos growth) and is the subject of the study presented here.

Here we have performed quasi-steady state and transient analysis using the commercial code CrysMAS to investigate the effects of furnace geometry and processing parameters on the temperature distribution, convection field, and melt-crystal interface shape during the crystal growth of sapphire in a small-scale heat exchanger method system based on the apparatus in Korea Polytechnic University. First of all, a transient simulation without considering melt convection has been performed to gain a big picture of such a growth process. Growth simulations show that the interface is predominantly convex and that the last-to-freeze growth occurs in upper, outer portion of crucible, which may cause segregation and stress-strain issues. Besides, the thermal gradient in the melt phase decreased both axially and radically as crystal growth, while the gradient of temperature in the crystal increased in such growth conditions. Besides, a series of quasi-steady-state simulations have been performed to assess the effects of melt convection including both buoyancy and Marangoni flow on the interface shape and thermal gradient in the melt. The temperature profile in the system is calculated to have lower temperatures both at the base of crucible and at the center top of the melt; however, the presence of convection flow arising from Marangoni force and buoyancy can ameliorate the latter effect. And it turned out the Marangoni effects will strengthen the melt flow, especially during the initial stage, and flatten the interface and reduce the thermal gradient in the melt phase, especially in the region right above the melt/crystal interface. However, it is noticed that the convexity of interface will increase gradually during sapphire growth in spite of the flattening effects of melt convection which intensity decreases as crystal growth.

Furthermore, a comparison study has also been performed to probe the effects of internal radiation by assuming sapphire crystal to be transparent and opaque respectively. Growth simulation results revealed that more convex interface shape occurred due to strengthened radiative cooling by assuming transparent crystal, compared to the much flatter interface shape where the sapphire crystal is assumed to be opaque. By applying simulation model based on CrysMAS, effects of growth conditions and furnace geometry were also investigated, such as growth rate and geometry of crucible support. Simulation results demonstrate that larger growth rate leads to less convex interface due to the coupling of latent heat release and radiative cooling. And molybdenum support geometry can significantly affect the shape of the interface. The larger support diameter leads to much flatter interface and the solidification is more uni-direction. The longer Mo "neck" would flatten interface shape. All of these investigations will provide valuable guidance for further optimization of HEM system.

7.2 Directions for Future Research

The work presented here has advanced the fundamental understandings of melt crystal growth via modeling of CZT growth in EDG furnace and developing a dynamic control strategy to achieve and maintain a convex interface shape. Furthermore, we developed a one-way coupling strategy to do the segregation analysis by performing a transient simulation. Undoubtedly, further questions and opportunities naturally arise from the work presented here. In this section, several future research directions will be highlighted and shortly discussed.

7.2.1 Development of time-dependent, multi-scale, fully-coupled and self-consistent model

Naturally, the next step is to develop a fully-coupled, self-consistent, multi-scale transient model, which will provide the capability of performing more realistic and rigorous transient simulations for melt crystal growth. One ongoing work regarding coupling code is to further develop and apply the Approximate Block Newton method (ABN), which has the capability of performing transient calculations embedded within its structure [5, 171].

The other promising strategy for solving transient problems of coupled systems is presented by Matthies and Steindorf [232], where an excellent outline of both explicit and

implicit time-stepping algorithms have been formulated. There are advantages and disadvantages with both methods. Explicit coupling is easier to implement and the subsystems can be solved independently, but subjected to a critical time step. On the contrary, implicit coupling does not have a critical time step. Furthermore, it is more robust in that the results obtained are the same if the problem were formulated in a monolithic manner. However, implicit coupling is more difficult to implement. The framework, however, for implicit coupling has been introduced through solving steady-state, multi-scale problems with a approximate block Newton method. Since both subsystems are discretized with respect to space and time, the ABN method can be applied to the time integration equations instead of the steady-state residual equations. Further details can be found in [232, 233].

However, explicit coupling could still be a promising strategy considering the difference of time-scales between global model (furnace scale, CrysMAS) and local model (charges, Cats2D). Felippa et al. [234] give numerous examples of time integration schemes of coupled systems. One interesting idea is that of subcycling in which one subsystem (Cats2D) is integrated in a smaller time step than the other subsystem (CrysMAS). Another possibility is to develop a hybrid explicit/implicit coupling method where the ABN method is used at specific time points, and the subsystems are integrated independently (explicitly) during times between these points [233]. A fully transient, coupled model will provide the powerful capabilities of analyzing the melt crystal growth process in a more realistic and vigorous way, and provide more elegant guidance and insight to the further optimization of existing processes.

Another interesting software package being developed to help create multiphysics simulation codes is called LIME [235, 6], an acronym for Lightweight Integrating Multiphysics Environment for coupling codes, by Sandia National Laboratories recently. Recently, more and more problems of great scientific or engineering interest involve complex systems characterized by numerous and even disparate interconnected components where different physical processes interact in a variety of ways. In order to simulate such systems, each and every involved physical processes are described and simulated by numerical models that evolve important state variables, such as temperature, velocity, concentration. It is called “coupled” when these processes interact with each other, and the governing equations must be solved in such a manner that changes in any state variable are properly reflected in all equation sets that are affected by that variable [235]. If the effect of changes in variable “X” on the evolution of variable “Y” is small, then the coupling is referred to be “weak”. Conversely, the coupling is said to be “strong” if the effect is large. Another important

aspect of coupling is whether the effect is linear or nonlinear. One can imagine that the most challenging problems will be those where the coupling is both strong and nonlinear.

LIME is intended to be especially helpful when separate computer codes already exist to solve different parts of a multiphysics problem, such as our *global model* CrysMAS and *local model* Cats2D as depicted in Figure 7.1. In principle, a single physics code can be written to simulate any coupled multiphysics system, i.e. a single physics code is not restricted to a single-physics [235]. Of interest to LIME is the ability for multiple physics codes to be coupled in order to accurately simulate a multiphysics system. In this case each physics code separately approximates the solution to one or more sets of physics in the overall coupled multiphysics system. Figure 7.2 illustrate the key components of LIME in the context of a generic multiphysics application that has been created using LIME from three individual physics codes. Further details could be found in [6].

With such time-dependent, multi-scale coupled model, we will be able to investigate more realistic, model-based control ideas for melt crystal growth process. Instead of dynamically changing the temperature profile along the shared boundary in one-way coupled model, the controller input signals could be applied directly to the furnace heat powers or set-point temperatures. The multi-scale model may also properly capture the time delay between changes in the applied temperature profiles and the corresponding responses of the growing crystals. One such an example will be the quenching process for molten crystal growth. Through a transient, multi-scale model, we can further probe the process of quenching process in a more realistic and detailed manner.

Although very little, if any, observable data can be obtained from melt crystal growth experiments due to the harsh conditions, such as very high temperature and extremely slow growth rate, many creative methods of obtaining in situ and real-time data have been attempted. For example, Kim, Witt, and Gatos related flow intensity to thermocouple measurements [34]. Batur and co-workers [121] measured interface position by employing a transparent furnace and image processing techniques. Eddy current sensors have been shown to be effective in tracking the melt-crystal interface during vertical Bridgman growth of CZT [236, 237]. All of these endeavors provide a solid basis for the ultimate application of model-based control strategies. For example, the coupled, multi-scale model could be applied as a state observer in melt crystal growth system, where the complex physical behavior occurring within the furnace and crystal can be captured. Limited in situ real-time data could be applied to optimize the model for a more accurate estimate of growth dynamics.

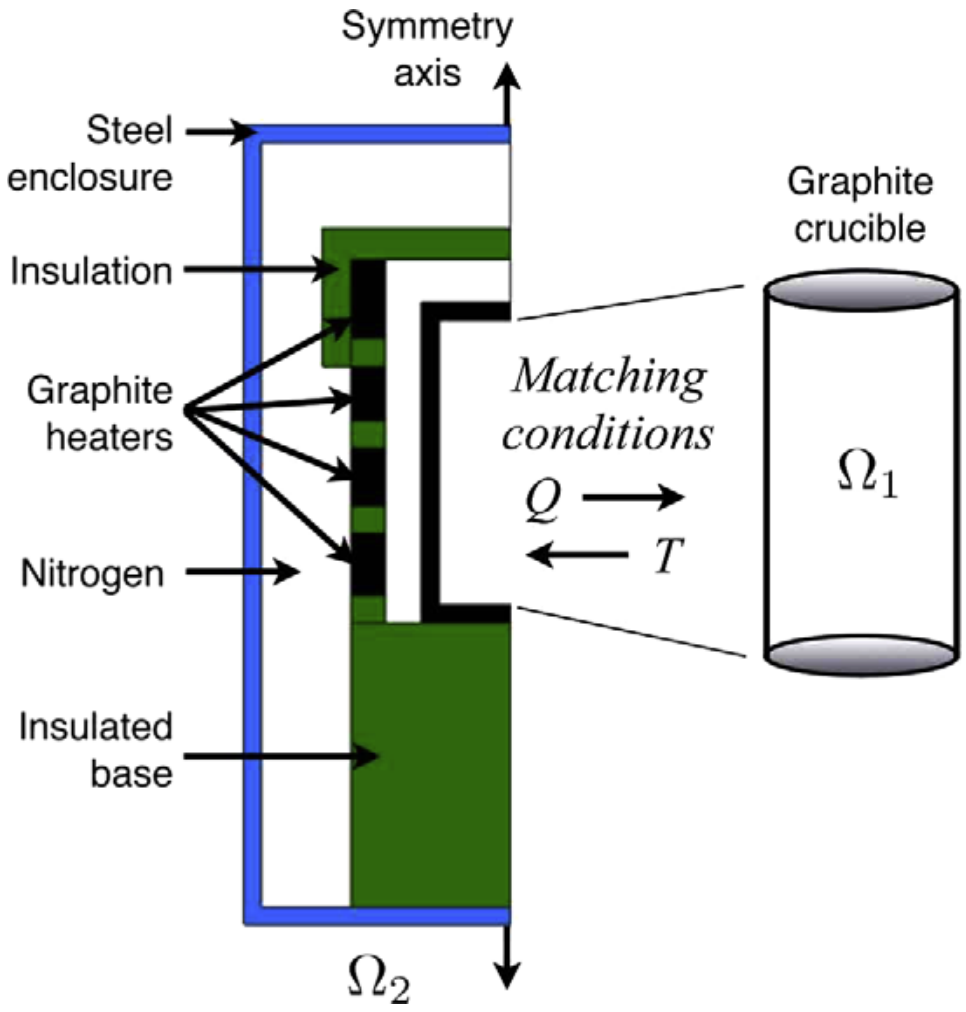

Figure 7.1: Generic simplified schematic of a melt crystal growth furnace, depicting a crystal growth process divided into submodels representing growth chamber (Ω_1) and furnace (Ω_2), which are coupled via conjugate heat transfer conditions. Reprint from [5]

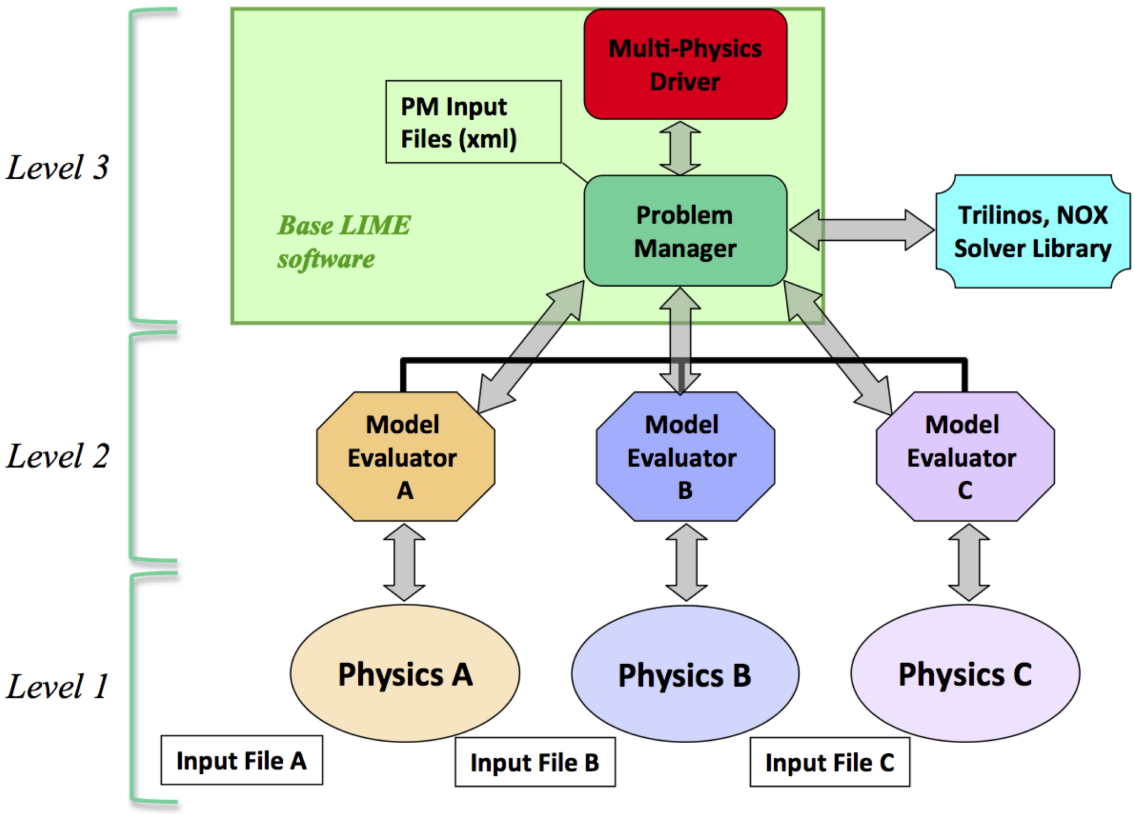

Figure 7.2: Key components of a simple generic application created using LIME. Adapted from [6]

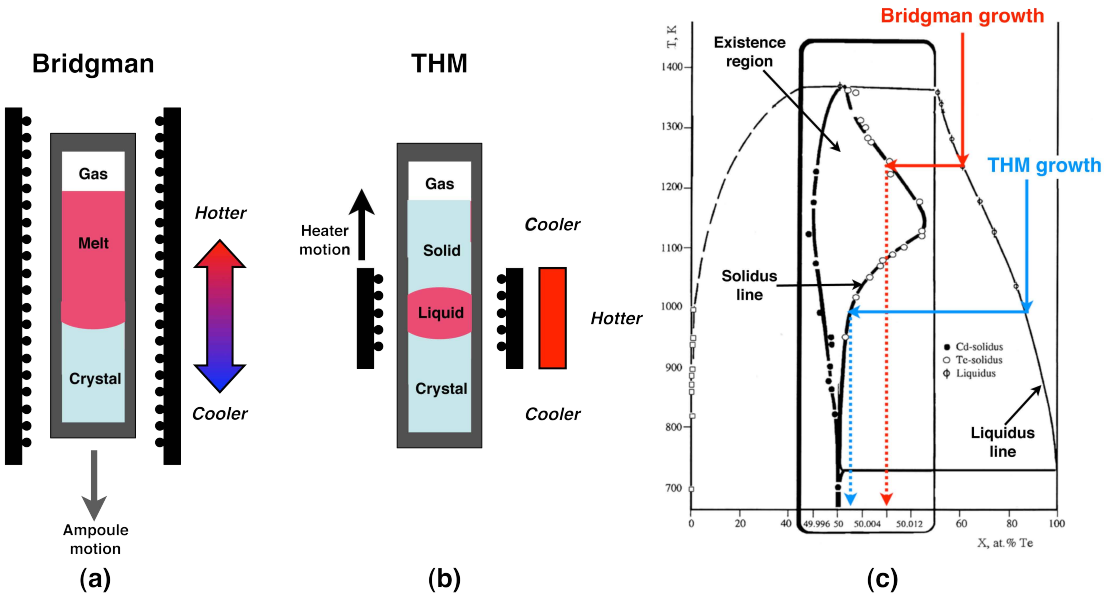

Figure 7.3: Schematic diagram of Bridgman and THM processes for the growth of a compound semiconductor. Phase diagram for CdTe is reproduced from [7]

7.2.2 Analysis of Traveling Heater Method (THM) for improved CZT crystal quality

Most bulk semiconductor crystals grow via directional solidification techniques in which a liquid phase is cooled in a precisely controlled manner to the solid, crystalline phase. The typical technique is the vertical Bridgman crystal growth process, shown schematically in Figure 7.3(a), where an ampoule containing the charge to be solidified is passed from a high-temperature region of a furnace to a lower-temperature region, setting up an appropriate thermal gradient to drive directional solidification. However, the thermodynamic phase behavior of compound semiconductors can impact this growth process in significant ways. One of the most important is the formation of second phases, such as Te-rich particles during the growth of CdTe and its alloys, during growth and cool-down. The traveling heater method (THM), depicted in Figure 7.3(b), is designed to operate in manner that may reduce the amount of second phase produced.

Figure 7.3(c) shows the phase diagram of CdTe (adapted from Greenberg [7]) with paths that mark the operation of each crystal growth process. Let us first focus on the phase diagram itself. A perfectly ordered crystalline array of the compound CdTe can exist only if the

constituent elements Cd and Te are present in exact stoichiometric ratio in the solid. Any deviation from stoichiometry must result in the disorder of atoms. Indeed, at all temperatures above absolute zero, configurational entropic effects (which act to decrease the Gibbs free energy of the solid) will produce non-zero, equilibrium concentrations of vacancies, self-interstitials, and anti-site defects. This leads to an "existence region" in composition of finite extent around the exact stoichiometric compound, over which the crystalline solid exists with an excess of one component or the other at nonzero temperatures. This region is indicated in Figure 7.3(c) and is bounded by the solidus lines of the compound (note also the expanded scale in composition to highlight the existence region). As absolute temperature decreases to zero, the existence region shrinks to a line, and perfect CdTe is the equilibrium solid state. The shrinking of the existence region with decreasing temperature is a generic feature of compound semiconductors and leads to an important phenomenon known as retrograde solubility. Namely, the solubility of the excess component in the solid decreases with temperature, and, upon cooling, there is a thermodynamic driving force for the excess component to form its own, enriched phase.

Next, consider the paths followed by the Bridgman melt growth process and the traveling heater method. Melt growth of CdTe starts with a superheated liquid phase that is typically slightly enriched with tellurium (for radiation detector material). The crucible is moved, leading to a cooling of a volume of the melt; this path is labeled "Bridgman growth" and is colored red in the figure. As this melt volume reaches the liquidus curve (marking its freezing/melting point), solidification occurs, and the melt changes phase to crystalline solid, whose composition is given by the solidus curve in this case CdTe with an excess amount of Te. When this solid eventually cools, following the dotted path on the phase diagram, it leaves the existence region of the phase diagram. The solid will now contain a thermodynamic excess of Te, leading to the nucleation and growth of second-phase particles highly enriched with tellurium.

THM growth follows the blue path in Figure 7.3(c), starting with a strongly tellurium-rich liquid (often referred to as the solvent or flux). As the heater moves upward, a volume of liquid near the lower interface cools to the liquidus point, as in melt growth. However, the freezing temperature of the liquid is much lower than in melt growth because of its high tellurium concentration. Phase change occurs next, and crystalline CdTe forms with a small excess of Te. If the system is engineered to grow from a flux of sufficiently high tellurium concentration, as is the intent in THM growth, the solidus is in retrograde (i.e., the new solid phase forms below the "hump" of the existence region) and, counterintu-

itively, the solid that forms contains far less excess tellurium than that formed during melt growth. Thermodynamics will still provide a driving force to form second-phase, Te- rich particles upon cooling, but we expect there to be be fewer, smaller particles, since there is a comparatively smaller amount of tellurium in the grown solid.

The prior discussion reveals many of the advantages of THM over Bridgman growth. First, THM growth occurs at much lower temperatures, simplifying furnace needs, reducing the gaseous overpressure of cadmium in the sealed crucible, and typically allowing lower thermal gradients (which may lead to lower levels of thermally-generated stresses and dislocations in the grown crystal). Second, since THM growth occurs at a temperature where the solidus curve exhibits retrograde solubility, crystals can be produced with significantly lower levels of excess tellurium and second-phase particles.

There are several additional, practical advantages of THM. It can be operated using pre-compounded ingots, avoiding in-situ, highly exothermic reactions in the growth system. The configuration of the moving liquid results in zone refining of the material; impurities are trapped in the liquid zone. The constant-volume liquid zone also, in theory, can eliminate axial segregation of dopants, a feature especially important for growth with added zinc to produce CZT with homogenous composition.

Unfortunately, despite these advantages, there are several challenges for successful THM growth of CZT. First, accessible growth rates in practice are 10–100 times smaller than those that can be employed in Bridgman growth, typically on the order of mm/day for THM versus several mm/hr for Bridgman. Second, the morphological stability of the growth interface is difficult to maintain during THM.

Owing to the complexity of including phase diagram information, rigorous modeling of the THM is a challenging undertaking. Virtually all previous modeling studies have greatly simplified the problem. Some have concentrated exclusively on the thermal field and have ignored compositional effects. Most have ignored the phase diagram. Others include a simplified version of the phase diagram but ignore interface shape or apply overly simple, unrealistic mass transfer conditions at the interfaces.

The key to the well-posed and realistic problem formulation lies in the representation of both thermodynamic and kinetic effects.

7.2.3 Analysis and Optimization of larger-scale sapphire crystal growth via HEM

Sapphire is an important crystal due to its combination of excellent optical and mechanical properties. The more important requirement of sapphire is to produce larger sizes with higher quality and purity. The most problematic properties of sapphire, with respect to growth, are its anisotropic properties, which necessitated that a completely single crystal boule be grown. Otherwise the boule would undergo cracking during the cooling-down process after growth. Heat-Exchanger Method (HEM) is the only method that has produced very large bulk sapphire crystals due to its unique capabilities of controlling heat input and extraction independently and carrying out in situ annealing of the boule after growth. The configuration of the HEM (see Figure 1.4) insulated heat zone can produce "near isothermal" conditions in the heat zone. During the seeding and growth stage, low concentric temperature gradients are imposed by the heat exchanger by controlling helium flow through the heat exchanger. This allows for crystal growth of high quality, and growth is achieved starting from the melted back seed crystal at the center bottom of the crucible. During the growth stage, the heat exchanger has a localized cooling effect on the charge. After the crystal is grown, it can be in situ annealed to reduce defect density from growth, minimize defect multiplication during cooling-down and allow cooling-down without imposing temperature gradients on the crystal [238].

Up to now, sapphire boules up to 381mm diameter are currently produced routinely using the HEM [239]. The next requirement is to produce sapphire crystals up to 500 mm diameter with higher purity. In order to scale up, the furnace need to be upgraded with respect to control and monitoring systems. And each of the various stages of sapphire growth during HEM, including seeding, charge melting, growth, post-annealing and cooling-down needs to be modified and adjusted in the recipe. Undoubtedly, such a modification and optimization process could be largely accelerated in collaboration with numerical modeling. Therefore, based on our study and results of HEM process in Chapter 6, we could further develop our HEM model to consider the larger crucible size, the more elegant control system and the optimization of the heat-exchanger to obtain the better recipe for such a large-scale sapphire growth. Specifically, we could develop a more realistic and detailed transient model to study the effects of heat-exchanger, to determine the possible flow regime of Helium gas (laminar or turbulent or transitional) and to estimate the overall heat transfer coefficient. On the other hand, through numerical simulations we would design and verify a

more accurate and sensitive control system (more control points, for example) and a more optimized heating system (more heating elements with optimized distribution). By such a combined strategy of design, one will achieve a desirable, dynamic balance between the heat input and extraction to make sure that (i) the solid-liquid interface expands for a three-dimensional growth, (ii) the solid is submerged during most of the growth cycle which will prevent sapphire crystal from mechanical and thermal perturbation by the surrounding melt, and (iii) the last material to solidify is along the walls of the crucible. See the schematics in [240]

Bibliography

[1] H. J. Scheel. Historical aspects of crystal growth technology. Journal of Crystal Growth, 211:1–12, 2000.

[2] Jeffrey J. Derby. Crystal growth: Crystal growth, bulk (theory and models). In F. Bassani, J. Liedl, and P. Wyder, editors, Encyclopedia of Condensed Matter Physics. Academic Press, submitted 2004.

[3] J. J. Derby and A. Yeckel. Modeling of crystal growth. In Georg M uller, Jean-Jacques Métois, and Peter Rudolph, editors, Crystal Growth - From Fundamentals to Technology. Elsevier Science, Amsterdam, 2004.

[4] Minoru Funaki, Tsutomu Ozaki, Kazuyuki Satoh, and Ryoichi Ohno. Growth and characterization of cdte single crystals for radiation detectors. Nuclear Instruments and Methods in Physics Research Section A: Accelerators, Spectrometers, Detectors and Associated Equipment, 436(12):120 – 126, 1999.

[5] Andrew Yeckel, Lisa Lun, and Jeffrey J. Derby. An approximate block newton method for coupled iterations of nonlinear solvers: Theory and conjugate heat transfer applications. J. Computational Physics, 228:8566–8588, 2009.

[6] Rod Schmidt, Noel Belcourt, and Russell Hooperand Roger Pawlowski. An introduction to lime 1.0 and its use in coupling codes for multiphysics simulations. Sandia Technical Report, 2011:8524, 2011.

[7] J.H. Greenberg. Ptx phase equilibrium and vapor pressure scanning of non-stoichiometry in the cdznte system. Progress in Crystal Growth and Characterization of Materials, 47(23):196 – 238, 2003. Vapour Growth of Bulk Crystals and Epitaxy: Part I. Vapour Growth of Bulk Crystals and Epitaxy: Part I.

[8] Bhushan Vartak, Yong-Il Kwon, Andrew Yeckel, and Jeffrey J. Derby. An analysis of flow and mass transfer during the solution growth of potassium titanyl phosphate. Journal of Crystal Growth, 210(4):704 – 718, 2000.

[9] Bhushan Vartak and Jeffrey J. Derby. On stable algorithms and accurate solutions for convection-dominated mass transfer in crystal growth modeling. Journal of Crystal Growth, 230(12):202 – 209, 2001. ¡ce:title¿Proceedings of the Third International Workshop om Modeling in Cr ystal Growth¡/ce:title¿.

[10] Bhushan Vartak, Andrew Yeckel, and Jeffrey J. Derby. Time-dependent, three-dimensional flow and mass transport during solution growth of potassium titanyl phosphate. Journal of Crystal Growth, 281(24):391 – 406, 2005.

[11] Bhushan Vartak, Andrew Yeckel, and Jeffrey J. Derby. On the validity of boundary layer analysis for flow and mass transfer caused by rotation during the solution growth of large, single crystals. Journal of Crystal Growth, 283(34):479 – 489, 2005.

[12] S. Kuppurao, S. Brandon, and J. J. Derby. Modeling the vertical Bridgman growth of cadmium zinc telluride, II: Transient analysis of zinc segregation. J. Cryst. Growth, 155:103–111, 1995.

[13] S. Kuppurao, S. Brandon, and J. J. Derby. Analysis of interrupted growth strategies for cadmium zinc telluride in an unseeded vertical Bridgman system. J. Cryst. Growth, 158:459–479, 1996.

[14] Satheesh Kuppurao and Jeffrey J. Derby. Designing thermal environments to promote convex interface shapes during the vertical Bridgman growth of cadmium zinc telluride. J. Cryst. Growth, 172:350–360, 1997.

[15] Lisa Lun, Andrew Yeckel, Prodromos Daoutidis, and Jeffrey J. Derby. Decreasing lateral segregation in cadmium zinc telluride via ampoule tilting during vertical Bridgman growth. J. Cryst. Growth, 291:348–357, 2006.

[16] Lisa Lun, Andrew Yeckel, Michael Reed, Csaba Szeles, Prodromos Daoutidis, and Jeffrey J. Derby. On the effects of furnace gradients on interface shape during the growth of cadmium zinc telluride in EDG furnaces. J. Cryst. Growth, 290:35–43, 2006.

[17] Lisa Lun, Andrew Yeckel, Jeffrey J. Derby, and Prodromos Daoutidis. Control of interface shape of cadmium zinc telluride grown via an electrodynamic gradient freeze furnace. In Proceedings of IEEE 2007 Mediterranean Conference on Control and Automation (MED '07), Athens, Greece, June 27-29, 2007.

[18] J. C. Brice. Crystal Growth Processes. Halsted Press, 1986.

[19] R. A. Brown. Theory of transport processes in single crystal growth from the melt. AIChE J., 34:881–910, 1988.

[20] D. T. J. Hurle. Crystal Growth of Electronic Materials. Elsevier Science Publishers, 1985.

[21] G. K. Teal, M. Sparks, and E. Buehler. Growth of germanium single crystals containing $p - n$ junctions. Phys. Rev., 81:637, 1951.

[22] R. N. Thomas, H. M. Hobgood, G. W. Eldridge, D. L. Barrett, and T. T. Braggins. Growth and characterization of large diameter undoped semi-insulating GaAs for direct ion implanted FET technology. Solid-State Elect., 24:387–399, 1981.

[23] A. G. Fischer. Techniques for melt-growth of luminescent semiconductor crystals under pressure. J. Electrochem. Soc., 117:41C–47C, 1970.

[24] E. M. Monberg, H. Brown, and C. E. Bonner. Dynamic gradient freeze growth of InP. J. Cryst. Growth, 94:109–114, 1989.

[25] S. Sen, W. H. Konkel, S. J. Tighe, L. G. Bland, S. R. Sharma, and R. E. Taylor. Crystal growth of large-area single-crystal CdTe and CdZnTe by the computer-controlled vertical modified-Bridgman process. J. Cryst. Growth, 86:111–117, 1990.

[26] Satheesh Kuppurao. Analysis of Transport Processes During the Growth of Single Crystal by the Vertical Bridgman Method. PhD thesis, University of Minnesota, 1995.

[27] S. Brandon and Jeffrey J. Derby. Heat transfer in vertical Bridgman growth of oxides: effects of conduction, convection, and internal radiation. Journal of Crystal Growth, 121:473–493, 1992.

[28] Ji. Kvapil, Jo. Kvapil, B. Manek, B. Perner, R. Autrata, and P. Schauer. Czochralski growth of YAG:Ce in a reducing protective atmosphere. Journal of Crystal Growth, 52(Part 2):542 – 545, 1981.

[29] V. S. Yuferev and M. G. Vasil'ev. Heat transfer in shaped thin-walled semi-transparent crystals pulled from the melt. Journal of Crystal Growth, 82(1-2):31 – 38, 1987.

[30] Jeffrey J. Derby. Macroscopic transport processes during the growth of single crystals from the melt. In Science and Technology of Crystal Growth, pages 97–110. Kluwer Academic Publishers, Dordrecht, 1995.

[31] W. W. Mullins and R. F. Sekerka. Stability of a planar interface during solidification of a dilute binary alloy. J. Applied Phys., 35:444–451, 1964.

[32] M. C. Flemings. Solidification Processes. McGraw-Hill, Inc., New York, 1974.

[33] W. A. Tiller. Principles of solidification. In J. J. Gilman, editor, The Art and Science of Growing Crystals, page 276. John Wile & Sons, Inc., 1963.

[34] K. M. Kim, A. F. Witt, and H. C. Gatos. Crystal growth from the melt under destabilizing thermal gradients. J. Electrochem. Soc., 119:1218–1226, 1972.

[35] K. M. Kim, A. F. Witt, M. Lichtensteiger, and H. C. Gatos. Quantitative analysis of the effects of destabilizing vertical thermal gradients on crystal growth and segregation: Ga-doped Ge. J. Electrochem. Soc., 125:475–480, 1978.

[36] T. Jasinski and A. F. Witt. On control of the crystal-melt interface shape during growth in a vertical Bridgman configuration. J. Cryst. Growth, 71:295–304, 19875.

[37] P. Penning. Generation of imperfections in germanium crystals by thermal strain. Philips' Research Reports, 13:79, 1958.

[38] Chong E. Chang and William R. Wilcox. Control of interface shape in the vertical Bridgman-Stockbarger technique. J. of Cryst. Growth, 21:135–140, 1974.

[39] P.M. Adornato and R. A. Brown. Convection and segregation in directional solidification of dilute and non-dilute binary alloys: Effects of ampoule and furnace design. J. Cryst. Growth, 80:155–190, 1987.

[40] S. Brandon and J.J. Derby. Heat transfer in vertical Bridgman growth of oxides: Effects of conduction, convection, and internal radiation. J. Cryst. Growth, 121:473–494, 1992.

[41] Lih-Yen Chin and Frederick M. Carlson. Finite element analysis of the control of interface shape in Bridgman crystal growth. J. Cryst. Growth, 62:561–567, 1983.

[42] P. S. Dutta, K. S. Sangunni, H. L. Bhat, and Vikram Kumar. Growth of gallium antimonide by vertical Bridgman technique with planar crystal-melt interface. J. Cryst. Growth, 141:44–50, 1994.

[43] P. S. Dutta, H. L. Bhat, and Vikram Kumar. Numerical analysis of melt-solid interface shapes and growth rates of gallium antimonide in a single-zone vertical Bridgman furnace. J. Cryst. Growth, 154:213–222, 1995.

[44] Tai-Wei Fu and William R. Wilcox. Influence of insulation on stability of interface shape and position in the vertical Bridgman-Stockbarger technique. J. Cryst. Growth, 48:416–424, 1980.

[45] R. J. Naumann and S. L. Lehoczky. Effect of variable thermal conductivity on isotherms in Bridgman growth. J. Cryst. Growth, 61:707–710, 1983.

[46] Sanghamitra Sen and William R. Wilcox. Influence of crucible on interface shape, position and sensitivity in the vertical Bridgman-Stockbarger technique. J. Cryst. Growth, 28:26–40, 1975.

[47] N. K. Udayashankar, K. Gopalakrishna Naik, and H. L. Bhat. The influence of temperature gradient and lowering speed on the melt-solid interface shape of $Ga_xIn_{1-x}Sb$ alloy crystals grown by vertical Bridgman technique. J. Cryst. Growth, 203:333–339, 1999.

[48] C. A. Wang, A. F. Witt, and J. R. Carruthers. Analysis of crystal growth characteristics in a conventional vertical Bridgman configuration. J. Cryst. Growth, 66:299–308, 1984.

[49] Andrew Yeckel and Jeffrey J. Derby. Feasibility study of cadmium zinc telluride growth using submerged heater in a vertical Bridgman system. J. Electron. Mater., 33:488–497, 2004.

[50] C. G. M. Marangoni. Sul pincipio della viscosità superficiale dei liquidi stabilitio dal Signor J. Plateau (on the principle of surface viscosity of liquids by Mr. J. Plateau). Il Nuovo Cimento, Ser. 2, 5/6:239–273, 1871.

[51] J. Baumgartl, W. Budweisr, G. Müller, and G. Neumann. Studies of buoyancy driven convection in a vertical cylinder with parabolic temperature profile. J. Cryst. Growth, 97:9–17, 1989.

[52] G. Müller, G. Neumann, and W. Weber. Natural convection in vertical Bridgman configuration. J. Cryst. Growth, 70:78–93, 1984.

[53] G. Müller, G. Neumann, and H. Matz. A two-Rayleigh-number model of buoyancy-driven convection in vertical melt growth configurations. J. Cryst. Growth, 84:36–49, 1987.

[54] G. Müller. Convective instabilities in melt growth configurations. J. Cryst. Growth, 128:26–36, 1993.

[55] C. W. Lan. Effects of ampoule rotation on flows and dopant segregation in vertical Bridgman crystal growth. J. Cryst. Growth, 197:983–991, 1999.

[56] C. W. Lan, M. C. Liang, and J. H. Chian. Influence of ampoule rotation on three-dimensional convection and segregation in Bridgman crystal growth under imperfect growth conditions. J. Cryst. Growth, 212:340–351, 2000.

[57] Qiang Xiao, Satheesh Kuppurao, Andrew Yeckel, and Jeffrey J. Derby. On the effects of ampoule tilting during vertical Bridgman growth: three-dimensional computations via a massively parallel, finite element method. J. Cryst. Growth, 167:292–304, 1996.

[58] Andrew Yeckel, Geoffrey Compére, Arun Pandy, and Jeffrey J. Derby. Three dimensional imperfections in a model vertical Bridgman growth system for cadmium zinc telluride. J. Cryst. Growth, 263:629–644, 2004.

[59] D. H. Kim, P. M. Adornato, and R. A. Brown. Effect of vertical magnetic field on convection and segregation in vertical Bridgman crystal growth. J. Cryst. Growth, 89:339–356, 1988.

[60] C. W. Lan, I. F. Lee, and B. C. Yeh. Three-dimensional analysis of flow and segregation in vertical Bridgman crystal growth under axial and transversal magnetic fields. J. Cryst. Growth, 254:503–515, 2003.

[61] J. R. Carruthers. Crystal growth in a low gravity environment. J. Cryst. Growth, 263:629–644, 2004.

[62] P. Capper, J. C. Brice, C. L. Jones, J. J. G. Gosney, C. K. Ard, I. Kenworthy, and A. Clark. Interfaces and flow regimes in ACRT grown $Cd_xHg_{1_x}Te$ crystals. J. Cryst. Growth, 89:171–176, 1988.

[63] A. Horowitz, D. Gazit, J. Makovsky, and L. Ben-Dor. Bridgman growth of Rb_2MnCl_4. J. Cryst. Growth, 61:317–322, 1983.

[64] Andrew Yeckel and Jeffrey J. Derby. Effect of accelerated crucible rotation on melt composition in high-pressure vertical Bridgman growth of cadmium zinc telluride. J. Cryst. Growth, 209:734–750, 2000.

[65] Andrew Yeckel, F. Patrick Doty, and Jeffrey J. Derby. Effect of steady crucible rotation on segregation in high-pressure vertical Bridgman growth of cadmium zinc telluride. J. Cryst. Growth, 203:87–102, 1999.

[66] W. A. Tiller, K. A. Jackson, J. W. Rutter, and B. Chalmers. The redistribution of solute atoms during the solidification of metals. Acta Metallurgica, 1:428, 1953.

[67] W. A. Tiller. Principles of solidification. In J. J. Gilman, editor, The Art and Science of Growing Crystals, page 276. John Wiley & Sons, Inc., New York, 1963.

[68] J. A. Burton, R. C. Prim, and W. P. Schlicter. The distribution of solute in crystals grown from the melt: Theoretical. J. Chem. Phys., 21:1987–1991, 1953.

[69] Chuechun J. Chang and Robert A. Brown. Radial segregation induced by natural convection and melt/solid interface shape in vertical Bridgman growth. J. Crystal Growth, 63:343–364, 1983.

[70] Merton C. Flemings. Solidification Processes. McGraw-Hill, Inc., New York, 1974.

[71] R. F. Sekerka. Morphological stability. In P. Hartman, editor, Crystal Growth: An Introduction, pages 403–443. American Elsevier Publishing Company, Inc., New York, 1973.

[72] W. W. Mullins and R. F. Sekerka. Stability of a planar interface during solidification of a dilute binary alloy. Journal of Applied Physics, 35:444, 1964.

[73] D. T. J. Hurle. Melt growth. In P. Hartman, editor, Crystal growth: an introduction, pages 210–247. American Elsevier Publishing Company, Inc., New York, 1973.

[74] Chong E. Chang and William R. Wilcox. Control of interface shape in the vertical Bridgman-Stockbarger technique. Journal of Crystal Growth, 21:135–140, 1974.

[75] James Coble Brice. Crystal Growth Processes. Halsted Press, New York, 1986.

[76] P. Penning. Generation of imperfections in germanium crystals by thermal strain. Philips' Research Reports, 13:79, 1958.

[77] Robert A. Brown. Theory of transport processes in single crystal growth from the melt. AIChE Journal, 34(6):881–910, 1988.

[78] D. T. J. Hurle, E. Jakeman, and E. R. Pikeman. Striated solute distributions produced by temperature oscillations during crystal growth from the melt. Journal of Crystal Growth, 3:633–640, 1968.

[79] K. M. Kim, A. F. Witt, and H. C. Gatos. Crystal growth from the melt under destabilizing thermal gradients. J. Electrochem. Soc., pages 1218–1226, 1972.

[80] K. M. Kim, A. F. Witt, M. Lichtensteiger, and H. C. Gatos. Quantitative analysis of the effects of destabilizing vertical thermal gradients on crystal growth and segregation: Ga-doped Ge. J. Electrochem. Soc., 125:475–480, 1978.

[81] Peter Rudolph and Manfre Mühlberg. Basic problems of vertical Bridgman growth of CdTe. Mater. Sci. Eng. B, 16:8–16, 1993.

[82] R. B. James, T. E. Schlesinger, J. C. Lund, and Michael Schieber. $Cd_{1-x}Zn_xTe$ spectrometers for gamma and X-ray applications. In T. E. Schlesinger an R. B. James, editor, Semiconductors for Room Temperature Nuclear Detector Applications, volume 43 of Semiconductors and Semimetals, pages 335–381. Academic Press Inc, San Diego, CA, 1995.

[83] A. Yeckel and J. J. Derby. Computer modelling of bulk crystal growth. In P Capper, editor, Bulk Crystal Growth of Electronic, Optical, and Optoelectronic Materials, pages 73–119. John Wiley & Sons, West Sussex, UK, 2005.

[84] Bing Dai. Finite element modeling solution crystal growth at a meso-scale. PhD thesis, University of Minnesota, 2005.

[85] Yong-Il Kwon and Jeffrey J. Derby. Modeling the coupled effects of interfacial and bulk phenomena during solution crystal growth. J. Cryst. Growth, 230:328–335, 2001.

[86] W. A. Tiller. The Science of Crystallization: Microscopic Interfacial Phenomena. Cambridge University Press, New York, 1991.

[87] H. Emmerich. The Diffuse Interface Approach in Materials Science: Thermodynamic Concepts and Applications of Phase-Field Models. Springer-Verlag, Heidelberg, 2003.

[88] W. A. Tiller, K. A. Jackson, J. W. Rutter, and B. Chalmers. The redistribution of solute atoms during the solidification of metals. Acta Metallurgica, 1:428, 1953.

[89] V. G. Smith, W. A. Tiller, and J. W. Rutter. A mathematical analysis of solute redistribution during solidification. Canadian J. Phys., 33:723–745, 1955.

[90] E. Scheil. Bemerkungen zür schichtkristallbildung. Z. Metall., 34:70–72, 1942.

[91] J. A. Burton, R. C. Prim, and W. P. Schlicter. The distributions of solute in crystals grown from the melt: theoretical. J. Chem. Phys, 21:1987–1991, 1953.

[92] W. Nernst. Theorie des Reaktiongeschwindigkeit in heterogenen systemen (theory of reaction velocities in heterogeneous systems). Z. Phys. Chem., 47:52–55, 1904.

[93] S. R. Coriell and R. F. Sekerka. Lateral solute segregation during unidirectional solidification of a binary alloy with a curved solid-liquid interface. J. Cryst. Growth, 46:479–482, 1979.

[94] S. R. Coriell and R. F. Sekerka. Lateral solute segregation during unidirectional solidification of a binary alloy with a curved solid-liquid interface, II. large departures from planarity. J. Cryst. Growth, 54:167–175, 1981.

[95] W. R. Wilcox. Validity of the stagnant film approximation for mass transfer in crystal growth and dissolution. Mat. Res. Bull., 4:265–274, 1969.

[96] F. Rosenberger and G. Müller. Interfacial transport in crystal growth, a parametric comparison of convective effects. J. Cryst. Growth, 65:91–104, 1983.

[97] R. A. Brown and D. H. Kim. Modeling of directional solidification: from Scheil to detailed numerical simulation. J. Cryst. Growth, 109:50–65, 1991.

[98] C. J. Chang and R. A. Brown. Radial segregation induced by natural convection and melt/solid interface shape in vertical Bridgman growth. J. Cryst. Growth, 63(343-364), 1983.

[99] K. Edwards and J. J. Derby. Understanding horizontal Bridgman shelf growth of cadmium telluride and cadmium zinc telluride I. heat and mass transfer. J. Cryst. Growth, 179:120–132, 1997.

[100] K. Edwards and J. J. Derby. Understanding horizontal Bridgman shelf growth of cadmium telluride and cadmium zinc telluride II. thermoelastic stresses. J. Cryst. Growth, 179:133–143, 1997.

[101] D. H. Kim and R. A. Brown. Modelling of the dynamics of HgCdTe growth by the vertical Bridgman method. J. Cryst. Growth, 114:441–434, 1991.

[102] S. Kuppurao, S. Brandon, and J. J. Derby. Modeling the vertical Bridgman growth of cadmium zinc telluride, I.: Quasi-steady analysis of heat transfer and convection. J. Cryst. Growth, 155:93–102, 1995.

[103] I. Lakeenkov, V. B. Ufimtsev, N. I. Shmatov, and Yu. F. Schelkin. Numerical simulation of vertical Bridgman growth of $Cd_{1-x}Zn_xTe$ melts. J. Cryst. Growth, 197:443–448, 1999.

[104] C. Martinez-Tomas, V. Muñoz, and R. Triboulet. Heat transfer simulation in a vertical Bridgman CdTe growth configuration. J. Cryst. Growth, 197:435–442, 1999.

[105] G. Müller. Modeling of crystal growth from the melt. In P. Vincenzini and A. Lami, editors, Computational Modelling and Simulations of Materials, pages 267–278. Techna Srl., 2003.

[106] C. W. Lan. Recent progress of crystal growth modeling and growth control. Chem. Eng. Sci., 59:1437–1457, 2004.

[107] E. Billig. Some defects in crystals grown from the melt. I. defects caused by thermal stresses. Proc. Roy. Soc. London, Ser. A, Math. Phys. Sci., 235:37–55, 1956.

[108] A. S. Jordan, A. R. Von Neida, and J. W. Nielsen. A comparative study of thermal stress induced dislocation generation in pulled GaAs, InP, and Si crystals. J. Appl. Phys., 52:3331–3336, 1981.

[109] O. W. Dillon Jr., C. T. Tsai, and R. J. DeAngelis. Dislocation dynamics during of web type silicon ribbon. J. Cryst. Growth, 82:50–59, 1987.

[110] M. Kurz, A. Pusztai, and G. Müller. Development of a new powerful computer code CrysVUN++ especially designed for fast simulation of bulk crystal growth processes. J. Cryst. Growth, 198/199:101–106, 1999.

[111] F. Dupret, P. Nicodème, Y. Ryckmans, P. Wouters, and M. J. Crochet. Global modelling of heat transfer in crystal growth furnaces. Int. J. Heat Mass Transfer, 33:1849–1871, 1990.

[112] H. Ouyang and W. Shyy. Multi-zone simulation of the Bridgman growth process of β-NiAl crystal. Int. J. Heat Mass Transfer, 39(10):2039–2051, 1996.

[113] E. V. Yakovlev, V. V. Kalaev, I. Yu. Evstratov, Ch. Frank-Rotsch, M. Neubert, P. Rudolph, and Yu. N. Makarov. Global heat and mass transfer in vapor pressure controlled Czochralski growth of GaAs crystals. J. Cryst. Growth, 252:26–36, 2003.

[114] A. Pandy, A. Yeckel, M. Reed, C. Szeles, M. Hainke, G. Müller, and J. J. Derby. Analysis of the growth of cadmium zinc telluride in an electrodynamic gradient freeze furnace via a self-consistent, multi-scale numerical model. J. Cryst. Growth, 276:133–147, 2005.

[115] A. Yeckel, A. Pandy, and J.J. Derby. Fixed-point convergence of modular, steady-state heat transfer models coupling multiple scales and phenomena for melt-crystal growth. Int. J. Numer. Methods Eng., 67:1768–1789, 2006.

[116] Jeffrey J. Derby, Lisa Lun, and Andrew Yeckel. Strategies for the coupling of global and local crystal growth models. J. Cryst. Growth, 303:114–123, 2007.

[117] R. G. Seidensticker, W. R. Rosch, R. Mazelsky, R. H. Hopkins, N. B. Singh, S. R. Coriell, W. M. B. Duval, and C. Batur. Active control of interface shape during the crystal growth of lead bromide. J. Cryst. Growth, 198/199:988–994, 1999.

[118] Y. Azuma, N. Usami, T. Ujihara, K. Fujiwara, G. Sazaki, Y. Murakami, and K. Nakajima. Growth of SiGe bulk crystals with uniform composition by utilizing feedback control system of the crystal-melt interface position for precise control of the growth temperature. J. Cryst. Growth, 250:298–304, 2003.

[119] Paul Sonda, Andrew Yeckel, Prodromos Daoutidis, and Jeffrey J. Derby. Development of model-based control for bridgman crystal growth. J. Cryst. Growth, 266:182–189, 2004.

[120] Paul Sonda, Andrew Yeckel, Jeffrey J. Derby, and Prodromos Daoutidis. The feedback control of the vertical bridgman crystal growth process by crucible rotation: Two case studies. Comput. Chem. Eng., 29:882–896, 2005.

[121] Celal Batur, Arvind Srinivasan, Walter M.B. Duval, N.B. Singh, and D. Golovaty. On-line control of solid-liquid interface by state feedback. J. Cryst. Growth, 205:395–409, 1999.

[122] C. Batur, W. Duval, and R. Bennett. Performance of Bridgman furnace operating under projective control. In Proceedings of the American Control Conference, pages 4101–4105, 1999.

[123] Arvind Srinivasan, Celal Batur, Bruce N. Rosenthal, and Walter M.B. Duval. Solid-liquid interface shape control during crystal growth. In Proceedings of the American Control Conference, volume 2, pages 1270–1274, 1995.

[124] Andrew Yeckel and Ralph T. Goodwin. Cats2D (Crystallization and Transport Simulator), User Manual, 2003. `http://www.msi.umn.edu/~yeckel/cats2d.html`.

[125] R. B. Bird, W. E. Stewart, and E. N. Lightfoot. Transport Phenomena. John Wiley & Sons, 1960.

[126] Thomas J. R. Hughes. The Finite Element Method: Linear Static and Dynamic Finite Element Analysis. Prentice-Hall, Inc., Englewood Cliffs, New Jersey, 1987.

[127] P. M. Gresho and R. L. Sani. Incompressible Flow and the Finite Element Method, Vol. 2: Isothermal Laminar Flow. John Wiley % Sons Ltd., New York, 1998.

[128] B. A. Finlayson and L. E. Scriven. The method of weighted residuals and its relation to certain variational principles for the analysis of transport processes. Chem. Eng. Sci., 20:395–404, 1965.

[129] Alan Jeffrey. Handbook of Mathematical Formulas and Integrals. Academic Press, New York, 1995.

[130] A. Winslow. Adaptive mesh zoning by the equipotential method. Technical Report UCID-190602, Lawrence Livermore National Laboratory, 1981.

[131] K. N. Christodoulou and L. E. Scriven. Discretization of free surface flows and other moving boundary problems. J. Comput. Phys., 99:39–55, 1992.

[132] Juan de Santos. Two-Phase CoCurrent Downflow Through Constricted Passages. PhD thesis, University of Minnesota, 1991.

[133] P. Hood. Frontal solution program for unsymmetric matrices. Int. J. Numer. Methods Eng., 10:379–399, 1976.

[134] P. M. Gresho. Some interesting issues in incompressible fluid dynamics, both in the continuum and in numerical simulation. In Advances in Applied Mechanics. Academic Press, 1992.

[135] M. Kurz and G. Müller. Control of thermal conditions during crystal growth by inverse modeling. Journal of Crystal Growth, 208(1–4):341–349, 2000.

[136] M. Kurz, A. Pusztai, and G. Müller. Development of a new powerful computer code CrysVUn++ especially designed for fast simulation of bulk crystal growth processes. Journal of Crystal Growth, 198–199(Part-1):101–106, 1999.

[137] J. Fainberg, D. Vizman, J. Friedrich, and G. Müller. A new hybrid method for the global modeling of convection in cz crystal growth congurations. Journal of Crystal Growth, 303(1):124–134, 2007.

[138] David Joseph Gasperino. Modeling of Transport Processes during Solution, Melt and Colloidal Crystal Growth. PhD thesis, University of Minnesota, 2008.

[139] R. Triboulet, Y. Marfaing, A. Cornet, and P. Siffert. Undoped high-resistivity cadmium telluride for nuclear radiation detectors,convection. J. Appl. Phys., 45:2759–2765, 1974.

[140] J.F. Butler, C.L. Lingren, and F.P. Doty. $Cd_{1-x}Zn_xTe$ gamma ray detectors. IEEE Trans. Nucl. Sci., 39:605–609, 1992.

[141] J.F. Butler, B. Apotovsky, A. Niemela, and H. Sipila. Sub-kev resolution detection with $Cd_{1-x}Zn_xTe$ detectors. In Proceedings of SPIE-The International Society for Optical Engineering, vol. 2009, SPIE, pages 121–127, Bellingham, WA, 1993.

[142] R.B. James and P. Siffert. Room temperature semiconductor detectors. In Proceedings of the 11th International Wrkshop on Room Temperature Semiconductor X- and Gamma-ray Detectors and Associated Electronics, Nucl. Instrum. Methods A, page 458, 2001.

[143] R.B. James, T.E. Schlesinger, J.C. Lund, and M. Schieber. spectrometers for Gamma and X-ray applications, in: T.E.S., R.B. James (Eds.). Academic Press Inc., San Diego, CA, 1995, pp. 335–381.

[144] P. Rudolph. Fundamental studies on bridgman growth of CdTe. Progress in Crystal Growth and Characterization of Materials, 29:275–381, 1994.

[145] P. Rudolph. Melt growth of IIVI compound single crystals. In M. Isshiki (Ed.), Recent Development of Bulk Crystal Growth, Research Signpost, Trivandrum, India, 1998.

[146] R. Triboulet. Wiley Press Inc., New York, 2003, pp. 373–406.

[147] R. Triboulet. Fundamentals of the CdTe and CdZnTe bulk growth. Phys, Status Solidi, C 2:1556–1565, 2005.

[148] V. Babentsov, J. Franc, A. Fauler, M. Fiederle, and R.B. James. Distribution of zinc, resistivity, and photosensitivity in a vertical bridgman grown $Cd_{1-x}Zn_xTe$ ingot. J. Crystal Growth, 310:3482–3487, 2008.

[149] E. Scheil. Bemerkungen zur schichtkristallbildung. Z. Metallk, 34:70–72, 1942.

[150] V.G. Smith, W.A. Tiller, and J.W. Rutter. A mathematical analysis of solute redistribution during solidification. Can. J. Phys., 33:723, 1955.

[151] G. Müller and A. Ostrogorsky. Convection in melt growth. In D. T. J. Hurle, editor, Handbook of Crystal Growth Vol. 2b: Bulk Crystal Growth, Growth Mechanisms and Dynamics, pages 711–814. North-Holland, Amsterdam, 1994.

[152] J.J. Derby. Modeling and bulk crystal growth processes: What is to be learned? In M. Wang, K. Tsukamoto, and D. Wu, editors, Selected Topics on Crystal Growth: 14th International Summer School on Crystal Growth, AIP Conference Proceedings 1270, pages 221–246, Melville, New York, 2010.

[153] S. Sen, W. H. Konkel, S. J. Tighe, L. G. Bland, S. R. Sharma, and R. E. Taylor. Crystal growth of large-area single-crystal CdTe and CdZnTe by the computer-controlled vertical modified-Bridgman process. Journal of Crystal Growth, 86:111–117, 1988.

[154] M. Pfeiffer and M. Mühlberg. Interface shape observation and calculation in crystal growth of CdTe by the vertical bridgman method. Journal of Crystal Growth, 118:269–276, 1991.

[155] C. Parfeniuk, F.Weinberg, I. V. Samarasekera, C. Schvezov, and L. Li. Measured critical resolved shear stress and calculated temperature and stress fields during growth of CdZnTe. Journal of Crystal Growth, 119:261–270, 1992.

[156] Satheesh Kuppurao and Jeffrey J. Derby. Designing thermal environments to promote convex interface shapes during vertical Bridgman growth of cadmium zinc telluride. Journal of Crystal Growth, 172:350–360, 1997.

[157] Satheesh Kuppurao, Simon Brandon, and Jeffrey J. Derby. Modeling the vertical Bridgman growth of cadmium zinc telluride, I: Quasi-steady analysis of heat transfer and convection. Journal of Crystal Growth, 155:93–102, 1995.

[158] Satheesh Kuppurao, Simon Brandon, and Jeffrey J. Derby. Modeling the vertical Bridgman growth of cadmium zinc telluride, II: Transient analysis of zinc segregation. Journal of Crystal Growth, 155:103–111, 1995.

[159] Satheesh Kuppurao, Simon Brandon, and Jeffrey J. Derby. Analysis of interrupted growth strategies for cadmium telluride in an unseeded vertical Bridgman system. Journal of Crystal Growth, 158:459–470, 1996.

[160] Krisanne Edwards, Simon Brandon, and Jeffrey J. Derby. Transient effects during the horizontal Bridgman growth of cadmium zinc telluride. Journal of Crystal Growth, 206:37–50, 1999.

[161] Krisanne Edwards and Jeffrey J. Derby. Understanding horizontal Bridgman shelf growth of cadmium zinc telluride, I: Heat and momentum transfer. Journal of Crystal Growth, 179:120–132, 1997.

[162] Krisanne Edwards and Jeffrey J. Derby. Understanding horizontal Bridgman shelf growth of cadmium zinc telluride, II: Thermoelastic stresses. Journal of Crystal Growth, 179:133–143, 1997.

[163] Qiang Xiao, Satheesh Kuppurao, Andrew Yeckel, and Jeffrey J. Derby. On the effects of ampoule tilting during vertical bridgman growth: Three-dimensional computations via a massively parallel, finite element method. Journal of Crystal Growth, 167:292–304, 1996.

[164] Andrew Yeckel and Jeffrey J. Derby. Effect of accelerated crucible rotation on melt composition in high-pressure vertical Bridgman growth of cadmium zinc telluride. Journal of Crystal Growth, 209:734–750, 2000.

[165] Andrew Yeckel, F. Patrick Doty, and Jeffrey J. Derby. Effect of steady crucible rotation on segregation in high-pressure vertical Bridgman growth of cadmium zinc telluride. Journal of Crystal Growth, 203:87–102, 1999.

[166] L. Lun, A. Yeckel, P. Daoutidis, and J. J. Derby. Decreasing lateral segregation in Cadmium Zinc Telluride via ampoule tilting during vertical Bridgman crystal growth. Journal of Crystal Growth, 291:348–357, 2006.

[167] David Gasperino, Mary Bliss, Kelly Jones, Kelvin Lynn, and Jeffrey J. Derby. On crucible effects during the growth of cadmium zinc telluride in an electrodynamic gradient freeze furnace. J. Crystal Growth, 311:2327–2335, 2009.

[168] Andrew Yeckel and Ralph T. Goodwin. Cats2D: Crystallization and Transport Simulator, User Manual. Available at http://www.msi.umn.edu/ yekcel/cats2d.html, 2003.

[169] A. Pandy, A. Yeckel, M. Reed, C. Szeles, M. Hainke, G. Müller, and J. J. Derby. Analysis of the growth of cadmium zinc telluride in an electrodynamic gradient freeze furnace via a self-consistent, multi-scale numerical model. Journal of Crystal Growth, 276:133–147, 2005.

[170] L. Lun, A. Yeckel, M. Reed, C. Szeles, P. Daoutidis, and J. J. Derby. On the effects of furnace gradients on interface shape during the growth of cadmium zinc telluride in EDG furnaces. Journal of Crystal Growth, 290:35–43, 2006.

[171] Andrew Yeckel, Lisa Lun, and Jeffrey J. Derby. Multi-scale crystal growth computations via an approximate block newton method. J. Crystal Growth, 312:1463–1467, 2010.

[172] L. Shcherbak, O. Kopach, Y. Plevachuk, V. Sklyarchuk, C. Dong, and P. Siffert. The viscosity of liquid cadmium telluride. Journal of Crystal Growth, 212:385–390, 2000.

[173] K. M. Arefev, B. F. Remarchuk, and M. A. Guseva. Diffusion in metal vapors in gases and the transport properties of vapors. Inzhenerno-Fizicheskii Zhurnal, 42:930–937, 1982.

[174] M. A. Ceramics. Technical data sheet: Pyrolytic boron nitride (a-pbn). Technical report, 2006. The Morgan Crucible Company.

[175] Toby David Rule. Experimental Validation of (Cd,Zn)Te Crystal Growth Model. PhD thesis, Washington State University, 2002.

[176] R. P. Inc. Vibratable product data: Vibrocast 60pc. Technical report, 2006. Resco Products Inc.

[177] M. A. Ceramics. Boards and shapes: Molded min-k insulation. Technical report, 2006. The Morgan Crucible Company.

[178] Y. S. Touloukian. Thermophysical Properties of Matter. IFI/Plenum, New York, 1979.

[179] K. Zanio. Cadmium telluride, volume 13 of Semiconductors and Semimetals. Academic Press, New York, 1978.

[180] K. Schwenkenbecher and P. Rudolph. Investigation of convection in the solution zone at the growth of CdTe by THM. Crystal Research and Technology, 20:1609–1613, 1985.

[181] N. Aslam, E. D. Jones, T. C. Q. Noakes, J. B. Mullin, and A. F. W. Willoughby. The diffusion of zinc in cadmium telluride. Journal of Crystal Growth, 117:249–253, 1992.

[182] K. Mochizukia, K. Masumotoa, and K. Miyazaki. Melt growth of CdTe single crystals with controlled deviation from stoichiometry. Crystal Research and Technology, 6:119–122, 1988.

[183] K. Hjelt, M. Juvonen, T.Tuomi, S. Nenonen, and and M. Bavdaz E. E. Eissler. Photoluminescence of $Cd_{1-x}Zn_xTe$ crystals grown by high-pressure bridgman technique. Phys. Status Solidi (a), 162:747–763, 1997.

[184] Andrew Yeckel, Geoffrey Compère, Arun Pandy, and Jeffrey J. Derby. Three dimensional imperfections in a model vertical Bridgman growth system for cadmium zinc telluride. Journal of Crystal Growth, 263:629–644, 2004.

[185] B.W. Choi and H.N.G. Wadley. In situ studies of $Cd_{1-x}Zn_xTe$ nucleation and crystal growth. J. Crystal Growth, 208:219–230, 2000.

[186] K.M. Kim, A.F. Witt, and H.C. Gatos. Crystal growth from the melt under destabilizing thermal gradients. J. Electrochem Soc., 119:1218–1226, 1972.

[187] D.T.J. Hurle. Melt temperature fluctuations: Causes and response of the solidification front. Advances in Space Research, 3(5):43 – 50, 1983.

[188] G. Müller, G. Neumann, and W. Weber. Natural convection in vertical bridgman configurations. J. Crystal Growth, 70:78–93, 1984.

[189] V.V. Godlevsky, J.J. Derby, and J.R. Chelikowsky. Ab Initio molecular dynamics simulations of liquid CdTe and GaAs: Semiconducting versus metallic behavior. Phys. Rev. Lett., 81:4959–4962, 1998.

[190] M. Mühlberg, P. Rudolph, C. Genzel, B. Wermke, and U. Becker. Crystalline and chemical quality of CdTe and CdZnTe grown by the bridgman method in low temperature gradients. Journal of Crystal Growth, 101:275–280, 1990.

[191] M. Azoulay, A. Raizman, G. Gafni, and M. Roth. Crystalline perfection of melt-grown CdTe. Journal of Crystal Growth, 101:256–260, 1990.

[192] M. Azoulay, S. Rotter, G. Gafni, R. Tenne, and M. Roth. Zinc segregation in CdZnTe grown under Cd/Zn partial pressure control. Journal of Crystal Growth, 117:276–280, 1992.

[193] T.E Schlesinger, J.E Toney, H Yoon, E.Y Lee, B.A Brunett, L Franks, and R.B James. Cadmium zinc telluride and its use as a nuclear radiation detector material. Materials Science and Engineering: R: Reports, 32:103 – 189, 2001.

[194] P. Rudolph. Melt growth of II-VI compound single crystals. In M. Isshiki, editor, Recent Development of Bulk Crystal Growth. Research Signpost, Trivandrum, India, 1998.

[195] R. Triboulet. CdTe and CdZnTe growth. In H. J. Scheel and T. Fukuda, editors, Crystal growth technology, chapter 17, pages 373–406. John Wiley & Sons, Ltd. Sons Ltd., 2003.

[196] Hiroyuki Shiraki, Minoru Funaki, Yukio Ando, Akira Tachibana, Shinya Kominami, and Ryoichi Ohno. THM growth and characterization of 100 mm diameter CdTe

single crystals. In Nuclear Science Symposium Conference Record, 2008. NSS '08. IEEE, pages 126 –132, oct. 2008.

[197] U.N. Roy, S. Weiler, and J. Stein. Growth and interface study of 2 in diameter CdZnTe by THM technique. J. Cryst. Growth, 312(19):2840 – 2845, 2010.

[198] V. Carcelén, K.H. Kim, G.S. Camarda, A.E. Bolotnikov, A. Hossain, G. Yang, J. Crocco, H. Bensalah, F. Dierre, E. Diéguez, and R.B. James. Pt coldfinger improves quality of Bridgman-grown Cd0.9Zn0.1Te:Bi crystals. J. Cryst. Growth, 338:1–5, 2012.

[199] J. Crocco, H. Bensalah, Q. Zheng, V. Carcelén, and E. Diéguez. Influence of SiC pedestal in the growth of 50 mm CZT by vertical gradient freeze method. J. Cryst. Growth, in press, 2012.

[200] Robert J. Naumann. An analytical approach to the thermal modeling of Bridgman-type crystal growth II. Two-dimensional analysis. Journal of Crystal Growth, 58:569–584, 1982.

[201] Robert J. Naumann and Sandor L. Lehoczky. Effect of variable thermal conductivity on isotherms in Bridgman growth. Journal of Crystal Growth, 61:707–710, 1983.

[202] T. Jasinski and A. F. Witt. On control of the crystal melt interface shape during growth in a vertical Bridgman configuration. Journal of Crystal Growth, 71:295–304, 1985.

[203] T. Jasinski and A. F. Witt. U.S. Patent: Apparatus for growing crystals. (4597949), 1986.

[204] Jeffrey J. Derby and David Gasperino. Computational models for crystal growth of radiation detector materials: Growth of CZT by the EDG method. In D.L. Perry, A. Burger, L. Franks, and M. Schieber, editors, Nuclear Radiation Detection Materials, volume 1038 of Materials Research Society Symposium Proceedings, pages 1038–O05–09, 2008.

[205] J. J. Derby, D. Gasperino, N. Zhang, and A. Yeckel. Modeling the crystal growth of cadmium zinc telluride: Accomplishments and future challenges. In D.L. Perry, A. Burger, L. Franks, and M. Schieber, editors, Nuclear Radiation Detection Materials

— 2009, volume 1164 of Materials Research Society Symposium Proceedings, pages 1164–L05–02, 2009.

[206] A. Yeckel and R. T. Goodwin. Cats2D (Crystallization and Transport Simulator) user manual, 2010.

[207] Nan Zhang, Andrew Yeckel, Arnold Burger, Yunlong Cui, Kelvin G. Lynn, and Jeffrey J. Derby. Anomalous segregation during electrodynamic gradient freeze growth of cadmium zinc telluride. J. Crystal Growth, 325:10–19, 2011.

[208] A. Datta, K.A. Jones, S. Swain, and K.G. Lynn. Modified vertical bridgman growth of Cd1-xZnxTe detector grade crystal in a 4 inch EDG furnace. In Nuclear Science Symposium Conference Record (NSS/MIC), 2009 IEEE, pages 1771 –1776, 2009.

[209] Paul Sonda, Andrew Yeckel, Prodromos Daoutidis, and Jeffrey J. Derby. Hopf bifurcation and solution multiplicity in a model for destabilized Bridgman crystal growth. Chemical Engineering Science, 60(5):1323 – 1336, 2005.

[210] M. Pfeiffer and M. Mhlberg. Interface shape observation and calculation in crystal growth of cdte by the vertical bridgman method. Journal of Crystal Growth, 118(34):269 – 276, 1992.

[211] Mark S. Akselrod and Frank J. Bruni. Modern trends in crystal growth and new applications of sapphire. J. Cryst. Growth, xxx:xxx–xxx, 2012.

[212] D. Viechnicki and F. Schmid. Crystal growth using the heat exchanger method (hem). Journal of Crystal Growth, 26(1):162 – 164, 1974.

[213] D. Viechnicki and F. Schmid. Growth of large monocrystals of Al_2O_3 by a gradient furnace technique. Journal of Crystal Growth, 11(3):345 – 347, 1971.

[214] F. Schmid, C.P. Khattak, and M.B. Smith. Growth of bismuth germanate crystals by the heat exchanger method. Journal of Crystal Growth, 70(1-2):466 – 470, 1984.

[215] S. Brandon and Jeffrey J. Derby. Internal radiative transport in the vertical bridgman growth of semitransparent crystals. Journal of Crystal Growth, 110:481–500, 1991.

[216] S. Brandon and J. J. Derby. Heat transfer in vertical Bridgman growth of oxides: Effects of conduction, convection, and internal radiation. J. Crystal Growth, 121:473–494, 1992.

[217] S. Brandon, D. Gazit, and A. Horowitz. Interface shapes and thermal fields during the gradient solidification method growth of sapphire single crystals. J. Crystal Growth, 167:196–207, 1996.

[218] Alexander Virozub and Simon Brandon. Radiative heat transport during the vertical bridgman growth of oxide single crystals: slabs versus cylinders. Journal of Crystal Growth, 193(4):592 – 596, 1998.

[219] S.E. Demina, E.N. Bystrova, V.S. Postolov, E.V. Eskov, M.V. Nikolenko, D.A. Marshanin, V.S. Yuferev, and V.V. Kalaev. Use of numerical simulation for growing high-quality sapphire crystals by the kyropoulos method. Journal of Crystal Growth, 310:1443 – 1447, 2008. ¡ce:title¿the Proceedings of the 15th International Conference on Crystal Growth (ICCG-15) in conjunction with the International Conference on Vapor Growth and Epitaxy and the US Biennial Workshop on Organometallic Vapor Phase Epitaxy¡/ce:title¿.

[220] Jong Hoe Wang, Do Hyun Kim, and Jeung-Soo Huh. Modelling of crystal growth process in heat exchanger method. Journal of Crystal Growth, 174(1-4):13 – 18, 1997. American Crystal Growth 1996 and Vapor Growth and Epitaxy 1996.

[221] S. Brandon, D. Gazit, and A. Horowitz. Interface shapes and thermal fields during the gradient solidification method growth of sapphire single crystals. Journal of Crystal Growth, 167:190–207, 1996.

[222] Chung-Wei Lu and Jyh-Chen Chen. Numerical computation of sapphire crystal growth using heat exchanger method. Journal of Crystal Growth, 225(2-4):274 – 281, 2001.

[223] Jyh-Chen Chen and Chung-Wei Lu. Influence of the crucible geometry on the shape of the melt-crystal interface during growth of sapphire crystal using a heat exchanger method. Journal of Crystal Growth, 266(1-3):239 – 245, 2004. Proceedings of the Fourth International Workshop on Modeling in Crystal Growth.

[224] Chun-Hung Chen, Jyh-Chen Chen, Chung-Wei Lu, and Che-Ming Liu. Numerical simulation of heat and fluid flows for sapphire single crystal growth by the kyropoulos method. Journal of Crystal Growth, 318(1):162 – 167, 2011.

[225] Yu.K. Lingart. Radiation-Conductive Heat Transfer in Optical Crystals. Crystal Growth Equipment: Internal Report, 1992.

[226] R.C. Weast and M.J. Astle. CRC Handbook of Chemistry and Physics, (59th ed.). CRC Press, Boca Raton, FL, 1978-1979.

[227] J.J. Rasmussen and R.P. Nelson. Surface Tension and Density of Molten Al_2O_3. Journal of the American Ceramic Society, 54:398 – 401, 1971.

[228] R. Siegel and J.R. Howell. Thermal Radiation Heat Transfer. (2nd ed.). McGraw-Hill, New York, 1981.

[229] G. Urbain. Rev. Int. Temper. Refract. Fr., 19:55, 1982.

[230] Alexander Virozub and Simon Brandon. Revisiting the quasi-steady state approximation for modeling heat transport during directional crystal growth. the growth rate can and should be calculated! Journal of Crystal Growth, 254:267 – 278, 2003.

[231] Nan Zhang, Andrew Yeckel, and Jeffrey J. Derby. Maintaining convex interface shapes during electrodynamic gradient freeze growth of cadmium zinc telluride using a dynamic, bell-curve furnace profile. J. Crystal Growth, 355:113–121, 2012.

[232] H. G. Matthies, R. Niekamp, and J. Steindorf. Algorithms for strong coupling procedures. Comput. Methods Appl. Mech. Eng., 195:2028–2049, 2006.

[233] Lisa Lun. Modeling and Control of Cadmium Zinc Telluride Grown via an Electro-dynamic Gradient Freeze Furnace. PhD thesis, University of Minnesota, 2007.

[234] C. A. Felippa, K. C. Park, and C. Farhat. Partitioned analysis of coupled mechanical systems. Comput. Methods Appl. Mech. Eng., 190:3247–3270, 2001.

[235] R. Pawlowski, R. A. Bartlett, N. Belcourt, R. Hooper, and R. Schmidt. A theory manual for multi-physics code coupling in lime. Sandia Technical Report, 2011:2195, 2011.

[236] K. P. Dharmasena and H. N. G. Wadley. Eddy current sensing of vertical Bridgman growth of CdZnTe. J. Cryst. Growth, 172:337–349, 1997.

[237] K. P. Dharmasena and H. N. G. Wadley. Modeling multifrequency eddy current sensor interaction during vertical Bridgman growth of semiconductors. Rev. Sci. Instruments, 70:3125–3142, 1999.

[238] Chandra P. Khattak and Frederick Schmid. Growth of the world's largest sapphire crystals. Journal of Crystal Growth, 225(24):572 – 579, 2001. Proceedings of the 12th American Conference on Crystal Growth and Epitaxy.

[239] David B. Joyce and Frederick Schmid. Progress in the growth of large scale ti:sapphire crystals by the heat exchanger method (hem) for petawatt class lasers. Journal of Crystal Growth, 312(8):1138 – 1141, 2010. The 17th American Conference on Crystal Growth and Epitaxy/The 14th US Biennial Workshop on Organometallic Vapor Phase Epitaxy/The 6th International Workshop on Modeling in Crystal Growth.

[240] Frederick Schmid. U.S. Patent: Crystal Growing. (3898051), 1973.